DISSERTATION

GPU-ACCELERATED COMPUTATIONAL STUDY OF BLOCK COPOLYMER SELF-ASSEMBLY WITH ADVANCED POLYMER THEORIES

Submitted by

Juntong He

Department of Chemical and Biological Engineering

In partial fulfillment of the requirements

For the Degree of Doctor of Philosophy

Colorado State University

Fort Collins, Colorado

Summer 2024

Doctoral Committee:

Advisor: Qiang (David) Wang

Ashok Prasad
Travis Bailey
Martin Gelfand

ABSTRACT

GPU-ACCELERATED COMPUTATIONAL STUDY OF BLOCK COPOLYMER SELF-ASSEMBLY WITH ADVANCED POLYMER THEORIES

A high-performance GPU-accelerated software package for self-consistent field (SCF) calculations of block copolymer assembly, PSCF+, has been developed. PSCF+ allows various combinations of chain-connectivity models (including the continuous Gaussian chains, discrete Gaussian chains, and freely jointed chains), non-bonded isotropic pair (including the Dirac δ-function, soft-sphere, dissipative particle dynamics, and Gaussian) potentials and system compressibility (incompressible *vs.* compressible). The Richardson-extrapolated pseudo-spectral methods, the crystallographic fast Fourier transform, the "slice" algorithm, and the automated calculation-along-a-path are implemented in PSCF+, which not only speed up the SCF calculations and reduce the GPU memory usage significantly, but also make it very efficient in constructing phase diagrams. Given the wide use and great success of SCF calculations in understanding and predicting the self-assembled structures of block copolymer, PSCF+ will be an invaluable computational tool for the polymer community.

Using PSCF+, we studied the stability of various Frank-Kasper phases formed by neat diblock copolymer (DBC) A-B melts using the "standard" model and the dissipative particle dynamics chain model and found that in general the SCF phase diagrams of these two models are qualitatively the same but with important differences. We also studied the stability of various Frank-Kasper phases formed by binary DBC blends using the "standard" model and found that the relative stability among the Frank-Kasper phases is dominated by their internal-energy

densities. Finally, we performed high-accuracy SCF calculations to study the stability of all known tiling patterns formed by symmetrically interacting ABC miktoarm star triblock terpolymers.

ACKNOWLEDGEMENTS

My deepest gratitude goes to my advisor, Dr. Qiang Wang, whose expertise, guidance, and encouragement were invaluable throughout the course of my research. I also wish to thank the members of my dissertation committee, Dr. Ashok Prasad, Dr. Travis Bailey, and Dr. Martin Gelfand for their insightful feedback and constructive suggestions. Financial support for this work was provided by U.S. Department of Energy (Award No. DE-SC0023203), which are gratefully acknowledged.

I would like to thank my family members for their support, trust, and patience.

TABLE OF CONTENTS

1 INTRODUCTION

1.1 Self-Consistent Field Theory

Polymeric self-consistent field theory (SCFT) is a field-based theory with mean-field approximation for the study of polymeric systems. In general, a many-chain system in thermodynamic equilibrium can be described by a partition function: The essence of the SCFT is to convert the particle-based description into a field-based one via Hubbard-Stratonovich transformation, under which the representation of interactive many-chain system is replaced by that of single chain interacting with certain fluctuating fields.[1] The essential step of Hubbard-Stratonovich transformation is inserting the identity,

$$1=\int\prod_i \mathrm{D}\rho_i(\mathbf{r})\delta\left[\rho_i(\mathbf{r})-\hat{\rho}_i(\mathbf{r})\right]=\int\prod_i \mathrm{D}\omega_i\mathrm{D}\rho_i \exp\left(\int \mathrm{d}\mathbf{r}\,\omega_i(\mathbf{r})\left(\rho_i(\mathbf{r})-\hat{\rho}_i(\mathbf{r})\right)\right),$$

into the particle-based partition function, where i denotes all the molecular species in the system, $\delta[\bullet]$ is the delta function, $\hat{\rho}_i$ is the microscopic number density, ρ_i is the fluctuating particle number density fields constrained to $\hat{\rho}_i$, ω_i is fluctuating *inhomogenous* chemical potential fields conjugated to the ρ_i. Note that the above particle-field transformation is restricted to "soft" potential that is finite at on contact. With the Hubbard-Stratonovich transformation one can obtain the field-based partition function of a many-chain system,

$$Q=\int\prod_i \mathrm{D}\omega_i \exp\left(-\beta H[\{\omega_i\}]\right),$$

where $\{\omega_i\}$ is the set of ω_i, $\beta\equiv 1/k_BT$ with k_B being the Boltzmann constant, and $H[\{\omega_i\}]$ is the effective Hamiltonian. However, the effective Hamiltonian is complex, which means the Boltzmann-like factor $\exp\left(-\beta H[\{\omega_i\}]\right)$ is not positive-definite. This property causes the so-

called “sign-problem” when simulating the fields[2]. Dealing with the “sign-problem” requires special numerical techniques and is not discussed in this dissertation.

For system of melts or concentrated solutions of high-molecular weight polymers, it is reasonable to assume that the partition function is dominated by a single field configuration $\bar{\omega}$ because the fluctuations of the surrounding of each polymer chain vanish at large molecular weight; therefore, $Q \approx \exp\left(-\beta H[\{\bar{\omega}_i\}]\right)$ can describe the system, This idea is called the mean-field approximation and the mean-fields $\bar{\omega}$ are obtained by the self-consistent field equations

$$\left.\frac{\partial H[\{\omega_i\}]}{\partial \omega_i}\right|_{\bar{\omega}_i} = 0.$$

The SCFT can calculate the Helmholtz free energy directly, by which one can compare and predict the stability of various possible morphologies. SCFT is the essential framework for this work and its theoretical and computational details are discussed in the following chapters.

1.2 Outline

This dissertation introduces a GPU-accelerated high-performance software package, PSCF+, for self-consistent field (SCF) calculations and gives a series of studies on stability of Frank-Kasper phase formed by block copolymer using PSCF+. The emergence of various phases in block copolymers can be explained qualitatively with deep insight into their formation mechanism.

Chapter 2 is devoted to a discussion of PSCF+, an extended and improved open-source software package for polymer self-consistent field calculations of block copolymers (BCP) self-assembly. I discuss the extensions and improvements by our group to PSCF which is an open-source software package originally developed by Prof. Morse’s group[3] for calculation of the self-assembled periodic structures of arbitrary mixtures of acyclic BCPs. The extension of PSCF

includes various combinations of chain models, non-bonded interactions, and compressibility. Richardson-extrapolated pseudo-spectral (REPS) methods for solving modified diffusion equations are implemented to save GPU memory usage. The crystallographic fast Fourier transform for the *Pmmm* supergroups is implemented to save GPU memory usage and to accelerate the SCF calculations. I also discuss the implementation of the "slice" algorithm. Other improvements are discussed at the end of this chapter.

In chapter 3, phase diagrams are presented for conformationally asymmetric diblock copolymer A-B melts using the SCF calculations of both the dissipative particle dynamics chain (DPDC) model (*i.e.*, compressible melts of discrete Gaussian chains with the DPD non-bonded potential) and the "standard" model (*i.e.*, incompressible melts of continuous Gaussian chains with the Dirac δ-function non-bonded potential) in the χN-ε plane, where χN and ε characterize, respectively, the repulsion and conformational asymmetry between A and B blocks, at the A-block volume fraction f=0.2 and 0.3. Consistent with previous SCF calculations of the "standard" model, σ and A15 are the only stable FK phases among the five FK (*i.e.*, σ, A15, C14, C15 and Z) phases considered. The stability of σ is due to its delicate balance between the energetic and entropic contributions to the Helmholtz free energy per chain of the system, which within our parameter range increases in the order of σ/A15, Z, C14 and C15, and σ and A15 always have smaller internal energy per chain due to the A-B repulsion than Z, C14 and C15. At f=0.2 the SCF phase diagram for the DPDC model is qualitatively the same as that for the "standard" model, but they are qualitatively different at f=0.3 (where A15 is not stable for the DPDC model at the copolymer chain length N=10); the latter and any quantitative differences in the SCF phase diagrams are solely due to the differences between these two models.

In chapter 4, we performed SCF calculations of the "standard" model to investigate seven Frank-Kasper phases (A15, σ, H, Z, pσ, C14 and C15) formed by both neat diblock copolymer A-B melts and binary DBC blends and found that their relative stability is dominated by the internal-energy densities (*i.e.*, the repulsion between A and B blocks). This trend is also found in other SCF data (including the binary blends of DBC and homopolymer), regardless of the detailed models used. We further found that the variations of the Helmholtz free-energy (and the internal-energy) density curves of different FK phases are clearly correlated with the average coordination number of the Wigner-Seitz polyhedra (which is equivalent to the average number of six-fold rotation axes) in these FK phases. Finally, the change of stable phase between σ and C14/C15 in binary DBC blends is mainly due to that in the interchain repulsion. In this work, Zhiwei Zhuang was responsible for performing SCF calculations, constructing phase diagram based on SCF results. I was responsible for providing initial guesses of omega field for SCF calculations, visualizing the morphologies of various FK phases, analyzing thermodynamic and morphological properties of various FK phases.

The results of stable and unstable tiling patterns formed by ABC miktoarm star triblock terpolymers of symmetric interactions are discussed in chapter 5, Several discrepancies exist among previous self-consistent field calculations of symmetrically interacting ABC miktoarm star triblock terpolymers, in part due to the differences in their candidate phases and the possible numerical inaccuracies. In this chapter, this issue is addressed by including all known tiling patterns, as well as several lamellar-type phases known to bound the regions in the parameter space occupied by these patterns. After carefully studying the effect of numerical parameters on the free-energy accuracy, the central region of the phase diagram is constructed in detail; both the (3.4.6.4) pattern and the 3D phase of hierarchical-hexagonal lamellae are found to be stable for

the first time. The energetic and entropic contributions to the free-energy density of several phases are analyzed and compared in detail to reveal their stability mechanisms, including the important (3^2.4.3.4) pattern. Comparisons to previous studies of the same model system are present throughout, with our results resolving the aforementioned discrepancies and providing a sound basis for future work to build upon. In this work, Cody Hawthorne was responsible for providing initial guesses of omega field for SCF calculations, constructing phase diagram based on SCF results, visualizing the tiling patterns, analyzing thermodynamic and morphological properties of complex tiling pattern. I was responsible for performing SCF calculations, analyzing numerical accuracy and implementing of free energy decomposition and star-junction density field calculation.

REFERENCES

[1] J. Hubbard, Phys. Rev. Lett. 3, 77 (1959).

[2] G. H. Fredrickson, V. Ganesan, and F. Drolet, Macromolecules 35 (1), 16-39 (2002).

[3] A. Arora, J. Qin, D. C. Morse, K. T. Delaney, G. H. Fredrickson, F. S. Bates, and K. D. Dorfman, Macromolecules 49, 4675 (2016).

2 PSCF+: AN EXTENDED AND IMPROVED OPEN-SOURCE SOFTWARE PACKAGE FOR POLYMER SELF-CONSISTENT FIELD CALCULATIONS

2.1 Introduction

In 2016, Morse and co-workers released the Fortran version[1] of PSCF[2], an open-source software package for polymer self-consistent field (SCF) calculations of the "standard" model (*i.e.*, an incompressible melt of continuous Gaussian chains (CGCs) with the Dirac δ-function repulsions) of block copolymer (BCP) self-assembly. BCPs consist of chemically distinct polymer chains (*i.e.*, blocks) covalently bonded together, and can spontaneously self-assemble into spatially periodic structures with their characteristic length ranging from a few to tens or even hundreds of nanometers; they therefore have great potential applications in many fields including nanotechnology, drug delivery, advanced plastics, *etc.*[3-5] While the underlying physics of BCP self-assembly (*i.e.*, the delicate balance of the energetic repulsion between various blocks and their entropic stretching under the space-filling requirement) has been qualitatively understood, given the large parameter space spanning chain architecture, block lengths, block flexibility and segment interactions, ***quantitative*** predictions of the self-assembled structures and their stabilities are needed for rational design of BCPs. Since the pioneer work of Edwards[6], SCF theory[7, 8] has been widely applied to many inhomogeneous polymers (*e.g.*, polymers at surfaces, self-assembled BCPs, *etc.*) with great success. In particular, it can be considered as the most successful molecular-level theory for BCP self-assembly[7, 9], partly due to its well-developed numerical calculations[9-17]. The release of PSCF, as well as the publication[2] of a pedagogical introduction to it and the SCF theory, has provided broad access of SCF calculations and lowered the barrier to their use even by experimental groups.

PSCF is designed to perform unit-cell calculations of the self-assembled periodic

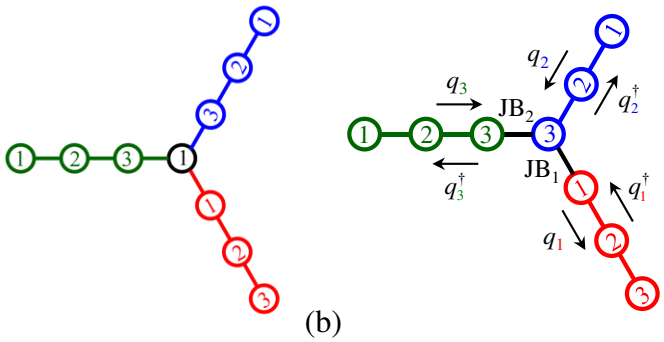

Figure 2.1. A discrete chain model of (a) symmetric and (b) asymmetric star triblock terpolymer consisting of three arms (shown in red, blue and green) each having three segments. In PSCF+, the three arms can have different effective bond lengths (represented in different colors). In part (a), the three arms are connected to a common JS (shown in black) via three JBs (shown in red, blue and green), and the non-bonded interactions of the JS can be set to 0. In (b), no JS and only two JBs (shown in black) are used, and the initial condition of the backward propagator for block i=2 is $q_2^\dagger(\mathbf{r}, s=3) = \exp\left(-\omega_m(\mathbf{r})\right)\int d\mathbf{r}'\Phi_{\mathrm{JB}_1}(|\mathbf{r}-\mathbf{r}'|)q_1^\dagger(\mathbf{r}', s=1)\int d\mathbf{r}''\Phi_{\mathrm{JB}_2}(|\mathbf{r}-\mathbf{r}''|)q_3(\mathbf{r}'', s=3)$, where m denotes the segment type of the block i=2, and $\Phi_{\mathrm{JB}_1}(r)$ and $\Phi_{\mathrm{JB}_2}(r)$ are the transition probabilities (which can be different) of the two JBs.

structures of arbitrary mixtures of flexible and acyclic BCPs (including homopolymers and small-molecule solvents) in either canonical or grand-canonical ensemble. While the Fortran version can only run on a single CPU, Morse and co-workers later released the C++/Cuda version[18], which takes advantage of the massive parallelization provided by GPUs and can solve millions of variables within minutes[19]. Their benchmark using double-precision calculations indicated about 30 times speed-up over the CPU version of PSCF, with the speed-up increasing with increasing unit-cell size. Such speed-up is achieved by (1) using the NVIDIA's cuFFT library[20] to perform the fast Fourier transforms (FFTs) needed for solving the modified diffusion equations (MDEs) in the "standard" model, (2) evaluating all the integrals over the chain contour and the spatial domain on the GPU, and (3) offloading to the GPU the Anderson-mixing (AM) algorithm[15] used for solving the SCF equations. The C++/Cuda version of PSCF therefore

provides a nice framework for SCF calculations on GPUs.

While the "standard" model has been the most commonly used one in polymer field theories including the SCF theory due to its least number of model parameters, other models[8, 21-25] have also been used in SCF calculations. More importantly, the mean-field approximation inherent in all SCF calculations neglects the system fluctuations and correlations, and the only way to unambiguously quantify its consequences is to directly compare the SCF results with those obtained from molecular (*i.e.*, Monte Carlo and molecular dynamics) simulations[22, 23, 25-33] or field-theoretic simulations (FTS)[34] of the ***same*** model system, thus without any parameter-fitting. Unfortunately, the infinite number of segments on each CGC, the zero range of the Dirac δ-function repulsions, and the incompressibility constraint imposed at every spatial point in continuum all make the "standard" model not usable in molecular simulations; the first two also lead to the ultraviolet divergence that is problematic in FTS[35]. We have therefore extended PSCF to systems of various discrete chain models and finite-range (non-bonded) interactions. We have also improved several aspects of PSCF, including calculations of the "standard" model.

Assuming that readers are familiar with the SCF theory of the "standard" model for BCP self-assembly and the usage of PSCF[1, 2, 18, 19], in the rest of this paper we describe in detail our extension and improvement made to PSCF, along with numerical examples and performance benchmark. Our extended and improved PSCF, referred to as PSCF+ hereafter, is freely available at https://github.com/qwcsu/PSCFplus.

2.2 SCF Calculations of Discrete Chain Models

2.2.1 Discrete chain models

In PSCF, an (acyclic) BCP chain consists of $n_B \geq 1$ (linear homopolymer) blocks connecting $n_V = n_B + 1$ vertices (including both joints and free ends); each block is specified by its

segment (referred to as "monomer") type and block length (*i.e.*, number of segments on the block, which is not limited to integer values, calculated using a common segment volume; this is actually proportional to the block volume fraction in the copolymer), and the BCP chain architecture is determined by specifying which block connects which two vertices. For the rest of this section, we describe SCF calculations of discrete chain models implemented in PSCF+.

Different from the above CGC model, block i (=1,…,n_B) of a (flexible) BCP chain in a discrete chain model consists of $N_i \geq 1$ segments (*i.e.*, interaction sites) of the same segment type m sequentially connected by N_i-1 bonds, each having the dimensionless bonding potential $\beta u_m^{\mathrm{b}}(r)$, where $\beta \equiv 1/k_B T$ with k_B denoting the Boltzmann constant and T the thermodynamic temperature of the system, and r denotes the distance between the two bonded segments; clearly, the special case of a BCP whose blocks all have the same segment type corresponds to a homopolymer, that of a BCP having $n_B=1$ corresponds to a linear homopolymer, and that of a linear homopolymer having only one segment corresponds to a small-molecule solvent. Note that we shift $\beta u_m^{\mathrm{b}}(r)$ by a constant such that $4\pi \int_0^\infty \mathrm{d}r r^2 \Phi_m(r) = 1$ with the bond transition probability $\Phi_m(r) \equiv \exp\left(-\beta u_m^{\mathrm{b}}(r)\right)$; for example, $\Phi_m^{\mathrm{FJC}}(r) = \delta\left(r - b_m\right) \big/ 4\pi b_m{}^2$ for the freely jointed chain (FJC) of fixed bond length b_m, and $\Phi_m^{\mathrm{DGC}}(r) = \left(3/2\pi b_m{}^2\right)^{3/2} \exp\left(-3r^2/2b_m{}^2\right)$ for the discrete Gaussian chain (DGC) of effective bond length b_m. The (acyclic) BCP chain architecture is then determined by specifying how these n_B blocks are connected by $n_J=n_B-1$ ***joint bonds*** (JB), each connecting one end-segment of a block to an end-segment of a different block. Clearly, in the limit of $N_i \to \infty$ at finite root-mean-square end-to-end distance of an ideal block $\sqrt{N_i - 1} b_m > 0$, a block of either FJC or DGC becomes that of CGC.

While different chain-connectivity models (*i.e.*, functional forms of $\Phi(r)$) could be used for different bonds, for simplicity we assume in PSCF+ the same chain-connectivity model (which can be either DGC, FJC, or CGC) for a given system, where different segment types can have different b_m to account for their conformational asymmetry, and use $\sqrt{b_m b_{m'}}$ for the joint bond connecting two blocks of segment type m and m', respectively. As in PSCF, we also assume (without loss of generality) that all segments, regardless of their type, have the same volume $1/\rho_0$; different from the block lengths in PSCF, however, N_i here must be a positive integer. For symmetry consideration, one can introduce a ***joint block (segment)*** of N_i=1, and simply use b_m for the joint bond connecting it to a block of segment type m; Fig. 2.1(a) shows an example of symmetric three-arm star triblock terpolymer, where a joint segment (JS) is needed.

2.2.2 Propagators and volume-fraction fields

The crux of SCF calculations is to compute the (one-end-integrated) forward and backward propagators. The forward propagator of segment s (=1,…,N_i) on the above block i at spatial position $\mathbf{r}$, $q_i(\mathbf{r},s)$, satisfies the recursive Chapman-Kolmogorov equation (CKE) $q_i(\mathbf{r},s+1)=\exp\left(-\omega_m(\mathbf{r})\right)\int \mathrm{d}\mathbf{r}'\Phi_m(|\mathbf{r}-\mathbf{r}'|)q_i(\mathbf{r}',s)$ for s=1,…,N_i−1, where $\omega_m(\mathbf{r})$ is the conjugate field interacting with segments of type m; that is, $q_i(\mathbf{r},s)$ propagates in the direction of increasing s. Similarly, the backward propagator of segment s on the above block i, $q_i^\dagger(\mathbf{r},s)$, satisfies the CKE $q_i^\dagger(\mathbf{r},s-1)=\exp\left(-\omega_m(\mathbf{r})\right)\int \mathrm{d}\mathbf{r}'\Phi_m(|\mathbf{r}-\mathbf{r}'|)q_i^\dagger(\mathbf{r}',s)$ for s=N_i,N_i−1,…2; that is, $q_i^\dagger(\mathbf{r},s)$ propagates in the direction of decreasing s. The CKE has the initial condition of $q_i(\mathbf{r},s=1)=\exp\left(-\omega_m(\mathbf{r})\right)$ ($q_i^\dagger(\mathbf{r},s=N_i)=\exp\left(-\omega_m(\mathbf{r})\right)$) if segment s=1 (s=N_i) is a free end, and otherwise that given by the product of the end-segment propagators that propagate into segment s=1 (s=N_i) over all other blocks connected to the segment, each convoluted with the transition

probability of the connecting JB, with $\exp\left(-\omega_m(\mathbf{r})\right)$; see Fig. 2.1(b) for an example.

Note that for given chain architecture of acyclic BCPs, the order of computing the forward and backward propagators for all the blocks (*i.e.*, the labeling of the two ends of block *i* as *s*=0 for CGC or 1 for discrete-chain models and N_i, respectively) is automatically determined in PSCF+, following the same approach as used in PSCF.

For given $\{\omega_m(\mathbf{r})\}$ over all segment types, after the propagators are computed, the volume fraction of segments of type *m* at **r** on block *i* in the BCP (which is molecular component *c* in the system) in canonical ensemble is given by $\phi_{i,m}(\mathbf{r}) = \overline{\phi}_c \exp\left(\omega_m(\mathbf{r})\right) \sum_{s=1}^{N_i} q_i(\mathbf{r},s) q_i^{\dagger}(\mathbf{r},s) \Big/ N_c Q_c$, where $\overline{\phi}_c$ is the overall volume fraction of component *c* in the system, $N_c \equiv \sum_{i=1}^{n_B} N_i$ the total number of segments on a BCP molecule of component *c*, and $Q_c = \hat{q}_j(\mathbf{q}=\mathbf{0}, N_j)$ is the normalized single-chain partition function of component *c*, where $\hat{g}(\mathbf{q}) \equiv \int d\mathbf{r} \exp\left(-\sqrt{-1}\mathbf{q}\bullet\mathbf{r}\right) g(\mathbf{r}) \Big/ V$ denotes the Fourier transform of a ***spatially periodic*** function $g(\mathbf{r})$ with **q** being the wavevector and *V* the system volume, and *j* can be ***any*** block whose last segment is a free end. The total volume fraction of segments of type *m* at **r**, $\phi_m(\mathbf{r})$, is then obtained by summing $\phi_{i,m}(\mathbf{r})$ over all the components and their blocks whose segment type is *m*.

2.2.3 Non-bonded interactions

The excluded-volume interactions between segments can be modeled either via the incompressibility constraint

$$\sum_{m=1}^{n_m} \phi_m(\mathbf{r}) = 1 \tag{2.1}$$

imposed at all **r** as in the "standard" model, where n_m denotes the total number of segment types

in the system, or via the non-bonded isotropic pair potentials $u^{\kappa}(r)$ as in molecular simulations, where the system is compressible. While different non-bonded potentials could be used for the excluded-volume interactions between different types of segments, for simplicity we assume in PSCF+ that $u^{\kappa}(r)$ is the same for all segments (the JSs can have no non-bonded interactions). In particular, non-bonded potentials must be ***integrable*** in SCF theory[36, 37] and we take $u^{\kappa}(r) = u_0(r)/\kappa\rho_0$, where $4\pi\int_0^{\infty} \mathrm{d}r r^2 \beta u_0(r) = 1$ and the dimensionless parameter κ>0 controls the potential strength (thus the system compressibility). We have implemented in PSCF+ the soft-sphere (SS) potential $\beta u_0^{\mathrm{SS}}(r) = 3/4\pi\sigma^3$ for $r<\sigma$ and 0 otherwise with σ>0 being the potential cut-off, the dissipative particle dynamics (DPD) potential $\beta u_0^{\mathrm{DPD}}(r) = \left(15/2\pi\sigma^3\right)\left(1 - r/\sigma\right)^2$ for $r<\sigma$ and 0 otherwise, and the Gaussian (G) potential $\beta u_0^{\mathrm{G}}(r) = \exp\left(-r^2/\sigma^2\right)\Big/\left(\sqrt{\pi}\sigma\right)^3$ with σ>0 controlling the potential range; all of these are purely repulsive and in the limit of $\sigma\to 0$ become the Dirac δ-function potential.

For BCP self-assembly, non-bonded repulsions between segments of different types are needed in addition to the above excluded-volume interaction, and we simply take them to be $u_{mm'}^{\chi}(r) = u_0(r)\chi_{mm'}/\rho_0$, where the dimensionless parameter $\chi_{mm'}\geq 0$ controls the repulsion strength between two segments of type m and m', respectively, with χ_{mm}=0. The "standard" model for BCP self-assembly is therefore recovered in the limit of $N_i\to\infty$ at finite $\sqrt{N_i - 1}b_m$ for all blocks (except the joint blocks, which always have N_i=1 with only $b_m\to 0$ taken for the limit), $\kappa\to 0$ and $\sigma\to 0$.

2.2.4 SCF equations, mean-field free energy and stresses

With the above non-bonded potentials, the SCF equations are given by

$$\omega_m(\mathbf{r}) = \xi(\mathbf{r}) + \int \mathrm{d}\mathbf{r}' \beta u_0(|\mathbf{r}-\mathbf{r}'|) \sum_{m'=1}^{n_m} \chi_{mm'} \phi_{m'}(\mathbf{r}') \tag{2.2}$$

for an incompressible system, where $\xi(\mathbf{r})$ is the conjugate field enforcing the incompressibility constraint (*i.e.*, Eq. (2.1)), and

$$\omega_m(\mathbf{r}) = \int \mathrm{d}\mathbf{r}' \beta u_0(|\mathbf{r}-\mathbf{r}'|) \sum_{m'=1}^{n_m} \left(\frac{1}{\kappa} + \chi_{mm'} \right) \phi_{m'}(\mathbf{r}') - \frac{1}{\kappa} \tag{2.3}$$

for a compressible system. Note that for the JSs having no non-bonded interactions (denoted by segment type J), $\chi_{m\mathrm{J}}$=0 for all m, $\omega_{\mathrm{J}}(\mathbf{r})$=0, and J is excluded from the summation in Eqs. (2.1)~(2.3).

After these SCF equations are solved, the (mean-field) dimensionless Helmholtz free energy per segment in canonical ensemble can be calculated as $\beta f \equiv \beta F / \rho_0 V = -\frac{1}{2} \sum_{\mathbf{q}} \sum_{m=1}^{n_m} \hat{\omega}_m(\mathbf{q}) \hat{\phi}_m(-\mathbf{q}) - \sum_{c=1}^{n_c} \left(\bar{\phi}_c / N_c \right) \ln Q_c$, where F denotes the (mean-field) Helmholtz free energy of the system, and n_c the total number of molecular (BCP) components in the system; note that, for an incompressible system, all the conjugate fields (*i.e.*, $\omega_m(\mathbf{r})$ for all m and $\xi(\mathbf{r})$) can be shifted by an arbitrary constant without affecting the volume fraction fields (*i.e.*, $\phi_m(\mathbf{r})$ for all m) and βf, and this property is used in PSCF (and PSCF+) to set $\int \mathrm{d}\mathbf{r} \xi(\mathbf{r}) = 0$. Also note that, for BCP self-assembly, βf should be minimized with respect to the unit-cell size and shape, which are controlled by up to six unit-cell parameters denoted by $\boldsymbol{\theta}$; this gives up to six additional SCF equations

$$\frac{\partial \beta f}{\partial \boldsymbol{\theta}} = \mathbf{0}, \tag{2.4}$$

where the derivative is taken at fixed conjugate fields[38]. Following Ref. 38(which is for the "standard" model), we find that

$$\frac{\partial \beta f}{\partial \boldsymbol{\theta}} = \sum_{\mathbf{q}} \frac{\partial q}{\partial \boldsymbol{\theta}} \frac{\mathrm{d}\beta \hat{u}_0(q)}{\mathrm{d}q} \sum_{m=1}^{n_m} \hat{\phi}_m(-\mathbf{q}) \left(\frac{1}{2} \sum_{m'=1}^{n_m} \chi_{mm'} \hat{\phi}_{m'}(\mathbf{q}) + C(\mathbf{q}) \right) - \sum_{c=1}^{n_c} \frac{\bar{\phi}_c}{N_c Q_c} \frac{\partial Q_c}{\partial \boldsymbol{\theta}} = 0 \quad \text{with} \quad C(\mathbf{q})=0 \quad \text{for}$$

incompressible systems and $\frac{1}{\kappa}\left(\frac{1}{2} \sum_{m'=1}^{n_m} \hat{\phi}_{m'}(\mathbf{q}) - \delta_{\mathbf{q},\mathbf{0}} \right)$ for compressible systems, and $\frac{\partial Q_c}{\partial \boldsymbol{\theta}}$ given by

the summation of $\sum_{\mathbf{q}} \frac{\partial q}{\partial \boldsymbol{\theta}} \frac{\mathrm{d}\hat{\Phi}_b(q)}{\mathrm{d}q} \hat{q}'(\mathbf{q}, s_b) \hat{q}'(-\mathbf{q}, s_b')$ over each bond b (which connects segments s_b and s_b') in a BCP molecule of component c, where $q \equiv |\mathbf{q}|$, $\hat{u}_0(q) = (4\pi/q) \int_0^\infty \mathrm{d}r r \sin(qr) u_0(r)$ is the 3D Fourier transform of $u_0(r)$ with $\beta \hat{u}_0(q=0) = 1$, $\hat{\Phi}_b(q)$ is similarly defined with $\hat{\Phi}_b(q=0) = 1$ and $\Phi_b(r)$ being the bond transition probability of b, and $\hat{q}'(\mathbf{q}, s_b)$ and $\hat{q}'(-\mathbf{q}, s_b')$ denote the 3D Fourier transform of the two (either forward or backward) propagators propagating into b.

In PSCF+, all of the above convolutions are efficiently computed using FFTs (see Sec. 2.4 below for more details), the integrals over the spatial domain (*i.e.*, the unit-cell) in Q_c, βf, and stress are evaluated using the (composite) trapezoidal rule[39] on GPU, and the SCF equations (*i.e.*, Eqs. (2.1)and (2.2) for an incompressible system or (2.3) for a compressible system, along with Eq.(2.4)) are solved with AM combined with a variable-cell method[16] as used in PSCF (with the improvement described in Sec. 2.5.1 below).

Finally, we note that while PSCF+ allows various combinations of chain-connectivity models (including CGC, FJC and DGC), non-bonded potentials (including the Dirac δ-function, SS, DPD, and G) and system compressibility (incompressible *vs.* compressible), as shown in Refs. 24 and 25 a model system of discrete chains with the Dirac δ-function non-bonded potential leads to unphysical results for BCP self-assembly. We also note that only compressible systems of discrete chains with the SS or DPD non-bonded potential can be directly used in

molecular simulations.

2.3 Richardson-Extrapolated Pseudo-Spectral (REPS) Methods for Solving MDEs

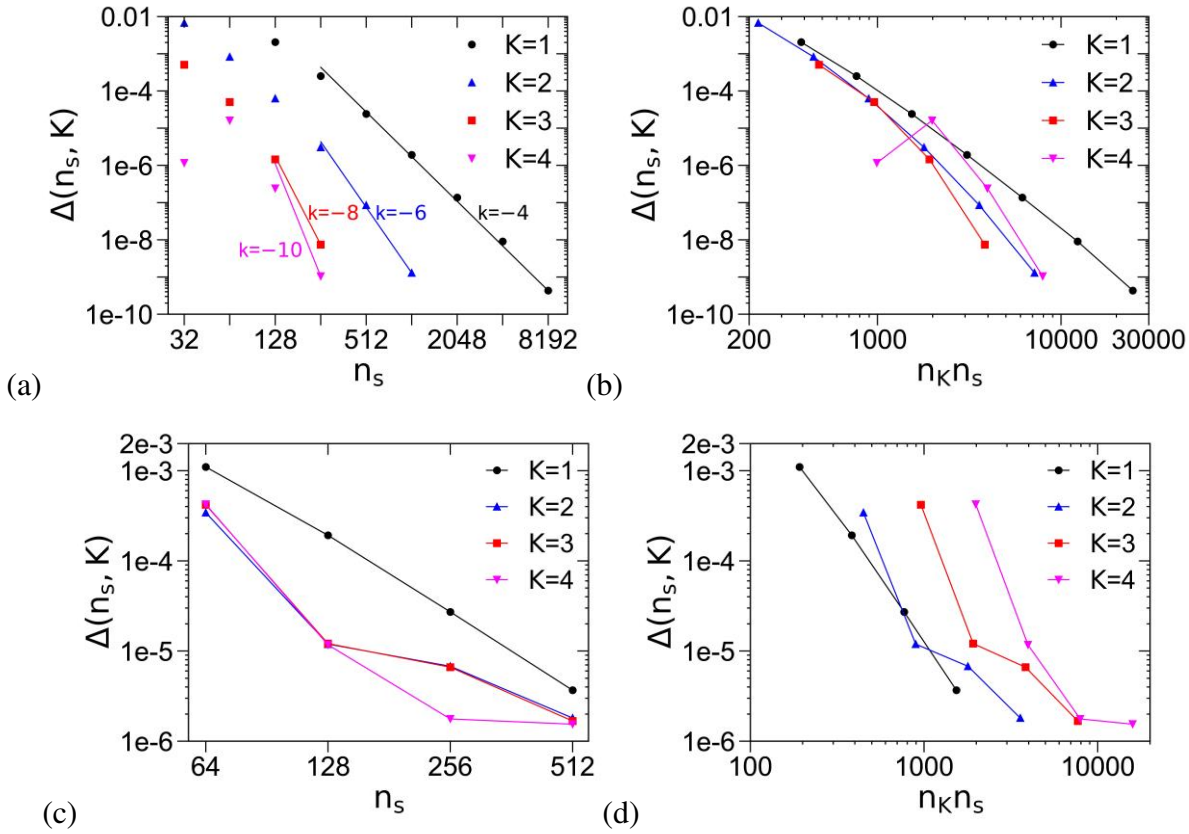

Figure 2.2. Logarithmic plots of the accuracy in the dimensionless Helmholtz free energy per DBC chain βf_c as a function of the number of chain-contour discretization steps n_s and the computing time $n_K n_s$ for various REPS-K methods in our SCF calculations of the "standard" model. Parts (a) and (b) are for lamellae formed by symmetric DBCs A-B at $\chi_{AB}(N_A+N_B)=100$, and (c) and (d) are for σ formed by asymmetric A-B at $\chi_{AB}(N_A+N_B)=40$, $N_A/(N_A+N_B)=0.25$ and $b_A^2/b_B^2=4$. The k-values in (a) give the slope of the corresponding straight line. The unit cell is uniformly discretized into 512 and 128×128×64 grid points for lamellae and σ, respectively. See the main text for more details.

For CGCs as used in the "standard" model, the propagators satisfy the MDEs, which can be obtained from the CKEs by Taylor expansion.[7] Here we consider as an example the forward propagator $q(\mathbf{r},s)$ in a block of length N and the effective bond length b, where $s\in[0,N]$ is the

(continuous) variable along the block contour; the MDE is then $\frac{\partial q}{\partial s} = \frac{b^2}{6}\nabla^2 q - \omega(\mathbf{r})q$ with given initial condition of $q(\mathbf{r},s=0)$, where $\omega(\mathbf{r})$ is the conjugate field interacting with segments on the block, and has the formal solution of $q(\mathbf{r}, s+\mathrm{d}s) = \exp\left[\left(\frac{b^2}{6}\nabla^2 - \omega(\mathbf{r})\right)\mathrm{d}s\right] q(\mathbf{r},s)$. Discretizing the block contour into n steps each of step-size $\Delta s = N/n$, one needs to numerically calculate $q(\mathbf{r},s+\Delta s)$ for given $q(\mathbf{r},s)$, where $s=j\Delta s$ and $j=0,\ldots,n-1$. For BCP self-assembly under the periodic boundary conditions, the 2nd-order pseudo-spectral (PS) method[40] gives $q(\mathbf{r}, s+\Delta s) \approx \exp\left(-\frac{\omega(\mathbf{r})\Delta s}{2}\right)\exp\left(\frac{b^2\Delta s}{6}\nabla^2\right)\exp\left(-\frac{\omega(\mathbf{r})\Delta s}{2}\right) q(\mathbf{r},s)$, which has a ***global*** error of $O(\Delta s^2)$ and can be readily computed using FFTs. While one of us combined the PS method with Richardson extrapolation[40] to obtain more accurate results[14], Morse and co-workers first pointed out that the error of the PS method contains only even powers of Δs and thus proposed a 4th-order method, which is used in PSCF, by linearly extrapolating the two results of $q(\mathbf{r},s+\Delta s)$ obtained via the PS method with the step-size of Δs and $\Delta s/2$, respectively, to the limit of $\Delta s \to 0$[49]. This is similar to the trapezoidal rule for numerical integration, the error of which also contains only even powers of the step-size; the Kth-order polynomial extrapolation of the $K+1$ results obtained via the trapezoidal rule with successively halved step-size to the limit of zero step-size then gives the commonly used Romberg integration[40], with $K=1$ corresponding to the Simpson's 1/3 rule. We therefore refer to the PS method and that proposed by Morse and co-workers[49] as the REPS-0 and REPS-1 method, respectively, and have implemented the REPS-K (for $K=0,\ldots,4$) method in PSCF+; polynomial extrapolation with $K>4$ may be unstable.

To be more specific, let q_k ($k=1,\ldots,K+1$) be the result of $q(\mathbf{r},s+\Delta s)$ obtained via the PS

method with a step-size of $\Delta s/2^{k-1}$, and q_0 be the extrapolated result given by the REPS-K method; one can then write $q_k = q_0 + \sum_{i=1}^{K} a_i \left(\frac{\Delta s}{2^{k-1}} \right)^{2i}$. For given Δs and q_k's, solving q_0 and the coefficients a_i (i=1,…,K) from these K+1 equations we obtain $q_0 = \left(4q_2 - q_1\right)/3$ (*i.e.*, Eq. (A6) in Ref. 49) for K=1, $q_0 = \left(64q_3 - 20q_2 + q_1\right)/45$ for K=2, $q_0 = \left(4096q_4 - 1344q_3 + 84q_2 - q_1\right)/2835$ for K=3, and $q_0 = \left(1048576q_5 - 348160q_4 + 22848q_3 - 340q_2 + q_1\right)/722925$ for K=4. Note that the REPS-K method has a global error of $O(\Delta s^{2(K+1)})$; this requires the Romberg integration of the same (or higher) order to calculate the integral $\int_0^N \mathrm{d}s q(\mathbf{r},s) q^{\dagger}(\mathbf{r},s)$ involved in the volume-fraction field (*e.g.*, the Simpson's 1/3 rule is used in PSCF to match the REPS-1 method), which in turn requires n be an integer multiple of 2^K. We also note that the REPS-K method requires $n_K \equiv 2^{K+1}-1$ pairs of forward and backward FFTs to obtain $q(\mathbf{r},s+\Delta s)$ from $q(\mathbf{r},s)$.

To compare the numerical performance of REPS-K methods, Fig. 2.2(a) shows the difference in the dimensionless Helmholtz free energy per diblock copolymer (DBC) chain $\beta f_c \equiv (N_A+N_B)\beta f$ as a function of the number of chain-contour discretization steps n_s given by various REPS-K methods from that given by REPS-4 at n_s=512, denoted by $\Delta(n_s,K) \equiv |\beta f_c(n_s,K) - \beta f_c(n_s=512,K=4)|$, for the lamellar phase formed by (both conformationally and compositionally) symmetric DBCs A-B of the "standard" model at $\chi_{AB}(N_A+N_B)$=100 (where we take $\{i,m\}$={A,B}). We see that at large n_s, $\Delta \propto n_s^{-2(K+1)}$ for K=1~3, indicating that REPS-K is a $2(K+1)^{\text{th}}$-order method as expected; for REPS-4, our n_s-values are not large enough before Δ approaches $\varepsilon_0=10^{-10}$. Note that the n_s-value needed to reach an accuracy of 10^{-8} in βf_c by REPS-3 is about 16 times smaller than REPS-1, which gives about one order of magnitude saving in the

GPU memory usage (see Sec. 2.5.1 below for more details). On the other hand, $n_K n_s$ is a good measure for the computing time of each AM iteration since FFTs are the most time-consuming part in SCF calculations; Fig. 2.2(b) shows that to reach an accuracy of 10^{-8} in βf_c, REPS-3 is about three times faster than REPS-1. Such comparisons of course depend on the ordered phase, the system parameters, and the free-energy accuracy to be reached. Figs.2.2(c) and 2.2(d) show another example of the σ phase formed by (both compositionally and conformationally) asymmetric A-B of the "standard" model at $\chi_{AB}(N_A+N_B)=40$; we see that to reach an accuracy of 10^{-5} in βf_c, REPS-2 has the least computing time and its GPU memory usage is the same as REPS-3 and -4 but much less than REPS-1. Other examples can be found in our recent work[39].

2.4 Implementation of Crystallographic FFT

For 3D spatially periodic ordered phases such as those formed by BCP self-assembly, while PSCF uses discrete Fourier transform (DFT) to convert between a uniform grid in the real

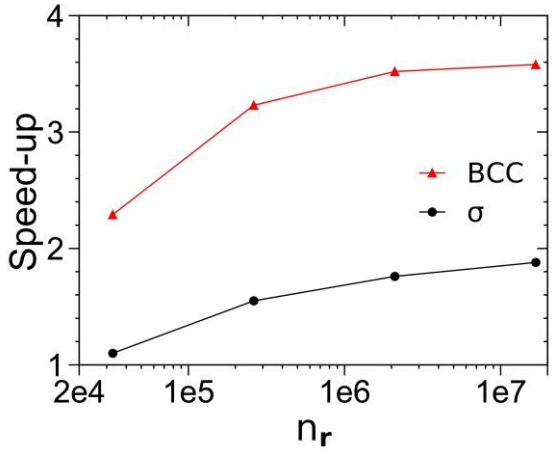

Figure 2.3. Semi-logarithmic plot of the speed-up by crystallographic FFT in the computing time of SCF calculations of the BCC and σ phases formed by DBCs of the "standard" model at $\chi_{AB}(N_A+N_B)=40$, $N_A/(N_A+N_B)=0.25$ and $b_A^2/b_B^2=4$, where the unit cell of BCC and σ is uniformly discretized into $n_r=m^3$ and $2m\times2m\times m$ grid points, respectively, the chain contour is uniformly discretized into $n_s=32$ steps, and REPS-1 is used. See the main text for more details.

Table 2.1. Size of various (real-number) arrays needed in SCF calculations of 3D ordered phases formed by BCPs. See the main text for more details.

Array Size	DFT	DCT
BCC/FCC/A15/H		
$q(\mathbf{r})$ and $\hat{q}(\mathbf{q})$	$2n_s n_\mathbf{r}$	$n_s n_\mathbf{r}/8$
$\omega(\mathbf{r})$ or $\phi(\mathbf{r})$	$n_\mathbf{r}$	$n_\mathbf{r}/8$
$\hat{\omega}(\mathbf{q})$ or $\hat{\phi}(\mathbf{q})$	n_*	$n_\mathbf{r}/8$
σ/Z		
$q(\mathbf{r})$ and $\hat{q}(\mathbf{q})$	$2n_s n_\mathbf{r}$	$n_s n_\mathbf{r}/4$
$\omega(\mathbf{r})$ or $\phi(\mathbf{r})$	$n_\mathbf{r}$	$n_\mathbf{r}/4$
$\hat{\omega}(\mathbf{q})$ or $\hat{\phi}(\mathbf{q})$	n_*	$n_\mathbf{r}/4$

space and that in the reciprocal space, PSCF+ uses crystallographic FFT that take advantage of the (partial) symmetry of an ordered phase to reduce the number of grid points (thus array sizes) used in the SCF calculation, thus both speeding up the calculation and reducing its memory usage. In particular, for ordered phases in the *Pmmm* supergroup, Qiang and Li[17] proposed to use the discrete cosine transform (DCT) of type II and its inverse transform, DCT of type III, to replace DFT and its inverse transform, respectively; this is implemented in PSCF+. Note that, while Qiang and Li implemented their own version of DCTs that fully makes use of the AVX2 SIMD instructions[17], this limits their implementation to CPUs only; instead, our DCTs are implemented on GPU that makes use of cuFFT[20] following Ref. 42.

Table 2.1 lists the size of various (real-number) arrays needed in SCF calculations of some 3D ordered phases formed by BCPs, where $q(\mathbf{r})$ represents the array for an (either forward or backward) propagator of a BCP component in the real space and $\hat{q}(\mathbf{q})$ the corresponding array in the reciprocal space, $\omega(\mathbf{r})$ ($\phi(\mathbf{r})$) represents the array for the conjugate (volume-fraction) field of a species in the real space and $\hat{\omega}(\mathbf{q})$ ($\hat{\phi}(\mathbf{q})$) the corresponding array in the reciprocal space, $n_\mathbf{r}$ denotes the total number of grid points used to uniformly discretize the unit cell of an ordered

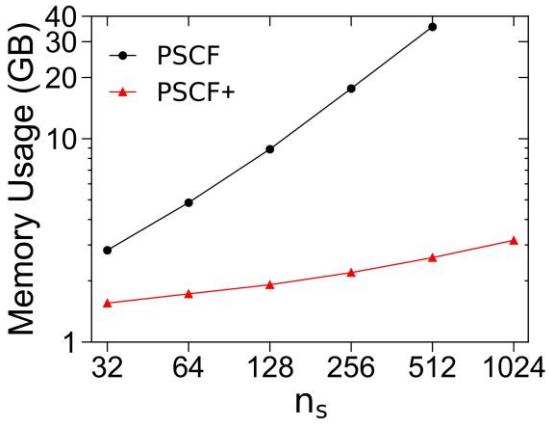

Figure 2.4. Logarithmic plot of the GPU memory usage of PSCF+ using the "slice" algorithm and that of PSCF (CUDA/C++ version) for SCF calculations of the BCC phase formed by DBCs of the "standard" model at $\chi_{AB}(N_A+N_B)=40$, $N_A/(N_A+N_B)=0.25$ and $b_A^2/b_B^2=4$, where the unit cell of BCC is uniformly discretized into 128^3 grid points (without using the crystallographic FFT) and the chain contour is uniformly discretized into n_s steps. See the main text for more details.

phase, and n_* denotes the corresponding number of symmetry-adapted basis functions in the reciprocal space[110] (which is usually one or two orders of magnitude smaller than $n_\mathbf{r}$, depending on both the $n_\mathbf{r}$-value and the symmetry of the ordered phase). Note that the factor of two for $q(\mathbf{r})$ and $\hat{q}(\mathbf{q})$ in PSCF is because the DFT (and its inverse transform) is performed out-of-place there, while in PSCF+ the DCTs are performed in-place; our implementation of the crystallographic FFT therefore achieves about one order of magnitude saving in the GPU memory usage in most cases.

Fig. 2.3 shows that the crystallographic FFT can also achieve a few times speed-up in the computing time of SCF calculations of ordered phases.

Finally, we note that the crystallographic FFT is currently implemented in PSCF+ only for the "standard" model, and will be implemented for other models in PSCF+ in the near future.

2.5 Implementation of the "Slice" Algorithm

Table I above shows that storing the propagators uses the most memory in SCF

calculations. In particular, $n_{\mathbf{r}}$ can be on the order of 10^6 or larger for 3D calculations, while n_s can be on the order of 10^2 or larger as shown in Fig. 2.2 above; since the GPU memory is currently limited to tens of Gigabytes (GBs), we have implemented the "slice" algorithm proposed in Ref. 43 to greatly reduce the memory usage in PSCF+.

For the CGC model used in PSCF, the architecture of an ***acyclic*** BCP chain, which consists of $n_B \geq 1$ (linear homopolymer) blocks connecting $n_V = n_B + 1$ vertices (note that an acyclic chain can be constructed by adding, in each step, a block and a new vertex to an existing vertex), including both joints (J) and free ends (E), is described by specifying the vertices j and $k \in [0, n_B]$ connected by each block i (=0,…,n_B−1). Block i of a BCP component has two propagators $q_i(\mathbf{r},s)$ and $q_i^\dagger(\mathbf{r},s)$, where s=0,…,$N_i\Delta s$ with N_i being the number of steps along the chain contour into which the block is uniformly discretized, $\Delta s \equiv f_i / N_i$ being the step-size along the chain contour, and f_i being the volume fraction of block i in the BCP chain; note that in the REPS-K method (K=0,…,4) described in Sec. 2.3 above, N_i must be an integer multiple of 2^K (*i.e.*, $M_i \equiv N_i / 2^K$ must be a positive integer). In each AM iteration, PSCF calculates the propagators in two steps: in Step I it solves all the forward propagators $\{q_i(\mathbf{r},s)\}$, and in Step II it solves all the backward propagators $\{q_i^\dagger(\mathbf{r},s)\}$; that is, for each BCP component in the system, the labeling of the two end-segments s=0 and s=f_i for all its blocks and the order of solving all its propagators are determined automatically in PSCF based on its chain architecture.

To calculate the contribution of block i to the volume-fraction field of its segment type, we need to evaluate $\int_0^{f_i} \mathrm{d}s q_i(\mathbf{r},s) q_i^\dagger(\mathbf{r},s) \approx \Delta s \sum_{k'=1}^{M_i} \sum_{k=0}^{2^K} c_k q_{i,2^K(k'-1)+k} q^\dagger_{i,2^K(k'-1)+k}$ at all $\mathbf{r}$ using the Romberg integration (denoted by RI-K), where c_k's are the coefficients used in RI-K,

$q_{i,j} \equiv q_i(\mathbf{r}, j\Delta s)$, and $q^{\dagger}_{i,j} \equiv q^{\dagger}_i(\mathbf{r}, j\Delta s)$. Usually, such integrals are calculated after all the propagators are solved and stored. The "slice" algorithm proposed in Ref. 43, however, is based on the fact that once the contribution of segment *s* on block *i* to the above integral (and stresses) is calculated, $q_{i,j}$ and $q^{\dagger}_{i,j}$ are no longer needed in the current AM iteration in SCF calculations. In particular, we store $q_{i,j}$ for all *i* only at their "check points", where *j*=0 or $j = N_i - \left(\sum_{i=1}^{l} i - 1\right) = N_i - \frac{l(l+1)}{2} + 1$ for ***integer*** values of $l \in [1, l_{\max})$ (in the ***descending*** order of *l*) in Step I above; to ensure *j*>0 in the latter case, one finds $l_{\max} = \left(\sqrt{8N_i + 9} - 1\right)\Big/2$. This splits block *i* into (at least two) "slices", each containing one "check point" corresponding to the smallest *j*-value in the "slice". In Step II above, we only store $q^{\dagger}_{i,j^*}$ for the current value of j^* (=N_i,N_i–1,…,0), and calculate (accumulate) the above integral "slice" by "slice"; note that $q^{\dagger}_{i,j^*-1}$ needs to be calculated out-of-place in REPS-*K* due to its successive halving of Δ*s*. In the "slice" containing j^*, if q_{i,j^*} is available (*e.g.*, when j^* is a check point), we then directly calculate the contribution of j^* to the above integral; otherwise, we re-calculate all $q_{i,j}$ from the "check point" in the "slice" and store them in the same places as the no-longer-needed *q*-values, then calculate their contribution to the above integral.

We take N_i=8 to illustrate the procedure of the "slice" algorithm as follows:

(1) $q_{i,j=0}$ is the ***known*** initial condition of the forward propagator. Since *j*=0 is a "check point", $q_{i,j=0}$ is stored in `q[0]`, the first element of a ***four-element array*** for storing the forward propagators. $q_{i,j}$ for *j*=1,2,…,8 are then obtained ***sequentially*** by solving the MDE for the forward propagator via, for example, the REPS-3 method; since here only *j*=3, 6 and 8 (*i.e.*,

l=3, 2 and 1, respectively) are "check points", $q_{i,j=3}$, $q_{i,j=6}$ and $q_{i,j=8}$ are stored in `q[1]`, `q[2]` and `q[3]`, respectively. We therefore have four "slices".

(2) At the end of Step I, all the forward propagators are calculated, which then gives the normalized single-chain partition function of each component and $q^{\dagger}_{i,j=N_i}$ (*i.e.*, the initial condition of the backward propagator). Since $j=N_i$ (*i.e.*, l=1) is always a "check point" (which is the only *j*-value contained in "Slice" 1), $q^{\dagger}_{i,j=N_i}$ is stored as `qd`, the ***variable*** for storing the backward propagators, and the contribution of segment $s=f_i$ to the above integral, $c_8 q_{i,j=8} q^{\dagger}_{i,j=8}$, is calculated using `q[3]` and `qd`.

(3) "Slice" 2 contains j=7 and 6. $q^{\dagger}_{i,j=7}$ is obtained from `qd` by solving the MDE for the backward propagator and stored in `qd` (which is overwritten since $q^{\dagger}_{i,j=8}$ is no longer needed). Since j=7 is not a "check point", $q_{i,j=7}$ is calculated (again) from `q[2]` by solving the MDE for the forward propagator and stored in `q[3]`. The contribution $c_7 q_{i,j=7} q^{\dagger}_{i,j=7}$ to the above integral is then calculated (and accumulated) using `q[3]` and `qd`. Similar to $q^{\dagger}_{i,j=7}$, $q^{\dagger}_{i,j=6}$ is obtained from `qd` and then stored in `qd`. Since j=6 is a "check point", however, the contribution $c_6 q_{i,j=6} q^{\dagger}_{i,j=6}$ to the above integral is calculated (and accumulated) using `q[2]` and `qd`.

(4) "Slice" 3 contains j=5, 4 and 3. Similar to (3), $q_{i,j=4}$ is calculated (again) from `q[1]` and stored in `q[2]`, and $q_{i,j=5}$ is then calculated (again) from `q[2]` and stored in `q[3]`; this clever design, where the number of *j*-values contained in the "slices" follow an arithmetic sequence of 1,2,3,…, efficiently re-uses the no-longer-needed storage for the forward propagators. For j=5, 4 and 3, $q^{\dagger}_{i,j}$ is obtained from `qd` and then stored in `qd`, and the contribution $c_j q_{i,j} q^{\dagger}_{i,j}$ to the above integral is then calculated (and accumulated) using `q[3]`,

`q[2]` and `q[1]`, respectively, and `qd`.

(5) The last "slice", "Slice" 4, contains the rest j-values (*i.e.*, j=2, 1 and 0). Similar to (4), $q_{i,j=1}$ is calculated (again) from `q[0]` and stored in `q[1]`, and $q_{i,j=2}$ is then calculated (again) from `q[1]` and stored in `q[2]`. For j=2, 1 and 0, $q^{\dagger}_{i,j}$ is obtained from `qd` and then stored in `qd`, and the contribution $c_j q_{i,j} q^{\dagger}_{i,j}$ to the above integral is then calculated (and accumulated) using `q[2]`, `q[1]` and `q[0]`, respectively, and `qd`.

Similarly, to calculate the contribution of block i to the system stresses[38] (which vanish when the bulk periodicity of an ordered phase formed by BCP self-assembly is found), we evaluate $\int_0^{f_i} \mathrm{d}s \hat{q}_i(\mathbf{q}, s)\hat{q}^{\dagger}_i(-\mathbf{q}, s)$ in the same way as above. Compared to the usual approach of calculating and storing all propagators before calculating the volume-fraction fields, the "slice" algorithm reduces the memory usage by a factor of $\sqrt{2N_i}$ for large N_i at the cost of increasing the computation by 50% (*i.e.*, solving $\{q_{i,j}\}$ twice). Fig. 2.4 compares the GPU memory usage of PSCF+ using the "slice" algorithm with that of the CUDA/C++ version of PSCF for SCF calculations of the BCC phase formed by DBCs of the "standard" model.

Finally, we note that the "slice" algorithm is currently implemented in PSCF+ only for the CGC model, and will be implemented for discrete chain models in PSCF+ in the near future.

2.6 Other Improvement

2.6.1 Solving SCF equations

As aforementioned in Sec. 2.4, the SCF equations are solved with AM combined with a variable-cell method[16] in PSCF. Since Eq. 2.4 gives only up to six equations, we focus on solving other SCF equations here. For incompressible systems, a conjugate field $\xi(\mathbf{r})$ enforcing the incompressibility constraint is needed and all the conjugate fields (*i.e.*, $\omega_m(\mathbf{r})$ for all m and

$\xi(\mathbf{r})$) can be shifted by an arbitrary constant as aforementioned in Sec. 2.2.4, which is fixed by setting $\hat{\xi}(\mathbf{q}=\mathbf{0})=0$ in PSCF; Eq.(2.2) then gives $\hat{\boldsymbol{\omega}}(\mathbf{q}=\mathbf{0})=\mathbf{X}\overline{\boldsymbol{\phi}}$, where $\hat{\boldsymbol{\omega}}(\mathbf{q})$ and $\overline{\boldsymbol{\phi}}=\hat{\boldsymbol{\phi}}(\mathbf{q}=\mathbf{0})$ are column vectors with their m^{th} (m=1,…,n_m) element being $\hat{\omega}_m(\mathbf{q})$ and $\overline{\phi}_m=\hat{\phi}_m(\mathbf{q}=\mathbf{0})$, respectively, and $\mathbf{X}$ is an $n_m\times n_m$ matrix with its (m,m')-element being $\chi_{mm'}$.[16] With $\hat{\boldsymbol{\omega}}(\mathbf{q}\neq\mathbf{0})$ taken as the independent variables, the residual of Eq. (2.2) is calculated as $\boldsymbol{\varepsilon}(\mathbf{q}\neq\mathbf{0})=\mathbf{X}\hat{\boldsymbol{\phi}}(\mathbf{q}\neq\mathbf{0})-\left(\mathbf{I}-\mathbf{1}\mathbf{1}^T\mathbf{X}^{-1}/\mathbf{1}^T\mathbf{X}^{-1}\mathbf{1}\right)\hat{\boldsymbol{\omega}}(\mathbf{q}\neq\mathbf{0})$, where $\mathbf{I}$ denotes the $n_m\times n_m$ identity matrix, $\mathbf{1}$ denotes the column vector having n_m elements of 1, and the column vector $\hat{\boldsymbol{\phi}}(\mathbf{q}\neq\mathbf{0})$ is obtained from the propagators at the given $\hat{\boldsymbol{\omega}}(\mathbf{q})$.[16] Clearly, this approach used in PSCF requires $\mathbf{X}$ be invertible, which is not the case when all the χ-parameters of some monomer type (*e.g.*, an athermal solvent or the JSs) are 0.

In PSCF+, to avoid the above problem we write all the linear SCF equations, Eqs. (2.1) ***and*** (2.2), in a block matrix form as $\begin{bmatrix}\mathbf{X} & \mathbf{1}\\ \mathbf{1}^T & 0\end{bmatrix}\begin{bmatrix}\hat{\boldsymbol{\phi}}(\mathbf{q})\\ \xi(\mathbf{q})\end{bmatrix}=\begin{bmatrix}\hat{\boldsymbol{\omega}}(\mathbf{q})\\ \delta_{\mathbf{q},\mathbf{0}}\end{bmatrix}$; different from $\mathbf{X}$, the (n_m+1)×(n_m+1) matrix $\begin{bmatrix}\mathbf{X} & \mathbf{1}\\ \mathbf{1}^T & 0\end{bmatrix}$ is always invertible, and we use $\mathbf{A}$ to denote the $n_m\times n_m$ submatrix obtained by deleting the last row and the last column of $\begin{bmatrix}\mathbf{X} & \mathbf{1}\\ \mathbf{1}^T & 0\end{bmatrix}^{-1}$. With $\hat{\boldsymbol{\omega}}(\mathbf{q}\neq\mathbf{0})$ taken as the independent variables, the residual of Eq. (2.2) is then calculated as $\boldsymbol{\varepsilon}(\mathbf{q}\neq\mathbf{0})=\hat{\boldsymbol{\phi}}(\mathbf{q}\neq\mathbf{0})-\mathbf{A}\hat{\boldsymbol{\omega}}(\mathbf{q}\neq\mathbf{0})$; as in PSCF, here we set $\hat{\xi}(\mathbf{q}=\mathbf{0})=0$ and obtain $\hat{\boldsymbol{\phi}}(\mathbf{q}\neq\mathbf{0})$ from the propagators at the given $\hat{\boldsymbol{\omega}}(\mathbf{q})$.

2.6.2 Automated calculation along a path (ACAP)

Since SCF equations are highly nonlinear, having a good initial guess is very important in

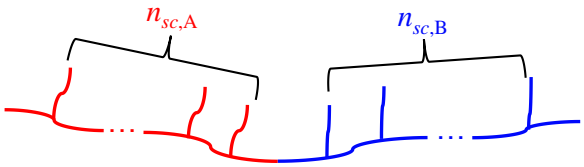

Figure 2.5: Illustration of bbDBC A-B in the "standard" model with $n_{sc,P}$ side-chains evenly grafted to the backbone of the P(=A,B) block, thus forming a bb homopolymer of type P. The bbDBC shown above consists of $2n_{sc,A}+1$ LHBs of type A each having the volume fraction of $f_{sc,A}$ and $2n_{sc,B}+1$ LHBs of type B each having the volume fraction of $f_{sc,B}$, with $(2n_{sc,A}+1)f_{sc,A} + (2n_{sc,B}+1)f_{sc,B} = 1$.

practice as it determines not only which final solution (corresponding to a phase in BCP self-assembly) can be obtained but also how many iteration steps the solver (*e.g.*, AM) takes to converge these equations. While PSCF includes methods for generating initial guesses for a given ordered phase,[2] ACAP is a simple and robust strategy that has been successfully used by one of the authors (QW) in nearly all his work involving solving nonlinear equations since 2000. Let $\mathbf{f}(\mathbf{x};p)=\mathbf{0}$ be the set of nonlinear equations to be solved at some value of parameter p (*e.g.*, $\chi_{mm'}$); the basic idea of ACAP is to use the converged solution $\mathbf{x}^*(p')$ as the initial guess at $p'+\delta p$ and vary the parameter value from p' to p in a stepwise manner (*i.e.*, along a path) by ***automatically adjusting*** δp (depending on whether or not the equations are converged) in each step. While ACAP is similar to the "SWEEP" command (which uses ***fixed*** δp) in PSCF, automatically adjusting δp is the key for ACAP to be successful. This can be simply done by using a factor $\alpha>1$: if the equations are converged in a step having step size δp, then $\alpha\delta p$ is taken as the step size for the next step; otherwise, one repeats the calculation in this step except with $\delta p/\alpha$ taken as the step size. Of course, one can also limit the largest and smallest absolute value of the step size in ACAP. ACAP works with any continuous parameter p; note, however, that the block volume fraction cannot be varied continuously, even for the CGC model due to the numerical integration along the block contour.

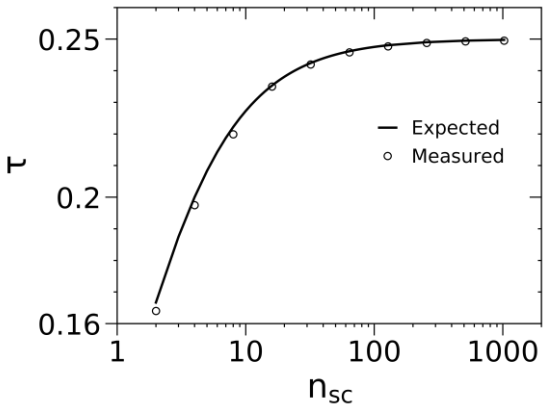

Figure 2.6. Semi-logarithmic plot of the speed-up τ *vs.* the total number of side-chains n_{sc} at fixed degree of segregation between the A and B blocks χN=60 for symmetric bbDBC.

ACAP described above involves only one (ordered) phase and is suitable for computing, *e.g.*, the βf-curve of that phase. We have also implemented ACAP to efficiently compute the phase boundary between two given phases in PSCF+. For an incompressible system of neat BCP melts, this requires solving a single equation

$$\beta f_{\mathrm{I}}(x;p) = \beta f_{\mathrm{II}}(x;p) \tag{2.5}$$

for two phases (I and II), where, for example, in the "standard" model of neat DBC melts x and p can be taken as $\chi_{AB}(N_A+N_B)$ and b_A^2/b_B^2, respectively[39]. While the basic idea of ACAP here is the same as described above, some bookkeeping is needed when both I and II are ordered phases; in particular, we solve Eq. (2.5) with the Ridders' method[44], which requires an estimated interval bracketing the solution of x at given p (or that of p at given x). This can be compared with the conventional approach of computing the phase boundary, where at each given p-value, βf_{I} and βf_{II} at several ***predetermined*** x-values are calculated and then interpolated to find an approximate solution (the accuracy of which depends on that of the interpolation, which is often not estimated) to Eq.(2.5); in contrast, the Ridders' method can quickly solve Eq. (2.5) to a specified accuracy, and the ACAP here can efficiently trace out the phase boundary $x(p)$ between the two phases.

2.6.2 Solving MDE equations

Consider a bottlebrush (bb) homopolymer consisting of a backbone (denoted by the subscript "*b*"), which has N_b segments with the statistical segment length a_b, and n_{sc} side-chains (denoted by the subscript "*sc*"), each of which has N_{sc} segments with the statistical segment length a_{sc}, evenly grafted to the backbone. In the CGC model, we have $N_b \to \infty$ and $a_b \to 0$ at finite $R_{e,b} \equiv \sqrt{N_b} a_b$ and similarly $N_{sc} \to \infty$ and $a_{sc} \to 0$ at finite $R_{e,sc} \equiv \sqrt{N_{sc}} a_{sc}$. For the bbDBC I illustrated in Fig. 2.5, the $n_{sc,\mathrm{P}}$ side-chains each having the volume fraction of $f_{sc,\mathrm{P}}$ divide the P backbone into $n_{sc,\mathrm{P}}+1$ P linear homopolymer blocks (LHBs) and we require that all the $2n_{sc,\mathrm{P}}+1$ P LHBs (including the side-chains) be the same (*i.e.*, $N_{b,\mathrm{P}} / \left(n_{sc,\mathrm{P}} + 1 \right) = N_{sc,\mathrm{P}}$). In the self-consistent field (SCF) calculations of the "standard" model (*i.e.*, incompressible melts of CGCs with the Dirac δ-function non-bonded interaction), each LHB has a forward and a backward propagator, and all the $n_{sc,\mathrm{P}}+1$ forward propagators (each starting from a free P end) are identical. We therefore need to calculate only $3n_{sc,\mathrm{A}}+3n_{sc,\mathrm{B}}+4$ different propagators; by further requiring $N_{sc,\mathrm{A}}=N_{sc,\mathrm{B}} \equiv N_{sc}$ (and using the same chain-contour discretization for the two blocks), we have the same computing time for all the propagators and thus achieve a speed-up (*i.e.*, less computation) of $\tau = \left(n_{sc,\mathrm{A}} + n_{sc,\mathrm{B}} \right) / 4 \left(n_{sc,\mathrm{A}} + n_{sc,\mathrm{B}} + 1 \right)$ compared to PSCF.

For ***symmetric*** bbDBC shown in Fig. 2.5 (where $n_{sc,\mathrm{A}}=n_{sc,\mathrm{B}}$ and $f_{sc,\mathrm{A}}=f_{sc,\mathrm{B}} \equiv f$), this becomes $\tau = n_{sc} / 4 \left(n_{sc} + 1 \right)$ with $n_{sc} \equiv n_{sc,\mathrm{A}}+n_{sc,\mathrm{B}}$ being the total number of side-chains. Fig. 2.6 shows that the actual speed-up $\tau \equiv 1 - t_+ / t$, where t_+ and t are the measured computing time for calculating the propagators in PSCF+ and PSCF, respectively, for 1D calculations of the lamellae formed by the symmetric bbDBC, is indeed given by the above result. We further note that PSCF+ also achieves the corresponding GPU memory saving in storing the computed propagators.

2.7 Summary

To summarize, we have extended the C++/Cuda version[18] of PSCF[2, 19], an open-source software package for polymer self-consistent field (SCF) calculations of the "standard" model (*i.e.*, an incompressible melt of continuous Gaussian chains (CGCs) with the Dirac δ-function non-bonded interactions) of block copolymer (BCP) self-assembly, to systems of various discrete-chain models and finite-range non-bonded interactions. We have also greatly improved several aspects of PSCF, including calculations of the "standard" model. PSCF is designed to perform unit-cell calculations of the self-assembled periodic structures of arbitrary mixtures of flexible and acyclic BCPs (including homopolymers and small-molecule solvents), and its C++/Cuda version provides a nice framework for SCF calculations on GPUs. Unfortunately, the "standard" model simply cannot be used in molecular (*i.e.*, Monte Carlo and molecular dynamics) simulations, and also leads to the ultraviolet divergence that is problematic in field-theoretic simulations (FTS)[34, 35]. Our extended and improved version of PSCF, named PSCF+, is freely available at https://github.com/qwcsu/PSCFplus.

PSCF+ runs on GPU and allows various combinations of chain-connectivity models (including CGC, discrete Gaussian chains, and freely jointed chains), non-bonded isotropic pair (including the Dirac δ-function, soft-sphere (SS), dissipative particle dynamics (DPD), and Gaussian) potentials and system compressibility (incompressible *vs.* compressible); note that a model system of discrete chains with the Dirac δ-function non-bonded potential leads to unphysical results for BCP self-assembly[24, 25], and that only compressible systems of discrete chains with the SS or DPD potential can be directly used in molecular simulations. It therefore enables direct comparisons between the SCF results with those obtained from molecular simulations or FTS[34] of the ***same*** model system, thus without any parameter-fitting, to

unambiguously quantify the fluctuation/correlation effects inherently neglected by the SCF theory.

On the other hand, we have implemented various Richardson-extrapolated pseudo-spectral methods (*i.e.*, REPS-*K* with *K*=2,3,4) for solving the modified diffusion equations and the corresponding Romberg integration (RI-*K*) methods for calculating the volume-fraction fields, which give more accurate results and greatly saves the memory usage than the REPS-1 method used in PSCF. We have also implemented the crystallographic fast Fourier transform proposed by Qiang and Li[17], which uses the discrete cosine transform (DCT) of type II and its inverse transform, DCT of type III, to replace the discrete Fourier transform and its inverse transform, respectively, to take advantage of the partial symmetry of the *Pmmm* supergroup to reduce the number of grid points (thus array sizes) used in the SCF calculation, thus both reducing its memory usage (as summarized in Table 2.1) and speeding up the calculation. We have further implemented the "slice" algorithm proposed by Qiang and Li[43], which reduces the memory usage for storing the propagators of block i by a factor of $2\sqrt{N_i}$ for large values of the block-contour discretization N_i at the cost of increasing the computation by 50%. While these last two improvements are implemented at present only for the "standard" model and CGCs, respectively, we plan to extend them to discrete chains with finite-range non-bonded interactions soon.

Finally, we have implemented a new strategy of iteratively solving the SCF equations for incompressible systems, which allows the use of athermal solvent or joint segment having no Flory-Huggins-type interaction with all other species in the system. We have also implemented the strategy of automated calculation along a path, which automatically adjusts the step size and makes the calculations of free-energy curves and boundaries between two phases much more convenient and efficient. While our current method for calculating phase boundaries is strictly

valid only for incompressible systems[45], we plan to extend it to compressible systems in the near future.

REFERENCES

[1] https://pscf-home.cems.umn.edu/fortran.

[2] A. Arora, J. Qin, D. C. Morse, K. T. Delaney, G. H. Fredrickson, F. S. Bates, and K. D. Dorfman, Macromolecules 49 (13), 4675-4690 (2016).

[3] F. S. Bates and G. H. Fredrickson, Annu. Rev. Phys. Chem. 41, 525-557 (1990).

[4] F. S. Bates and G. H. Fredrickson, Phys. Today 52 (2), 32-38 (1999).

[5] F. S. Bates, M. A. Hillmyer, T. P. Lodge, C. M. Bates, K. T. Delaney, and G. H. Fredrickson, Science 336 (6080), 434-440 (2012).

[6] S. F. Edwards, P. Phys. Soc. 85, 613-624 (1965).

[7] G. H. Fredrickson, The equilibrium theory of inhomogeneous polymers. Oxford University Press: New York, (2006).

[8] G. J. Fleer, M. A. Cohen Stuart, J. M. H. M. Scheutjens, T. Cosgrove, and B. Vincent, Polymers at interfaces. 1st ed.; Chapman & Hall: London; New York, (1993).

[9] M. W. Matsen and M. Schick, Phys. Rev. Lett. 72 (16), 2660-2663 (1994).

[10] G. Tzeremes, K. K. Rasmussen, T. Lookman, and A. Saxena, Phys. Rev. E 65 (4), 041806 (2002).

[11] H. D. Ceniceros and G. H. Fredrickson, Multiscale Model. Simul. 2 (3), 452-474 (2004).

[12] E. W. Cochran, C. J. Garcia-Cervera, and G. H. Fredrickson, Macromolecules 39 (7), 2449-2451 (2006).

[13] E. W. Cochran, C. J. Garcia-Cervera, and G. H. Fredrickson, Macromolecules 39 (12), 4264-4264 (2006).

[14] A. Ranjan, J. Qin, and D. C. Morse, Macromolecules 41 (3), 942-954 (2008).

[15] M. W. Matsen, Eur. Phys. J. E 30 (4), 361-369 (2009).

[16] A. Arora, D. C. Morse, F. S. Bates, and K. D. Dorfman, J. Chem. Phys. 146 (24), 244902 (2017).

[17] Y. Qiang and W. Li, Macromolecules 53 (22), 9943-9952 (2020).

[18] https://github.com/dmorse/pscfpp.

[19] G. K. Cheong, A. Chawla, D. C. Morse, and K. D. Dorfman, Eur. Phys. J. E 43 (2), 15 (2020).

[20] https://docs.nvidia.com/cuda/pdf/CUFFT_Library.pdf.

[21] Q. Wang, J. Chem. Phys. 129 (5), 054904 (2008).

[22] Q. Wang, Soft Matter 5 (22), 4564-4567 (2009).

[23] Q. Wang, Soft Matter 6 (24), 6206-6207 (2010).

[24] M. W. Matsen, Macromolecules 45 (20), 8502-8509 (2012).

[25] P. Sandhu, J. Zong, D. Yang, and Q. Wang, J. Chem. Phys. 138 (19), 194904 (2013).

[26] P. Zhang, B. Li, and Q. Wang, Macromolecules 44 (19), 7837-7852 (2011).

[27] P. Zhang, B. Li, and Q. Wang, Macromolecules 45 (5), 2537-2550 (2012).

[28] P. Zhang and Q. Wang, Soft Matter 9 (47), 11183-11187 (2013).

[29] P. Zhang and Q. Wang, J. Chem. Phys. 140, 044904 (2014).

[30] D. Yang and Q. Wang, J. Chem. Phys. 140, 194902 (2013).

[31] P. Zhang and Q. Wang, Macromolecules 52 (15), 5777-5790 (2019).

[32] P. Zhang and Q. Wang, Macromolecules 53 (20), 8883-8888 (2020).

[33] J.-P. Wu, B.-H. Li, and Q. Wang, Chin. J. Polym. Sci. 40 (4), 413-420 (2022).

[34] G. H. Fredrickson, V. Ganesan, and F. Drolet, Macromolecules 35 (1), 16-39 (2002).

[35] K. T. Delaney and G. H. Fredrickson, J. Phys. Chem. B 120 (31), 7615-34 (2016).

[36] Q. Wang, Polymers 15 (5), 1180 (2023).

[37] Q. Wang, Chin. J. Polym. Sci. 42, 1-12 (2023).

[38] C. A. Tyler and D. C. Morse, Macromolecules 36 (21), 8184-8188 (2003).

[39] J. He and Q. Wang, Polymers, submitted (2023).

[40] W. H. Press, Chap. 4.3. In Numerical recipes in C: The art of scientific computing, 2nd ed.; Cambridge University Press: Cambridge; New York, (1992).

[41] M. Dong and Q. Wang, J. Chem. Phys. 126 (23), 234902 (2007).

[42] M. Ren, Y. Gao, G. Wang, and X. Liu, In 2020 IEEE Intl Conf on Parallel & Distributed Processing with Applications, Big Data & Cloud Computing, Sustainable Computing & Communications, Social Computing & Networking, 2020; pp 57-66.

[43] Y. Qiang, Chap. 6.3.2 in The High-Performance Algorithms for Self-Consistent Field Theory. PhD Thesis, Fudan University, Shanghai, China, (2022).

[44] W. H. Press, Chap. 9.2. In Numerical recipes in C: The art of scientific computing, 2nd ed.; Cambridge University Press: Cambridge; New York, (1992).

[45] J. Zong and Q. Wang, J. Chem. Phys. 143 (18), 184903 (2015).

3 FRANK-KASPER PHASES OF DIBLOCK COPOLYMER MELTS: SELF-CONSISTENT FIELD RESULTS OF TWO COMMONLY USED MODELS

3.1 Introduction

Initially found in metallic alloys, Frank-Kasper (FK) phases refer to a class of complex structures where coordination polyhedra[1] have only triangular faces; in their seminal work, Frank and Kasper deduced the general principles regarding the combination of four types of such polyhedra into full structures with coordination numbers of 12, 14, 15 and 16, and applied them to the analysis and classification of some FK phases.[1, 2] The more recent discovery of FK phases in various soft materials,[3-8] particularly in block copolymers (BCPs),[9-17] indicates the existence of certain universal principles governing the formation of these complex structures in a wide range of condensed matter at different length scales. From fundamental viewpoint, the delicate balance of the energetic repulsion between various blocks and their entropic stretching under the space-filling requirement in BCP self-assembly gives somewhat different formation mechanisms of FK phases from the packing of hard spheres in metallic alloys, thus making these complex structures more controllable. For example, blending BCP with homopolymer or another BCP of different chain length and/or composition gives an easy way of tuning the FK structures experimentally.[9-11, 15, 18-26] Hereafter we limit our discussion to the spherical FK phases formed in the simplest BCP system – neat diblock copolymer (DBC) melts A-B, where A denotes the minority block whose volume fraction $f<1/2$.

σ and A15 are, respectively, the first FK phase reported in experiments[12] and studied by the polymer self-consistent field (SCF) calculations[27] of A-B. Their stability can be attributed to the conformational asymmetry between the two blocks, characterized by $\varepsilon\equiv(a_A/a_B)^2$,[28] where a_P (P=A,B) denotes the statistical segment length of the P block calculated using the same reference

volume for A- and B-segments. To date, several experimental groups have reported σ in poly(lactide)-poly(isoprene) (PLA-PI with $\varepsilon=(a_{PLA}/a_{PI})^2\approx1.32$)[12, 16, 29-31], PLA-poly(ethylethylene) (PLA-PEE with $\varepsilon=(a_{PLA}/a_{PEE})^2\approx1.68$)[21], PLA-poly(dodecyl acrylate) (PLA-PDDA with $\varepsilon=(a_{PLA}/a_{PDDA})^2\approx3.4$)[14, 32], poly(trifluoroethyl acrylate)-PDDA (PF-PDDA with $\varepsilon\equiv(a_{PF}/a_{PDDA})^2\approx2.0$)[32], PF-poly(dimethylsiloxane) (PF-PDMS with $\varepsilon=(a_{PF}/a_{PDMS})^2\approx2.2$)[33, 34], poly(ethylene oxide)-poly(2-ethyl hexylacrylate) (PEO-PA with $\varepsilon\equiv(a_{PEO}/a_{PA})^2\approx3.5$)[35], and PEP-PDMS (with $\varepsilon\equiv(a_{PEP}/a_{PDMS})^2\approx1.6$)[36]. Similarly, A15 has been found in PLA-PDDA[14, 32], PF-PDDA[37], and PF-PDMS[34].

In comparison, other FK phases have been much less studied. Kunieda and co-workers suggested C15 formed in PEO-PDMS[17], F. S. Bates and co-workers studied metastable C14 and C15 formed in PLA-PI[16, 38], and very recently Ryu and co-workers reported stable C14 formed in PF-PDMS[33, 34].

On the other hand, using SCF calculations, Li and co-workers first proposed that the stability of σ formed in A-B is due to the conformational asymmetry between the two blocks; they constructed phase diagrams in the χN-f plane, where χ denotes the Flory-Huggins parameter characterizing the repulsion between A and B segments and N denotes the copolymer chain length, and found stable σ (*i.e.*, having the lowest dimensionless mean-field Helmholtz free energy per chain βf_c, where $\beta\equiv1/k_BT$ with k_B being the Boltzmann constant and T the thermodynamic temperature) in A-B with ε=2.25 and 4.[39] Dorfman and co-workers reported similar SCF results over a range of χN, f and ε-values, and found that C14, C15 and Z are metastable with their βf_c only a few thousandth higher than the stable phase.[16] Grason and co-workers studied the structure and stability of eleven FK phases (including A15, σ, C14, C15, H,

M, P, Z, δ, μ, and $p\sigma$) formed in A-B using SCF calculations at χN=25 and ε=4 and a strong-stretching theory[40-42], and found that A15 and σ are the only two stable FK phases while H is the most competitive metastable phase.[43] Finally, Fredrickson and co-workers reported the most recent SCF phase diagrams of A-B in the χN-f (at ε=9) and ε-f (at χN=40) planes, and found that A15 is stable around f=0.3 for ε>4.4 and that σ is stable at smaller ε, f and χN than A15, with C14 and C15 being metastable.[14] All these SCF calculations for A-B reported to date[14, 16, 39, 43] are for the "standard" model (*i.e.*, incompressible melts of continuous Gaussian chains with the Dirac δ-function repulsion between A and B segments)[44, 45]. While SCF theory[46] can be considered as the most successful molecular-level theory for BCP assembly partly due to its well-developed numerical calculations[45, 47-54], as a mean-field theory it neglects the effects of system fluctuations/correlations, thus corresponding to the limit of $\bar{N}\to\infty$, where the invariant degree of polymerization[55] $\bar{N} \equiv \left(nR_e^3/V\right)^2$ controls the fluctuations/correlations in a melt of n DBC chains in volume V with R_e being the root-mean-square chain end-to-end distance. In comparison, all DBC melts forming FK phases in experiments to date[12, 14, 16, 17, 21, 29-35, 37, 38] have $25 < \bar{N} < 385$, with only one exception[36] of $\bar{N}\approx 520$. We also note that the aforementioned SCF calculations show that σ is unstable for ε<2.1,[14, 16, 39] thus overestimating the ε-value needed for obtaining σ and A15 in experiments. Direct comparison between SCF and molecular (*i.e.*, molecular dynamics or Monte Carlo) simulation or field-theoretic simulation[56] results based on the same model system, thus without any parameter-fitting, is the ***only*** way to unambiguously quantify the fluctuation/correlation effects neglected by the former. The "standard" model, however, ***cannot*** be used in molecular simulations due to its infinite number of segments on each chain (*i.e.*, the continuous Gaussian chain model), its zero-range (*i.e.*, the Dirac δ-function)

interaction potential, and its incompressibility constraint imposed at all spatial positions in continuum. It also causes the problem of ultraviolet divergence that is difficult to handle in field-theoretic simulations.[57]

As the first step towards the direct comparisons between SCF and molecular simulation results of the FK phases formed in A-B, in this work we propose a model system for conformationally asymmetric A-B that can be used in the dissipative particle dynamics (DPD) simulations of DBC melts[58], which consists of discrete Gaussian chains interacting with the DPD non-bonded potentials and is referred to as the DPD model, and construct its SCF phase diagrams at f=0.2 and 0.3 (*i.e.*, focusing on the FK phases) by varying χN and $\varepsilon \equiv (b_A/b_B)^2$ with b_P being the effective bond length of the P-block, while fixing N=10, $b_B = \sqrt{3}/2$ (in units of the interaction range of the DPD potential) and the system compressibility N/κ=50π (for nearly incompressible melts) as commonly used in the DPD simulations[58]. In addition, the SCF phase diagrams are compared with those of the "standard" model.

3.2 Model and Method

3.2.1 The DPDC model and its SCF calculations

Our DPD model for diblock copolymer A-B melts consists of n chains, each having N_A segments of type A followed by N_B segments of B, in volume V at thermodynamic temperature T. The volume fraction of the A-block in the copolymer is $f \equiv N_A/N$ with $N \equiv N_A+N_B$. The chain connectivity is described by the discrete Gaussian chain model with an effective bond length b_P for the P-block (P=A,B; without loss of generality, we define the conformational asymmetry $\varepsilon \equiv (b_A/b_B)^2 \geq 1$) and $b_{AB} \equiv \sqrt{b_A b_B}$ for the A-B bond. The bonded potential of the k^{th} chain is therefore $\beta u_k^b = \frac{3}{2b_A^2}\sum_{s=1}^{N_A-1}\left(\mathbf{R}_{k,s+1}-\mathbf{R}_{k,s}\right)^2 + \frac{3}{2b_{AB}^2}\left(\mathbf{R}_{k,N_A+1}-\mathbf{R}_{k,N_A}\right)^2 + \frac{3}{2b_B^2}\sum_{s=N_A+1}^{N-1}\left(\mathbf{R}_{k,s+1}-\mathbf{R}_{k,s}\right)^2$,

where $\beta \equiv 1/k_B T$ with k_B being the Boltzmann constant and $\mathbf{R}_{k,s}$ denotes the spatial position of the s^{th} segment on the k^{th} chain. As for the non-bonded interactions, all segments (regardless of their type) repel each other with the pair potential of $u_0(r)/\kappa\rho_0$, where r denotes the distance between two segments, $\beta u_0(r) = \left(15/2\pi r_c^3\right)\left(1 - r/r_c\right)^2$ for $r<r_c$ and 0 otherwise is the normalized DPD potential (*i.e.*, $\int \mathrm{d}\mathbf{r}\beta u_0(r) = 1$; in the limit of the interaction range $r_c \to 0$, $\beta u_0(r)$ becomes the Dirac δ-function), the generalized Helfand compressibility[59] $\kappa \geq 0$ controls the repulsion strength ($\kappa=0$ corresponds to the hard-sphere chains), and $\rho_0 \equiv nN/V$ is the average number density of segments in the system. In addition, an A segment repels a B segment via the pair potential of $u_0(r)\chi/\rho_0$ with the generalized Flory-Huggins parameter $\chi \geq 0$ controlling their repulsion strength.

The $\varepsilon=1$ case of the above model is the same as that used in previous DPD[58, 60-64] and our fast off-lattice Monte Carlo[65-67] simulations of conformationally symmetric A-B melts. In the limit of $N \to \infty$ and $b_{\text{P}} \to 0$ (at fixed $R \equiv \sqrt{N/6}b_{\text{B}}$ and ε), a discrete Gaussian chain becomes a continuous Gaussian chain and our model becomes the same as that used in the field-theoretic simulations of conformationally asymmetric A-B by Fredrickson and co-workers[14], except that they used the Gaussian (instead of DPD) non-bonded potential; as both r_c and κ further approach 0, the DPD model reduces to the "standard" model[44, 45].

With R taken as the unit of length, our DPD model has a total of seven dimensionless parameters: the invariant degree of polymerization $\bar{N} \equiv \left(nR_{e,0}^3/V\right)^2$ with the ideal-chain root-mean-square end-to-end distance $R_{e,0} = \sqrt{\left(N_{\text{A}}-1\right)b_{\text{A}}^2 + b_{\text{AB}}^2 + \left(N_{\text{B}}-1\right)b_{\text{B}}^2}$, f, ε, χN and N/κ are physical parameters (the first three can be quantitatively taken from an experimental system),

and N and b_B/r_c are coarse-graining parameters.

Eqs. (5)~(8) in our previous work[65] give the SCF equations for the above DPD model as

$$\hat{\omega}_A(\mathbf{q}) = \beta\hat{u}_0(q)\left[\chi N\hat{\phi}_B(\mathbf{q}) + (N/\kappa)\left(\hat{\phi}_A(\mathbf{q}) + \hat{\phi}_B(\mathbf{q}) - \delta_{\mathbf{q},\mathbf{0}}\right)\right], \tag{3.1}$$

$$\hat{\omega}_B(\mathbf{q}) = \beta\hat{u}_0(q)\left[\chi N\hat{\phi}_A(\mathbf{q}) + (N/\kappa)\left(\hat{\phi}_A(\mathbf{q}) + \hat{\phi}_B(\mathbf{q}) - \delta_{\mathbf{q},\mathbf{0}}\right)\right], \tag{3.2}$$

$$\phi_A(\mathbf{r}) = \frac{\exp\left(\omega_A(\mathbf{r})/N\right)}{N\hat{q}_N(\mathbf{q}=\mathbf{0})}\sum_{s=1}^{N_A} q_s(\mathbf{r})q^*_{N-s+1}(\mathbf{r}), \tag{3.3}$$

$$\phi_B(\mathbf{r}) = \frac{\exp\left(\omega_B(\mathbf{r})/N\right)}{N\hat{q}_N(\mathbf{q}=\mathbf{0})}\sum_{s=N_A+1}^{N} q_s(\mathbf{r})q^*_{N-s+1}(\mathbf{r}), \tag{3.4}$$

where $\hat{f}(\mathbf{q}) \equiv \int d\mathbf{r}\exp(-i\mathbf{q}\bullet\mathbf{r})f(\mathbf{r})/V$ and $\hat{g}(q) \equiv \int d\mathbf{r}\exp(-i\mathbf{q}\bullet\mathbf{r})g(r)$ denote the 3D Fourier transform of a spatially ***periodic*** function $f(\mathbf{r})$ and a ***radial*** function $g(r)$, respectively, with $\mathbf{q}$ being the wavevector, $r\equiv|\mathbf{r}|$, $q\equiv|\mathbf{q}|$, $\omega_P(\mathbf{r})$ and $\phi_P(\mathbf{r})$ are the conjugate field and volume fraction, respectively, of P segments at spatial position $\mathbf{r}$, and $\delta_{\mathbf{q},\mathbf{0}}$ is the Kronecker δ-function. With $\varepsilon>1$ used here, however, the Chapman-Kolmogorov equations for the propagators $q_s(\mathbf{r})$ and $q^*_{t\equiv N-s+1}(\mathbf{r})$ (*i.e.*, Eqs. (9) and (10) in Ref. 65) become

$$q_{s+1}(\mathbf{r}) = \begin{cases} \exp\left(-\omega_A(\mathbf{r})/N\right)\int d\mathbf{r}'\Phi_A(|\mathbf{r}-\mathbf{r}'|)q_s(\mathbf{r}') & \text{for } s = 1,\ldots,N_A-1 \\ \exp\left(-\omega_B(\mathbf{r})/N\right)\int d\mathbf{r}'\Phi_{AB}(|\mathbf{r}-\mathbf{r}'|)q_s(\mathbf{r}') & \text{for } s = N_A \\ \exp\left(-\omega_B(\mathbf{r})/N\right)\int d\mathbf{r}'\Phi_B(|\mathbf{r}-\mathbf{r}'|)q_s(\mathbf{r}') & \text{for } s = N_A+1,\ldots,N-1 \end{cases} \tag{3.5}$$

with $q_{s=1}(\mathbf{r}) = \exp\left(-\omega_A(\mathbf{r})/N\right)$ and

$$q^*_{t+1}(\mathbf{r}) = \begin{cases} \exp\left(-\omega_B(\mathbf{r})/N\right)\int d\mathbf{r}'\Phi_B(|\mathbf{r}-\mathbf{r}'|)q^*_t(\mathbf{r}') & \text{for } t = 1,\ldots,N_B-1 \\ \exp\left(-\omega_A(\mathbf{r})/N\right)\int d\mathbf{r}'\Phi_{AB}(|\mathbf{r}-\mathbf{r}'|)q^*_t(\mathbf{r}') & \text{for } t = N_B \\ \exp\left(-\omega_A(\mathbf{r})/N\right)\int d\mathbf{r}'\Phi_A(|\mathbf{r}-\mathbf{r}'|)q^*_t(\mathbf{r}') & \text{for } t = N_B+1,\ldots,N-1 \end{cases} \tag{3.6}$$

with $q^*_{t=1}(\mathbf{r}) = \exp\left(-\omega_B(\mathbf{r})/N\right)$, respectively, where $\hat{\Phi}_A(q) = \exp\left(-\varepsilon q^2/N\right)$,

$\hat{\Phi}_{\mathrm{AB}}(q) = \exp\left(-\sqrt{\varepsilon}q^2/N\right)$, and $\hat{\Phi}_{\mathrm{B}}(q) = \exp\left(-q^2/N\right)$. After these SCF equations are solved, the dimensionless mean-field Helmholtz free energy per chain βf_c can be calculated (within a constant) as $\beta f_c = \beta u_c - \sum_{\mathbf{q}}\left(\hat{\omega}_{\mathrm{A}}(\mathbf{q})\hat{\phi}_{\mathrm{A}}(-\mathbf{q}) + \hat{\omega}_{\mathrm{B}}(\mathbf{q})\hat{\phi}_{\mathrm{B}}(-\mathbf{q})\right) - \ln \hat{q}_N(\mathbf{q}=\mathbf{0})$, where the dimensionless internal energy per chain due to the non-bonded interactions is $\beta u_c = \sum_{\mathbf{q}} \beta\hat{u}_0(q)\left[\frac{N}{2\kappa}\left(\hat{\phi}_{\mathrm{A}}(\mathbf{q}) + \hat{\phi}_{\mathrm{B}}(\mathbf{q}) - \delta_{\mathbf{q},\mathbf{0}}\right)\left(\hat{\phi}_{\mathrm{A}}(-\mathbf{q}) + \hat{\phi}_{\mathrm{B}}(-\mathbf{q}) - \delta_{-\mathbf{q},\mathbf{0}}\right) + \chi N\hat{\phi}_{\mathrm{A}}(\mathbf{q})\hat{\phi}_{\mathrm{B}}(-\mathbf{q})\right]$.

In our SCF calculations of the DPD model, Eqs. (3.1) and (3.2), as well as the minimization of βf_c with respect to (up to six) unit-cell parameters $\boldsymbol{\theta}\equiv\{\theta_i\}$, written as $\mathbf{f}(\mathbf{x})=\mathbf{0}$ with the independent variables $\mathbf{x}\equiv\{\hat{\omega}_{\mathrm{A}}(\mathbf{k}), \hat{\omega}_{\mathrm{B}}(\mathbf{k}), \boldsymbol{\theta}\}$, are solved iteratively via the Anderson mixing (AM)[52], which can quickly converge to an accuracy of $|\mathbf{f}|_{\max}<10^{-6}$ or higher.[53] During each iteration, $\phi_{\mathrm{P}}(\mathbf{r})$ and the propagators are calculated in real space with the convolutions in Eqs. (3.5) and (3.6) evaluated via the fast Fourier transforms (FFTs).[65]

We have extended the newly released C++/Cuda version[68] of PSCF[69], an open-source code for SCF calculations of the "standard" model for block copolymer self-assembly, to include our DPD model in order to take advantage of its GPU-accelerated FFTs[70]. PSCF uses a fourth-order pseudo-spectral method[51] to solve the modified diffusion equations (instead of Eqs. (3.5) and (3.6)) satisfied by the propagators in the "standard" model, the composite Simpson's 1/3 rule to evaluate the integrals over s (instead of the summations in Eqs. (3.3) and(3.4)) in the volume fractions of various blocks, and the AM[52] combined with a variable-cell scheme[53] to simultaneously solve the SCF equations and minimize βf_c of an ordered phase with respect to $\boldsymbol{\theta}$; it has been used in some of the SCF calculations[16, 43] mentioned in the main text. To extend PSCF to include our DPD model, we follow Ref. 71 and find the stresses for our DPD model to

be

$$\frac{\mathrm{d}\beta f_c}{\mathrm{d}\theta_i}=\sum_{\mathbf{q}}\frac{\partial q}{\partial\theta_i}\left\{\begin{array}{l}\dfrac{\mathrm{d}\beta\hat{u}_0(q)}{\mathrm{d}q}\left[\dfrac{N}{2\kappa}\left(\hat{\phi}_{\mathrm{A}}(\mathbf{q})+\hat{\phi}_{\mathrm{B}}(\mathbf{q})-\delta_{\mathbf{q},\mathbf{0}}\right)\left(\hat{\phi}_{\mathrm{A}}(-\mathbf{q})+\hat{\phi}_{\mathrm{B}}(-\mathbf{q})-\delta_{-\mathbf{q},\mathbf{0}}\right)+\chi N\hat{\phi}_{\mathrm{A}}(\mathbf{q})\hat{\phi}_{\mathrm{B}}(-\mathbf{q})\right]\\ -\dfrac{1}{\hat{q}_N(\mathbf{q}=\mathbf{0})}\left(\begin{array}{l}\dfrac{\mathrm{d}\hat{\Phi}_{\mathrm{B}}(q)}{\mathrm{d}q}\displaystyle\sum_{t=N_{\mathrm{A}}+1}^{N-1}\hat{q}_t(\mathbf{q})\hat{q}^*_{t+1}(-\mathbf{q})+\dfrac{\mathrm{d}\hat{\Phi}_{\mathrm{AB}}(q)}{\mathrm{d}q}\hat{q}_{N_{\mathrm{A}}}(\mathbf{q})\hat{q}^*_{N_{\mathrm{A}}+1}(-\mathbf{q})\\ +\dfrac{\mathrm{d}\hat{\Phi}_{\mathrm{A}}(q)}{\mathrm{d}q}\displaystyle\sum_{t=1}^{N_{\mathrm{A}}-1}\hat{q}_t(\mathbf{q})\hat{q}^*_{t+1}(-\mathbf{q})\end{array}\right)\end{array}\right\},$$

which are set to 0 to minimize βf_c.

3.2.2 The "standard" model and its SCF calculations

The "standard" model, which is an incompressible system of continuous Gaussian chains with the Dirac δ-function non-bonded potential, has been the most commonly used in SCF calculations of block copolymer self-assembly; we therefore refer the readers to Chapter 2 for its SCF calculations, and just mention here that in the limit of $N\to\infty$, $b_{\mathrm{P}}\to 0$ (at finite $R\equiv\sqrt{N/6}b_{\mathrm{B}}$, ε and b_{B}/r_c) and $\kappa\to 0$, the DPDC model reduces to the "standard" model.

We have also improved the numerical performance of PSCF[69]. In particular, we have implemented the so-called Richardson extrapolated pseudo-spectral (REPS) methods for solving the chain propagators from the modified diffusion equations (MDEs); with R taken as the unit of length, the forward propagator $q(\mathbf{r},s)$, for example, satisfies the MDE $\dfrac{\partial q}{\partial s}=\varepsilon\nabla^2 q-\omega_{\mathrm{A}}(\mathbf{r})q$ for the normalized chain-contour variable $0\le s\le f$ with the initial condition of $q(\mathbf{r},s=0)=1$, which has the formal solution of $q(\mathbf{r},s+\mathrm{d}s)=\exp\left[\left(\varepsilon\nabla^2-\omega_{\mathrm{A}}(\mathbf{r})\right)\mathrm{d}s\right]q(\mathbf{r},s)$. Uniformly discretizing the chain contour into n_s steps each of size $\Delta s=1/n_s$, the 2nd-order pseudo-spectral (PS) method[39] gives $q(\mathbf{r},s+\Delta s)\approx\exp\left(-\omega_{\mathrm{A}}(\mathbf{r})\Delta s/2\right)\exp\left(\Delta s\varepsilon\nabla^2\right)\exp\left(-\omega_{\mathrm{A}}(\mathbf{r})\Delta s/2\right)q(\mathbf{r},s)$, which has a ***global*** error of $O(\Delta s^2)$. Morse and co-workers first pointed out that the error of the PS method contains

only even powers of Δs and thus proposed a 4th-order method, which is used in PSCF[69], by linearly extrapolating the two results of $q(\mathbf{r},s+\Delta s)$ obtained via the PS method with the step-size of Δs and $\Delta s/2$, respectively, to the limit of $\Delta s \to 0$.[49] This is similar to the (composite) trapezoidal rule for numerical integration, whose error also contains only even powers of the step-size; the Kth-order polynomial extrapolation of the $K+1$ results obtained via the trapezoidal rule with successively halved step-size to the limit of zero step-size then give the commonly used Romberg integration, with $K=1$ corresponding to the (composite) Simpson's 1/3 rule. We therefore refer to the PS method and that proposed by Morse and co-workers[49] as the REPS-0 and REPS-1 method, respectively, and have implemented the REPS-K methods for $K=0,\ldots,4$. Note that the REPS-K method has a global error of $O(\Delta s^{2(K+1)})$; this requires Romberg integration of the same (or higher) order to calculate $\phi_{\mathrm{A}}(\mathbf{r}) = \int_0^f \mathrm{d}s\, q(\mathbf{r},s)q^{\dagger}(\mathbf{r},s) \Big/ \hat{q}(\mathbf{q}=\mathbf{0}, s=1)$ with $q^{\dagger}(\mathbf{r},s)$ denoting the backward propagator and $\hat{q}(\mathbf{q},s) \equiv \int \mathrm{d}\mathbf{r} \exp(-i\mathbf{q}\bullet\mathbf{r}) q(\mathbf{r},s) \Big/ V$ (for example, the Simpson's 1/3 rule is used in PSCF[47] to match the REPS-1 method), which in turn requires $n_s f$ (as well as $n_s(1-f)$) be an integer multiple of 2^K.

3.3 Results and Discussion

3.3.1 Unit-cell discretization and accuracy of βf_c

SCF equations, including those for the minimization of the dimensionless (mean-field) Helmholtz free energy per chain βf_c with respect to the (up to six) unit-cell parameters $\boldsymbol{\theta}$, are written as $\mathbf{f}(\mathbf{x})=\mathbf{0}$ and solved via the Anderson mixing (AM) to an accuracy of $|\mathbf{f}|_{\max}<\varepsilon_0$. For the DPDC model, we set $\varepsilon_0=10^{-10}$. Fig. 3.1 shows how the accuracy of βf_c for this model, denoted by $\Delta(m) \equiv |\beta f_c(m) - \beta f_c(m=128)|$ with m being the spatial discretization parameter, varies with m for all the eight ordered phases considered in this work, including the regular-hexagonally packed

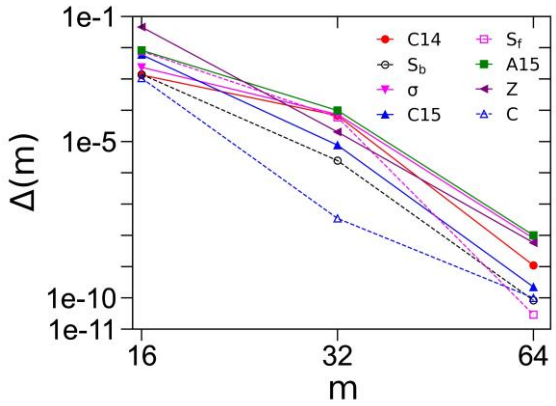

Figure 3.1. Logarithmic plot of the accuracy in the dimensionless (mean-field) Helmholtz free energy per chain βf_c of all the eight ordered phases considered in this work at χN=40 for the DPDC model. The periodic unit cell of C, C14, σ and all other phases (*i.e.*, S_b/S_f/A15/C15/Z) is uniformly discretized into m^2, $m\times m\times 2m$, $2m\times 2m\times m$ and m^3 grid points, respectively. Note that the same unit-cell size, chosen to be very close to that in bulk (*i.e.*, minimizing βf_c of the corresponding phase), is used for various m. f=0.3 for C14/C15 and 0.2 for others; ε=2.25 for Z and 4 for others; and N=10, $N/\kappa=50\pi$ and $b_B/r_c=\sqrt{3}/2$ in all the cases. See the main text for more details.

cylinders (C), body-centered cubic spheres (S_b), face-centered cubic spheres (S_f), and five FK phases (*i.e.*, σ, A15, C14, C15 and Z). Based on Fig. 3.1, we choose m=64 in our subsequent SCF calculations of the DPDC model, which gives $\Delta<10^{-8}$ (and even smaller Δ for lower χN) in all the cases.

For the "standard" model, we set $\varepsilon_0=10^{-6}$. Fig. 3.2 shows how the accuracy of βf_c for this model, denoted by $\Delta(m,n_s,K=4)\equiv|\beta f_c(m,n_s,K=4)-\beta f_c(m=128,n_s=512,K=4)|$, varies with m and the chain-contour discretization parameter n_s for various ordered phases, where we use the REPS-4 method to solve the MDEs. We see that in most cases Δ decreases with increasing n_s as expected; that Δ levels off with increasing n_s at small m=32 for σ, A15, Z and S_f indicates that the error caused by the real-space discretization dominates Δ in these cases. Furthermore, that the Δ-curves for m=64 and 128 nearly overlap in all the cases indicates that m=64 gives sufficient real-

space discretization for all the ordered phases, the error of which is smaller than that caused by

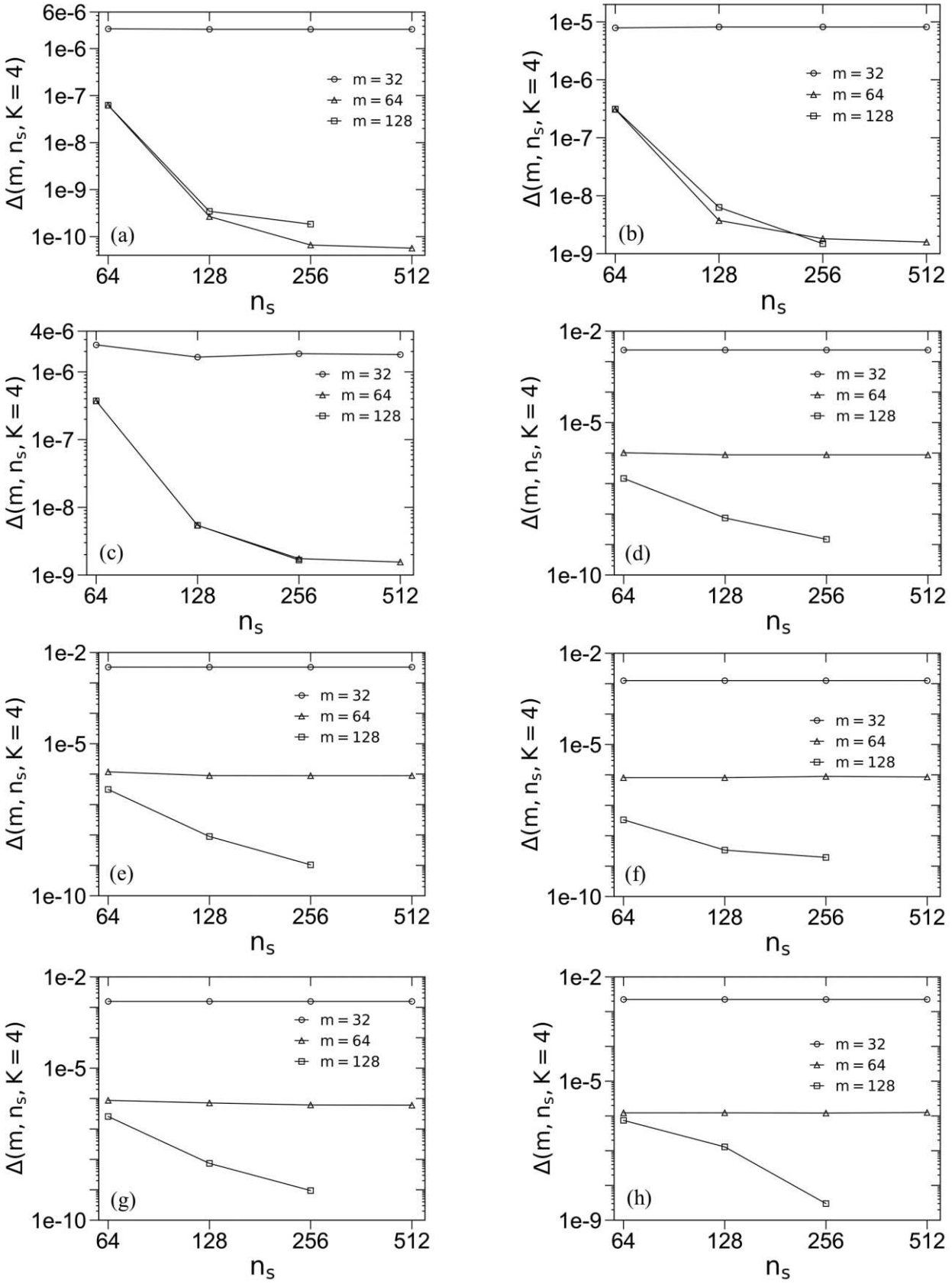

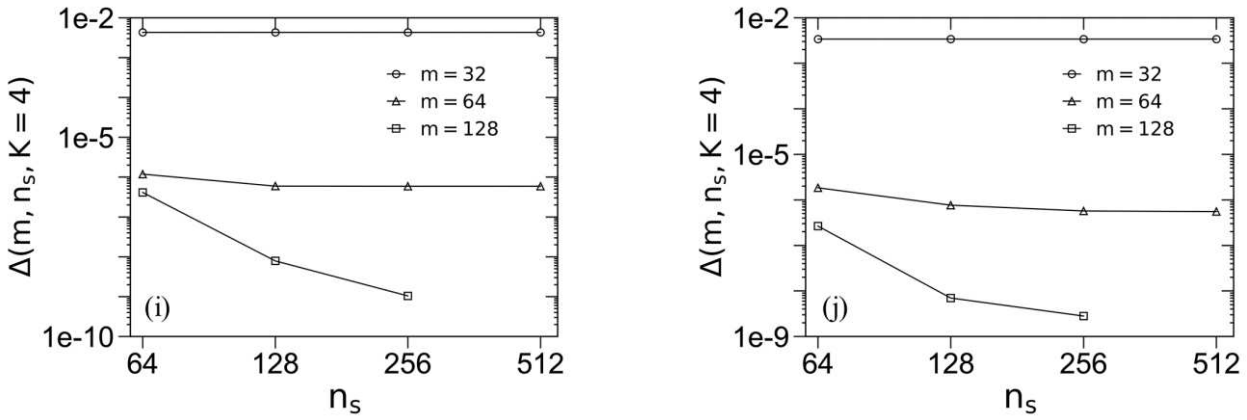

Figure 3.2. Logarithmic plot of the accuracy in the dimensionless (mean-field) Helmholtz free energy per chain βf_c, $\Delta(m,n_s,K=4) \equiv |\beta f_c(m,n_s,K=4) - \beta f_c(m=128,n_s=512,K=4)|$, of (a) C, (b) S_b, (c) S_f, (d) σ, (e) A15, (f) C14, (g) C15, (h) H, (i) Z and (j) pσ formed by neat DBC melts at f=1/4 and χN=40, where ε=2.25 for σ/H/pσ and 4 for other phases. The unit cell of C, S_b/S_f/A15/C15/Z, σ/C14, pσ and H is uniformly discretized into m^2, m^3, $m\times m\times 2m$, $2m\times 1.6875m\times m$ and $m\times m\times 4m$ grid points, respectively, and the copolymer chain contour is uniformly discretized into n_s subintervals. The REPS-4 method is used to solve the modified diffusion equations. See the main text for more details. This figure shows that at χN=40, while m=32 can be used for the non-FK phases (*i.e.*, C/S_b/S_f) to give $\Delta<10^{-5}$, m=64 is needed for the FK phases (*i.e.*, A15/C14/C15/Z/σ/H/pσ).

the chain-contour discretization (at the largest χN-value of 40 used in this work). We therefore also choose m=64 in our subsequent SCF calculations of the "standard" model.

Fig. 3.3 shows how $\Delta(m=64,n_s,K) \equiv |\beta f_c(m=64,n_s,K) - \beta f_c(m=128,n_s=512,K=4)|$ for various ordered phases varies with n_s and K, where we use the REPS-K methods to solve the MDEs; note that, since the REPS-K method requires $n_K \equiv 2^{K+1}-1$ pairs of fast Fourier transforms to obtain the propagators in each step along the chain contour (with the step size of $1/n_s$), we use $n_K n_s$ as the horizontal axis in Fig. 3.3 in order to compare the efficiency of various REPS-K methods. We see that in all cases Δ decreases with increasing n_s as expected, and that the REPS-K methods with$K$=3 and 4 are less efficient than those with K=1 and 2 (at least for the system parameters used in Fig. 3.3), although the larger the K-value, the smaller the n_s-value (thus the less the GPU memory) required to achieve a certain Δ. Based on Fig. 3.3, we choose K=2 with n_s=256 (at

f=0.25), which gives $\Delta<10^{-5}$ (at the largest χN-value of 40 used in this work), in our SCF

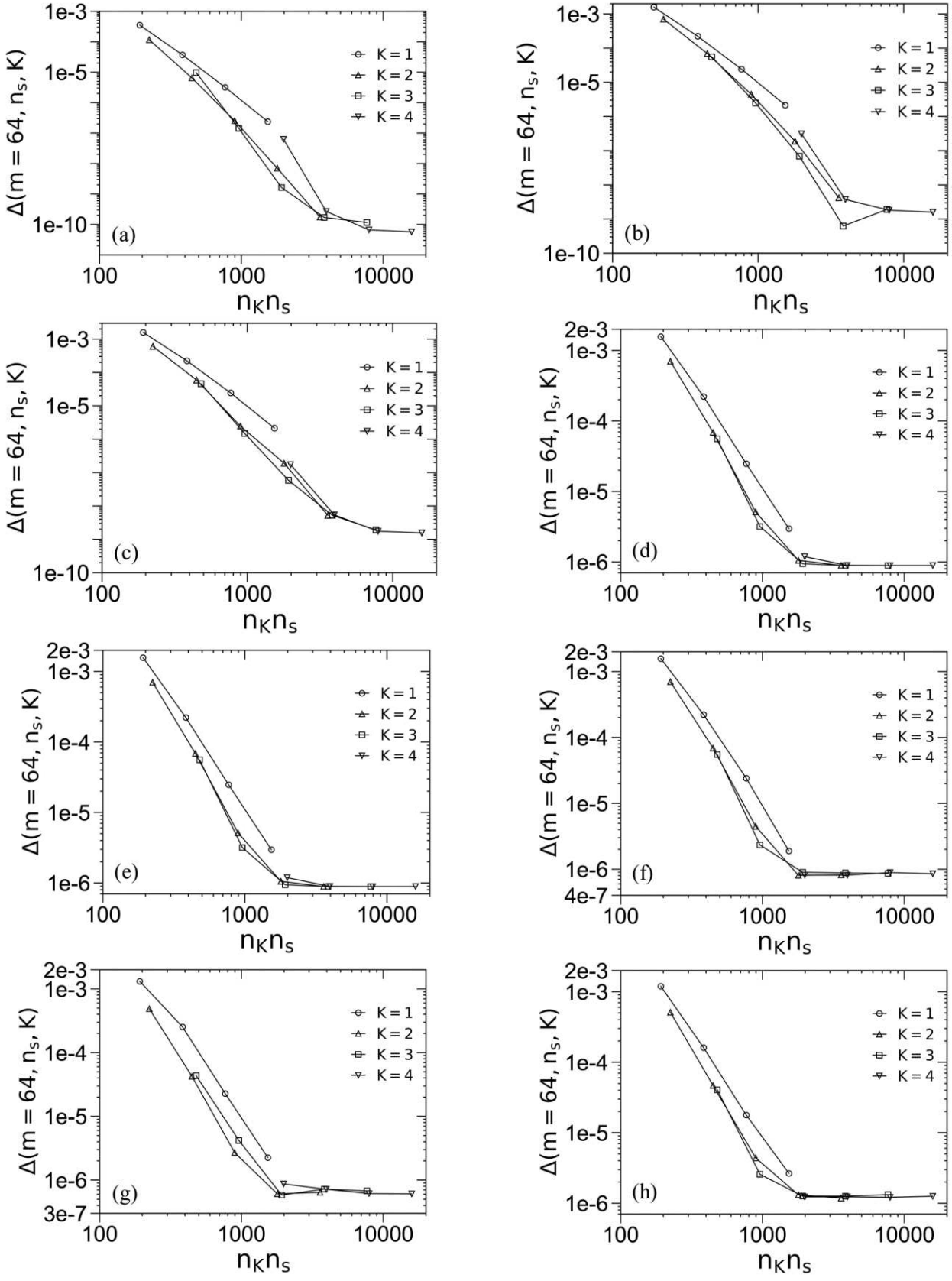

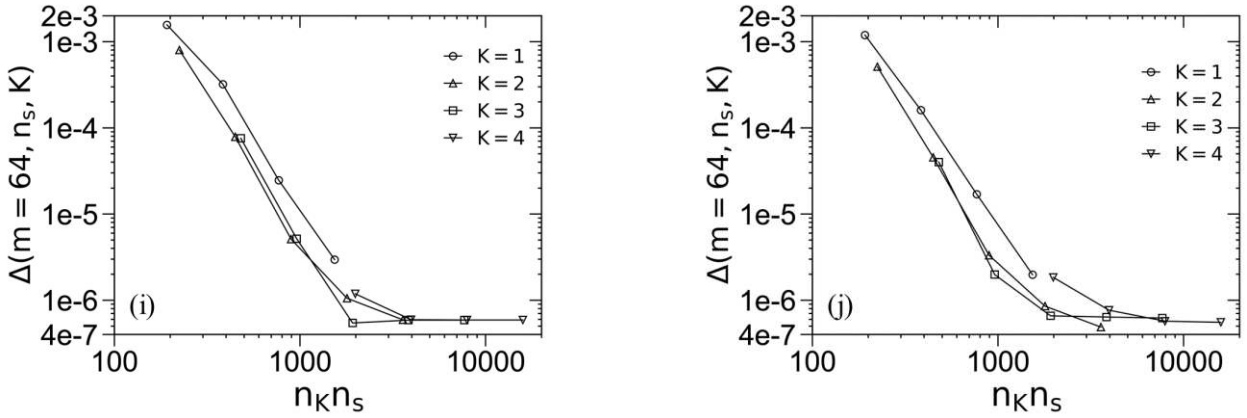

Figure 3.3. Similar to Fig. S1 except that $\Delta(m=64,n_s,K) \equiv |\beta f_c(m=64,n_s,K)-\beta f_c(m=128,n_s=512,K=4)|$, $n_K=2^{K+1}-1$, and the REPS-K method is used to solve the MDEs. See the main text for more details. This figure shows that at χN=40, n_s=64 (with K=3 or 4) or 128 (with K=2) or 512 (with K=1) is needed to give $\Delta<10^{-5}$. In addition, the REPS-3 and REPS-2 methods have comparable efficiency (measured by the number of fast Fourier transforms needed to solve the modified diffusion equations), which is higher than that of REPS-1 and REPS-4.

calculations of the "standard" model; in comparison, n_s=512 is needed for REPS-1 to reach this βf_c-accuracy. Note that, since each block must be uniformly discretized into an integer multiple of 2^K subintervals in the REPS-K method, for f=0.2 and 0.3 studied below we use slightly larger n_s-values of 260 and 280, respectively, in our subsequent SCF calculations.

Comparing Fig. 3.1 with Figs. 3.2 and 3.3, we see that SCF calculations of the DPDC model can achieve much higher βf_c-accuracy than those of the "standard" model, due to the model differences. In particular, as pointed out in our recent paper[76], N in the DPDC model is much smaller than n_s (=100~1000) typically needed to achieve good βf_c-accuracy for the "standard" model; SCF calculations of the DPDC model therefore are faster and use less memory, both by at least one order of magnitude, than the latter. In addition, βf_c of an ordered phase in the DPDC model depends only on the spatial discretization, making its accuracy much easier to study than in the "standard" model.

3.3.2 Phase diagrams

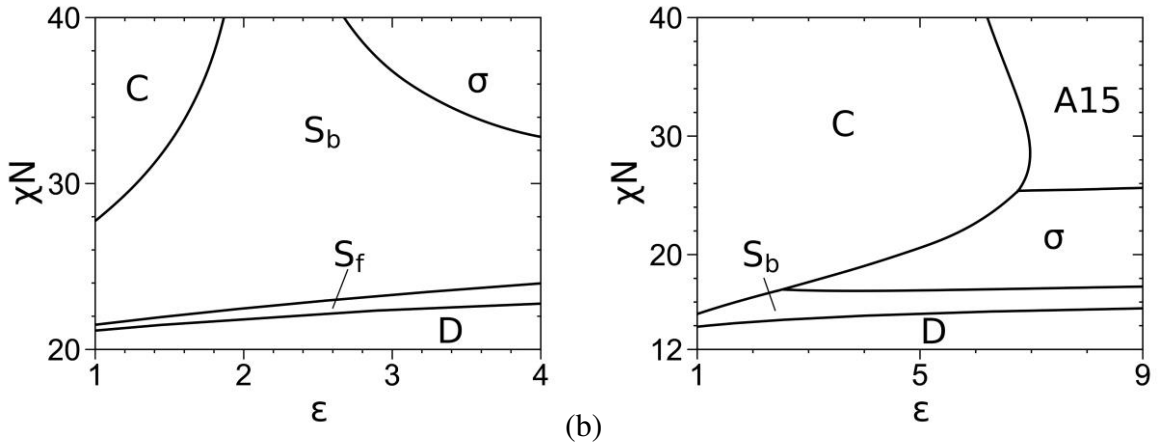

Figure 3.4. Phase diagrams of the "standard" model at (a) f=0.2 and (b) f=0.3, where D denotes the disordered phase. The periodic unit cell of C, σ and all other ordered phases (*i.e.*, A15/Z/S_b/S_f) is uniformly discretized into 64^2, 128×128×64 and 64^3 grid points, respectively, and the chain contour is uniformly discretized into (a) 260 and (b) 280 subintervals. The REPS-2 method is used to solve the MDEs, and the phase boundaries are solved to an accuracy of 10^{-3} in χN. The triple points are at (ε,χN)=(2.434,16.944) and (6.752,25.320) in (b). See the main text for more details.

Table 3.1. Comparison of various phase boundaries obtained in this work and by Fredrickson and co-workers[1].

	This work	**Ref. 1**
f=0.2 and χN=40		
C/S_b	ε=1.874	ε=1.882
S_b/σ	ε=2.667	ε=2.722
f=0.2 and ε=9		
D/S_f	χN=24.225	χN=24.155
S_f/S_b	χN=26.261	χN=26.177
S_b/σ	χN=30.746	χN=30.483
f=0.3 and χN=40		
C/A15	ε=6.210	ε=6.249
f=0.3 and ε=9		
S_b/σ	χN=17.303	χN=17.257
σ/A15	χN=25.629	χN=25.629

Fig. 3.4 shows our SCF phase diagrams for the "standard" model in the χN-ε plane at

f=0.2 and 0.3, where the phase boundaries are solved via the Ridder's method to an accuracy of 10^{-3} in χN by equating βf_c of the two phases having the smallest βf_c at given ε and the obtained χN. Table 3.1 in Supporting Information quantitatively compares eight of our phase boundary points with those obtained by Fredrickson and co-workers[14]; note that their phase diagrams are in the χN-f plane at ε=9 and in the ε-f plane at χN=40. Our phase boundary points are in good agreement with theirs, with the largest relative deviation being about 2%. Since they considered

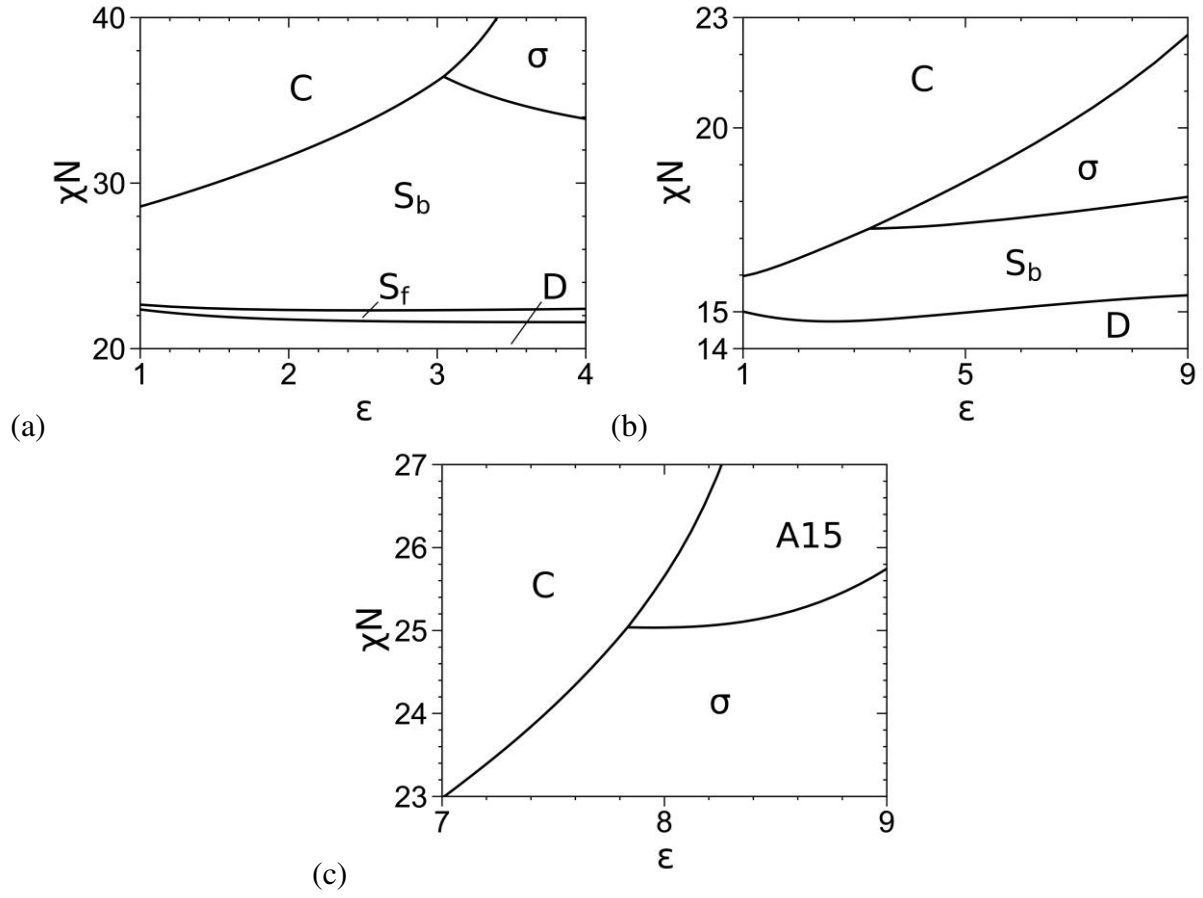

Figure 3.5. Phase diagrams of the DPDC model at (a) f=0.2 and N=10, (b) f=0.3 and N=10, and (c) f=0.3 and N=20, where D denotes the disordered phase. The periodic unit cell of C, C14, σ and all other ordered phases (*i.e.*, S_b/S_f/A15/C15/Z) is uniformly discretized into 64^2, 64×64×128, 128×128×64 and 64^3 grid points, respectively. The phase boundaries are solved to an accuracy of 10^{-3} in χN. The triple point is at (ε,χN)=(3.045,36.428) in (a), (3.290,17.263) in (b), and (7.840,25.039) in (c). N/κ=50π and $b_B/r_c = \sqrt{3}/2$ in all the cases. See the main text for more details.

but did not find C14 and C15 to be stable in their phase diagrams[1], we do not include these phases in our SCF calculations of the "standard" model. On the other hand, we have included but not found the Z phase to be stable. From Fig. 3.4(a), we see that at f=0.2 increasing χN expands the stable region in ε of σ into that of S_b, consistent with the phase diagrams for the "standard" model at χN=0[14] obtained by Fredrickson and co-workers. From Fig. 3.4(b), we see that at f=0.3 increasing χN<28.580 expands the stable region in ε of C into those of σ and A15, but increasing χN>28.580 expands the stable region in ε of A15 into that of C; the latter is also consistent with the phase diagrams at χN=40[14] obtained by Fredrickson and co-workers.

Fig. 3.5 shows our SCF phase diagrams for the DPDC model in the χN-ε plane at f=0.2 (with N=10) and 0.3 (with N=10 and 20), where the phase boundaries are again solved via the Ridder's method[119] to an accuracy of 10^{-3} in χN by equating βf_c of the two phases having the smallest βf_c at given ε and the obtained χN; as mentioned in Ref. 76, for the nearly incompressible melts studied here, our previous work for conformationally symmetric A-B shows negligible differences between the SCF phase boundaries determined by equating βf_c, where the two phases have the same density, and those by equating the chain chemical potential and pressure, where the two phases have different densities and the two-phase coexisting region could appear.[120] Note that our phase boundaries at ε=1 and N=10 are the same as those reported in Table IV of Ref. [104] (where S_f was not considered), indicating that the less accurate βf_c calculated in our previous work is still good enough for the classical phases (*i.e.*, C and S_b) formed by conformationally symmetric DBCs. For ε>1 and N=10, however, our phase diagrams are qualitatively different from those reported in our previous work[76]; in particular the phase boundary between S_b and S_f and that between S_f and the disordered phase (D) at f=0.2 are also

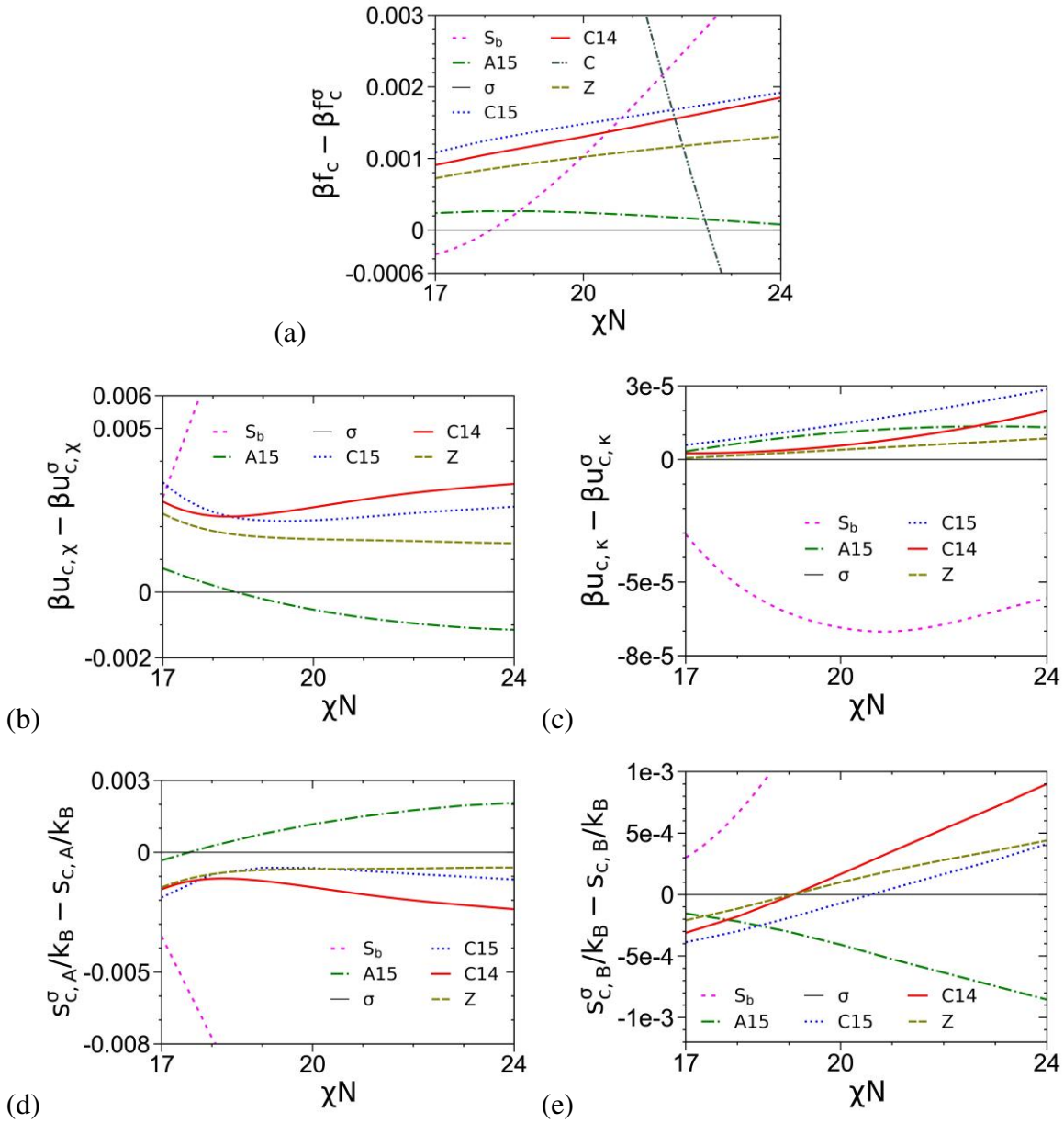

Figure 3.6. Comparisons of (a) the dimensionless (mean-field) Helmholtz free energy per chain βf_c, (b) the dimensionless internal energy per chain due to the A-B repulsion $\beta u_{c,\chi}$ and (c) that due to the system compressibility $\beta u_{c,\kappa}$, and (d) the dimensionless entropy per chain of the A block $s_{c,A}/k_B$ and (e) that of the B block $s_{c,B}/k_B$, of various ordered phases obtained from our SCF calculations of the DPDC model at f=0.3, N=10 and ε=9, with the σ phase taken as a reference. Due to its too large βf_c, the S_f phase is not shown here. Similarly, since for χN=17~24 $\beta u_{c,\chi}^{C} - \beta u_{c,\chi}^{\sigma} = -0.034 \sim -0.044$, $\beta u_{c,\kappa}^{C} - \beta u_{c,\kappa}^{\sigma} = 0.0014 \sim 0.0025$, $s_{c,A}^{\sigma}/k_B - s_{c,A}^{C}/k_B = 0.09 \sim 0.14$ and $s_{c,B}^{\sigma}/k_B - s_{c,B}^{C}/k_B = -0.042 \sim -0.099$, the C phase is not shown in (b)~(e). N/κ=50π and $b_B/r_c = \sqrt{3}/2$. See the main text for more details.

altered. On the other hand, our previous results[76] that all phase boundaries are shifted to smaller

χN as f increases from 0.2 to 0.3 and that a small region of S_f exists at f=0.2 but disappears at f=0.3 are still valid. Finally, at N=20 A15 emerges as another stable FK phase at f=0.3.

Comparing Figs. 3.4 and 3.5, we see that at f=0.2 the SCF phase diagram for the DPDC model at N=10 is qualitatively the same as that for the "standard" model, but they are qualitatively different at f=0.3 (where A15 is not stable for the DPDC model); the latter and any quantitative differences in the SCF phase diagrams are solely due to the differences between these two models. Changing the "standard" model to the DPDC model expands the stable regions of C and S_b into that of σ at both f-values, and the stable region of C into that of A15 at f=0.3. On the other hand, that A15 becomes stable for the DPDC model at f=0.3 as N increases to 20 is consistent with the fact that the DPDC model reduces to the "standard" model in the limit of $N\rightarrow\infty$, $b_P\rightarrow 0$ (at finite R, ε and b_B/r_c) and $\kappa\rightarrow 0$.

3.3.3 Curves βf_c and its components

As an example, Fig. 3.6(a) compares βf_c of various ordered phases obtained from our SCF calculations of the DPDC model at f=0.3 and ε=9; we see that S_b is stable for χN<18.126, σ is stable for 18.126<χN<22.529, and C is stable at larger χN. Figs. 3.6(b)~3.6(e) compare the various components of βf_c, including the dimensionless internal energy per chain $\beta u_{c,\chi}$ due to the A-B repulsion, the dimensionless internal energy per chain $\beta u_{c,\kappa}$ due to the system compressibility, and the dimensionless entropy per chain $s_{c,P}/k_B$ of the P block for various ordered phases. We see that the stability of σ at intermediate χN is due to its delicate balance between $\beta u_c=\beta u_{c,\chi}+\beta u_{c,\kappa}$ and $s_c/k_B=s_{c,A}/k_B+s_{c,B}/k_B$, and that of C at larger χN is mainly due to its smallest $\beta u_{c,\chi}$ (βu_c) and $-s_{c,B}/k_B$; in contrast, S_b at smaller χN is mainly stabilized by its smallest $-s_{c,A}/k_B$ ($-s_c/k_B$). In addition, our results show that $\beta u_{c,\kappa}$ accounts for only 0.3~0.5% of βu_c, thus

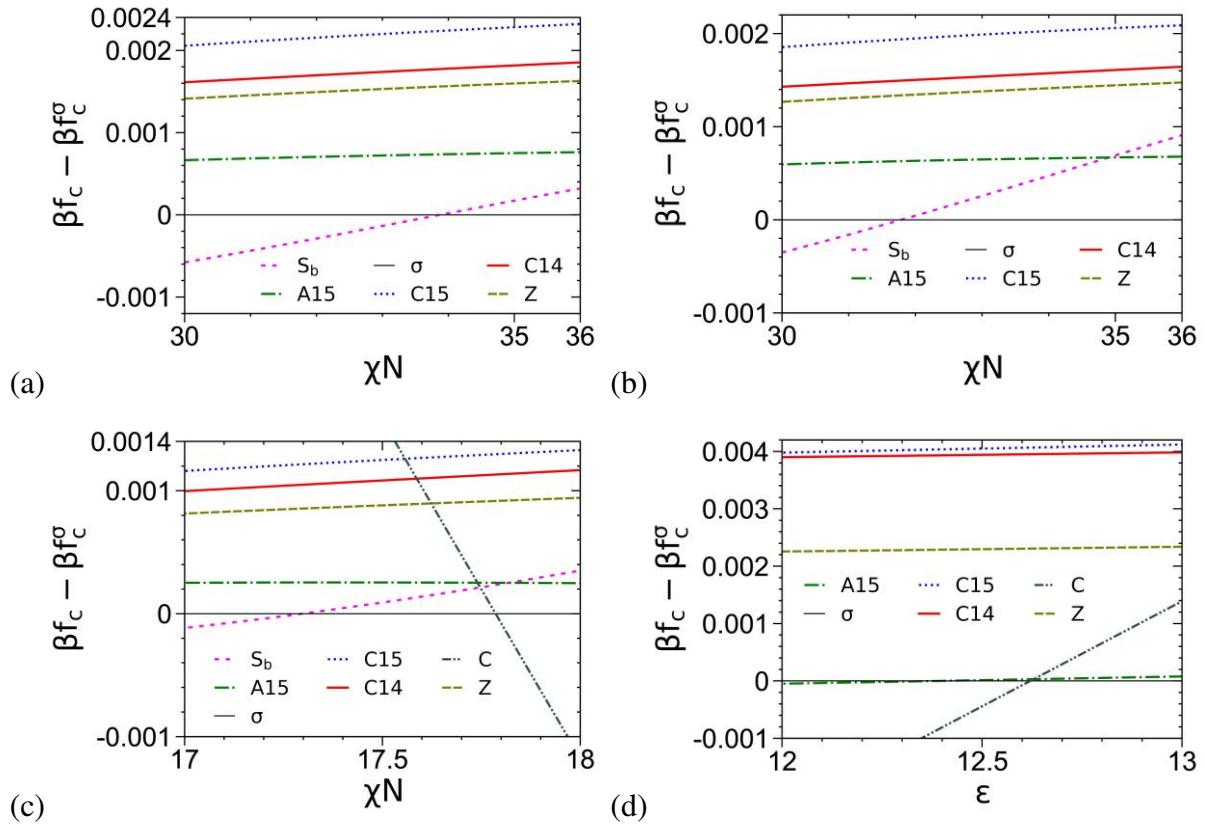

Figure 3.7. Comparisons of the dimensionless (mean-field) Helmholtz free energy per chain βf_c of various ordered phases obtained from our SCF calculations of the DPDC model, with the σ phase taken as a reference. Due to their too large βf_c, the S_f phase is also not shown here, the C phase is not shown in parts (a) and (b), and the S_b phase is not shown in part (d). f=0.2 and ε=4 in (a), f=0.2 and ε=9 in (b), f=0.3 and ε=4 in (c), f=0.3 and χN=40 in (d), N=10, N/κ=50π, and $b_B/r_c = \sqrt{3}/2$. See the main text for more details.

indicating that our DPDC model at N/κ=50π is nearly incompressible. Similar results are found for other parameter values as shown in Figs. 3.7~3.9; we see that within our parameter range, βf_c of the FK phases increase in the order of σ/A15, Z, C14 and C15 with their differences being on the order of 10^{-3} or smaller. Fig. 3.7 compares $\beta u_{c,\chi}$ of various FK phases obtained from our SCF calculations of the DPDC model; combining it with Figs. 3.6(b), 3.8(b) and 3.9(b), we see that σ and A15 always have smaller $\beta u_{c,\chi}$ than Z, C14 and C15, which explains why the latter three FK phases are not stable in our SCF calculations.

Note that at finite R, ε and b_B/r_c, as $N\to\infty$ (thus $b_P\to 0$ and $r_c\to 0$) our (compressible)

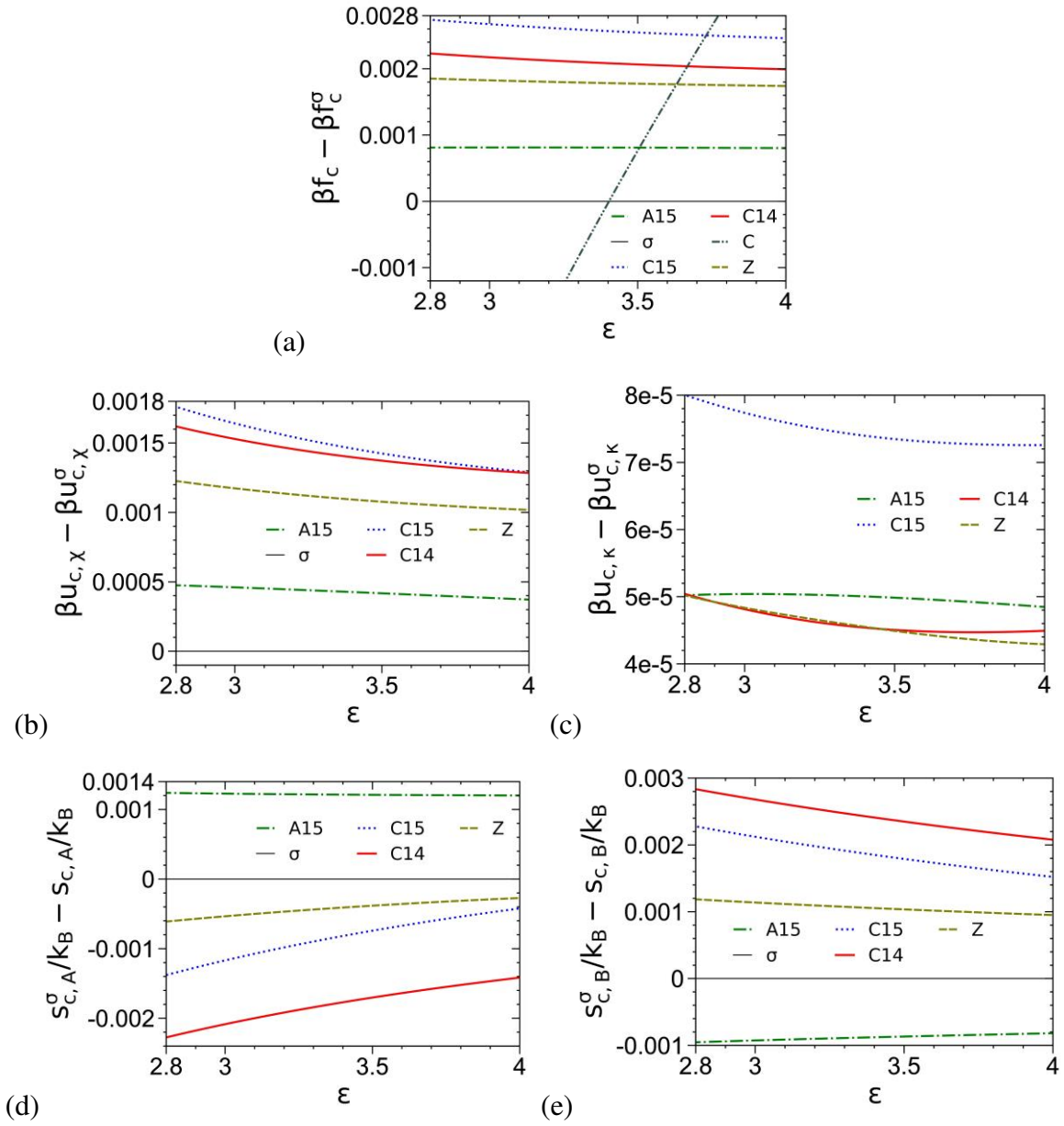

Figure 3.8. Comparisons of (a) the dimensionless (mean-field) Helmholtz free energy per chain βf_c, (b) the dimensionless internal energy per chain due to the A-B repulsion $\beta u_{c,\chi}$ and (c) that due to the system compressibility $\beta u_{c,\kappa}$, and (d) the dimensionless entropy per chain of the A block $s_{c,A}/k_B$ and (e) that of the B block $s_{c,B}/k_B$, of various ordered phases obtained from our SCF calculations of the DPDC model at f=0.2, N=10 and χN=40, with the σ phase taken as a reference. Due to their too large βf_c, the S_b and S_f phases are not shown here. Similarly, since for ε=2.8~4 $\beta u_{c,\chi}^{C} - \beta u_{c,\chi}^{\sigma} = -0.030 \sim -0.019$, $\beta u_{c,\kappa}^{C} - \beta u_{c,\kappa}^{\sigma} = 0.0076 \sim 0.0081$, $s_{c,A}^{\sigma}/k_B - s_{c,A}^{C}/k_B = 0.177 \sim 0.171$ and $s_{c,B}^{\sigma}/k_B - s_{c,B}^{C}/k_B = -0.160 \sim -0.156$, the C phase is not shown in (b)~(e). N/κ=50π and $b_B/r_c = \sqrt{3}/2$. See the main text for more details.

DPDC model becomes the Edwards model (*i.e.*, a compressible diblock copolymer melt, or

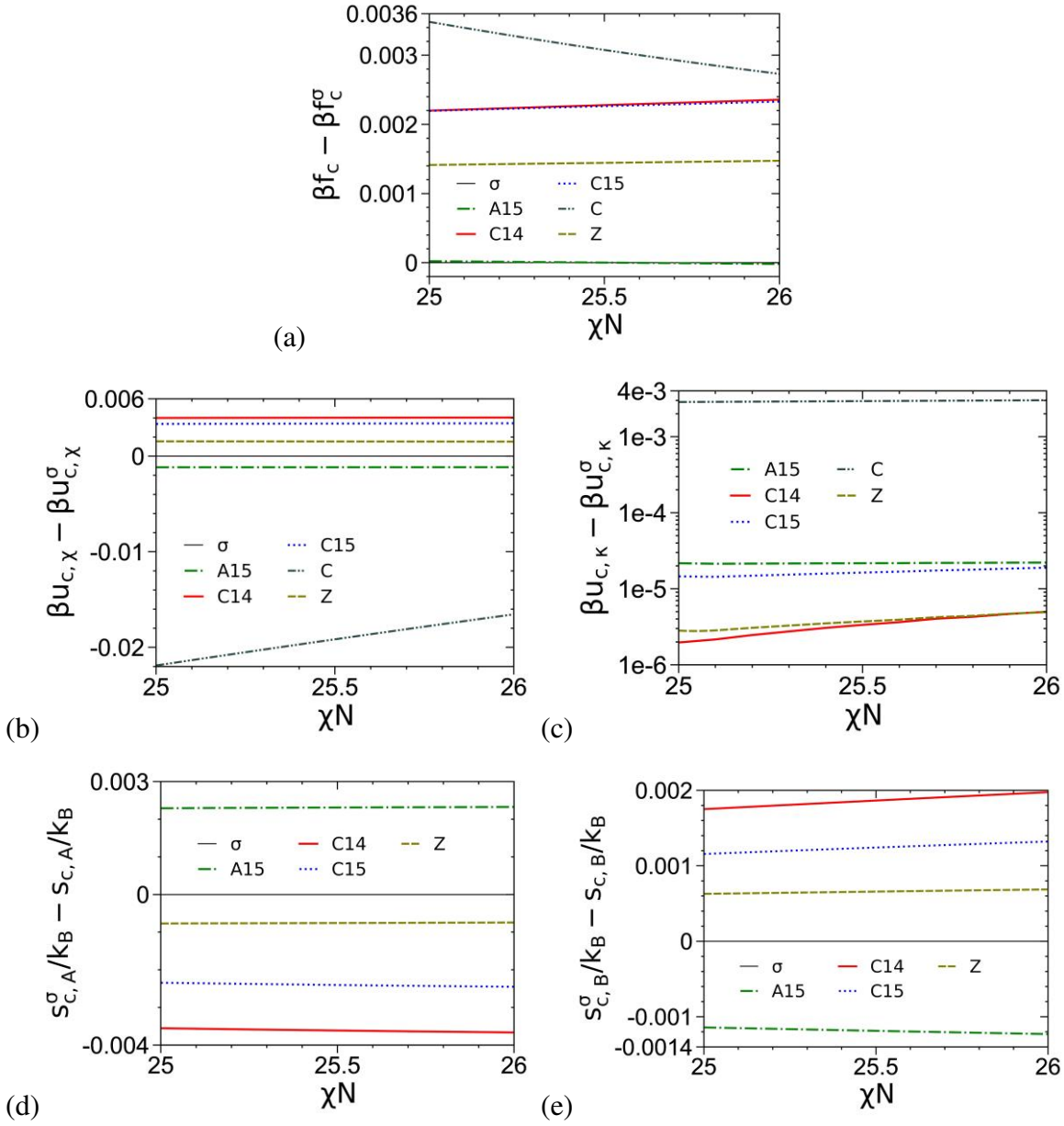

Figure 3.9. Comparisons of (a) the dimensionless (mean-field) Helmholtz free energy per chain βf_c, (b) the dimensionless internal energy per chain due to the A-B repulsion $\beta u_{c,\chi}$ and (c) that due to the system compressibility $\beta u_{c,\kappa}$, and (d) the dimensionless entropy per chain of the A block $s_{c,A}/k_B$ and (e) that of the B block $s_{c,B}/k_B$, of various ordered phases obtained from our SCF calculations of the DPDC model at f=0.3, N=20 and ε=9, with the σ phase taken as a reference. Due to their too large βf_c, the S_b and S_f phases are not shown here. Similarly, since for χN=17~24 $s_{c,A}^\sigma/k_B - s_{c,A}^C/k_B = 0.1322 \sim 0.1316$ and $s_{c,B}^\sigma/k_B - s_{c,B}^C/k_B = -0.110 \sim -0.115$, the C phase is not shown in (d) and (e). $N/\kappa = 50\pi$ and $b_B/r_c = \sqrt{3}/2$. See the main text for more details.

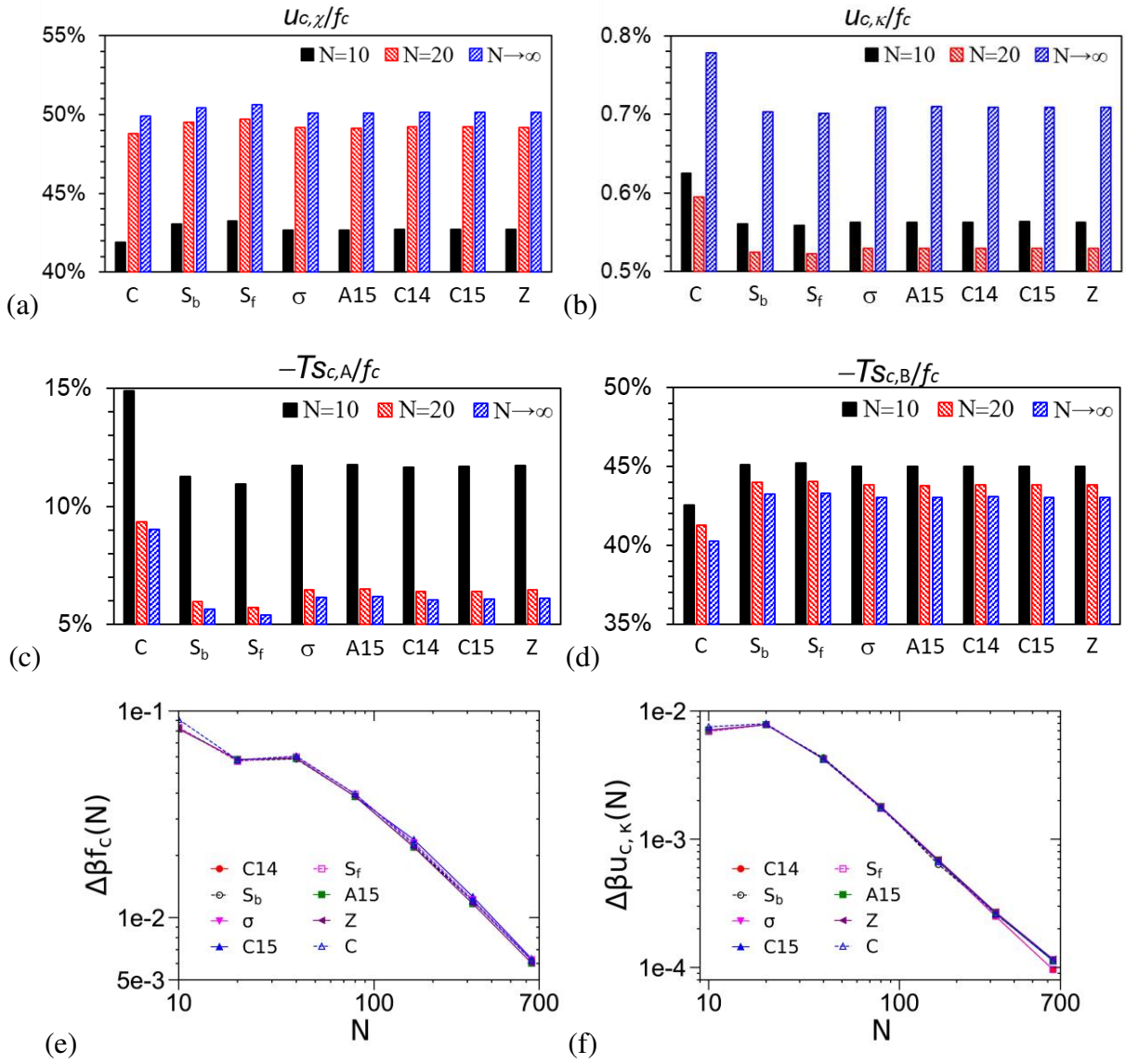

Figure 3.10. Variations of (a) the percentage of the dimensionless internal energy per chain due to the A-B repulsion $\beta u_{c,\chi}$ in the dimensionless Helmholtz free energy per chain βf_c, (b) that of the dimensionless internal energy per chain due to the system compressibility $\beta u_{c,\kappa}$ in βf_c, (c) that of the dimensionless entropy per chain of the A block $s_{c,A}/k_B$ in βf_c, (d) that of the dimensionless entropy per chain of the B block $s_{c,B}/k_B$ in βf_c, (e) βf_c, and (f) $\beta u_{c,\kappa}$ *vs.* the chain length N of various ordered phases obtained from our SCF calculations of the DPDC model, where $\Delta\beta f_c(N)\equiv|\beta f_c(N)-\beta f_c(N\to\infty)|$ and $\Delta\beta u_{c,\kappa}(N)\equiv|\beta u_{c,\kappa}(N)-\beta u_{c,\kappa}(N\to\infty)|$, respectively, and $N\to\infty$ corresponds to the Edwards model. f=0.3, ε=9, χN=26, N/κ=50π, and $b_B/r_c=\sqrt{3}/2$. See the main text for more details.

equivalently solution in an implicit good solvent, of continuous Gaussian chains with the Dirac δ-function non-bonded potential). Fig. 3.10 shows that for all the ordered phases considered in

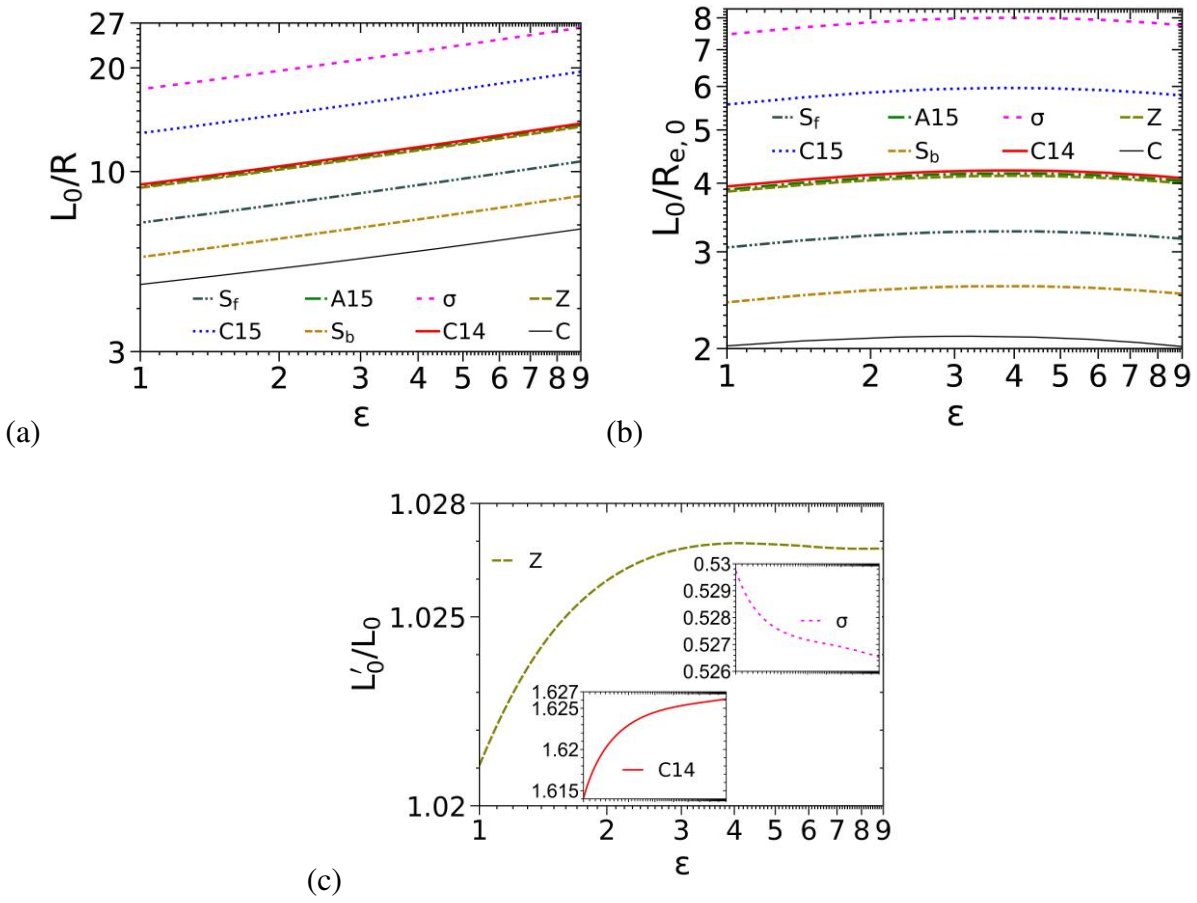

Figure 3.11. Logarithmic plots of the bulk period L_0 (taken as the length of at least two equal sides of the unit cell) in units of (a) $R \equiv \sqrt{N/6}b_B$ and (b) the ideal-chain root-mean-square end-to-end distance $R_{e,0} = \sqrt{\left(1+(\varepsilon-1)f\right)N - \varepsilon + \sqrt{\varepsilon} - 1}b_B$ of various ordered phases obtained from our SCF calculations of the DPD model. Part (c) shows the semi-logarithmic plot of the unit-cell aspect ratio, where both insets have the same axes as the main plot except for the range of the vertical axis. f=0.2, χN=40, N=10, N/κ=50π, and $b_B/r_c = \sqrt{3}/2$. See main text for more details.

this work, $u_{c,\chi}/f_c$, $-Ts_{c,A}/f_c$ and $-Ts_{c,B}/f_c$, as well as $\beta u_{c,\kappa}$ and βf_c for N>30, of the DPDC model approach their corresponding value of the Edwards model monotonically as N increases. In addition, as N increases from 10 to 20, $u_{c,\chi}/f_c$ (and $-Ts_{c,A}/f_c$) exhibits the largest change. Fig. 3.10(a) shows that $u_{c,\chi}/f_c$ increases as N increases for all the ordered phases considered here; in particular, we note that at f=0.3, ε=9 and χN=26 shown in the figure, C is the stable phase at

N=10 while σ becomes more stable than C at N=20 (note that at both N-values, A15 is slightly more stable than σ with a ~10^{-5} lower βf_c). Given the small changes of βf_c of these phases shown in Fig. 3.10(e) as N increases from 10 to 20, our finding that $\beta u_{c,\chi}$ increases as σ becomes more stable than C is consistent with that of Collanton and Dorfman[77], who recently found that $\beta u_{c,\chi}$ increases as the stable phase changes from C to σ while f decreases in their SCF calculations of the "standard" model. Furthermore, while the values of the thermodynamic quantities shown in Fig. 5 vary with the system parameters, Fig. 3.10(b) again shows that our DPDC model at N/κ=50π is nearly incompressible.

Finally, Fig. 3.11 shows how the bulk period and unit-cell aspect ratio of the ordered phases studied here vary with ε, and Fig. 3.12 shows in 2D the normalized volume fraction profiles of A segments $\tilde{\phi}_{\mathrm{A}}(\mathbf{r}) \equiv \phi_{\mathrm{A}}(\mathbf{r})/\phi(\mathbf{r})$ and the total volume fraction profiles $\phi(\mathbf{r}) \equiv \phi_{\mathrm{A}}(\mathbf{r}) + \phi_{\mathrm{B}}(\mathbf{r})$ of the various FK phases formed by our DPDC model.

3.4 Summary

To summarize, we have performed a numerical issue in our SCF calculations and calculated the SCF phase diagrams for the dissipative particle dynamics chain (DPDC) model (*i.e.*, compressible melts of discrete Gaussian chains with the DPD non-bonded potential) of conformationally asymmetric diblock copolymers A-B proposed in our recent paper[76] in the χN-ε plane, where χN and $\varepsilon \equiv (b_{\mathrm{A}}/b_{\mathrm{B}})^2 \geq 1$ characterize, respectively, the repulsion and conformational asymmetry between A and B blocks with b_{P} (P=A,B) being the effective bond length of the P block, at the A-block volume fraction f=0.2 (where the copolymer chain length N=10) and 0.3 (where N=10 and 20). Consistent with previous SCF calculations[14, 16] of the "standard" model (*i.e.*, incompressible melts of continuous Gaussian chains with the Dirac δ-function non-bonded

potential), σ and A15 are the only stable Frank-Kasper (FK) phases among the five FK (*i.e.*, σ,

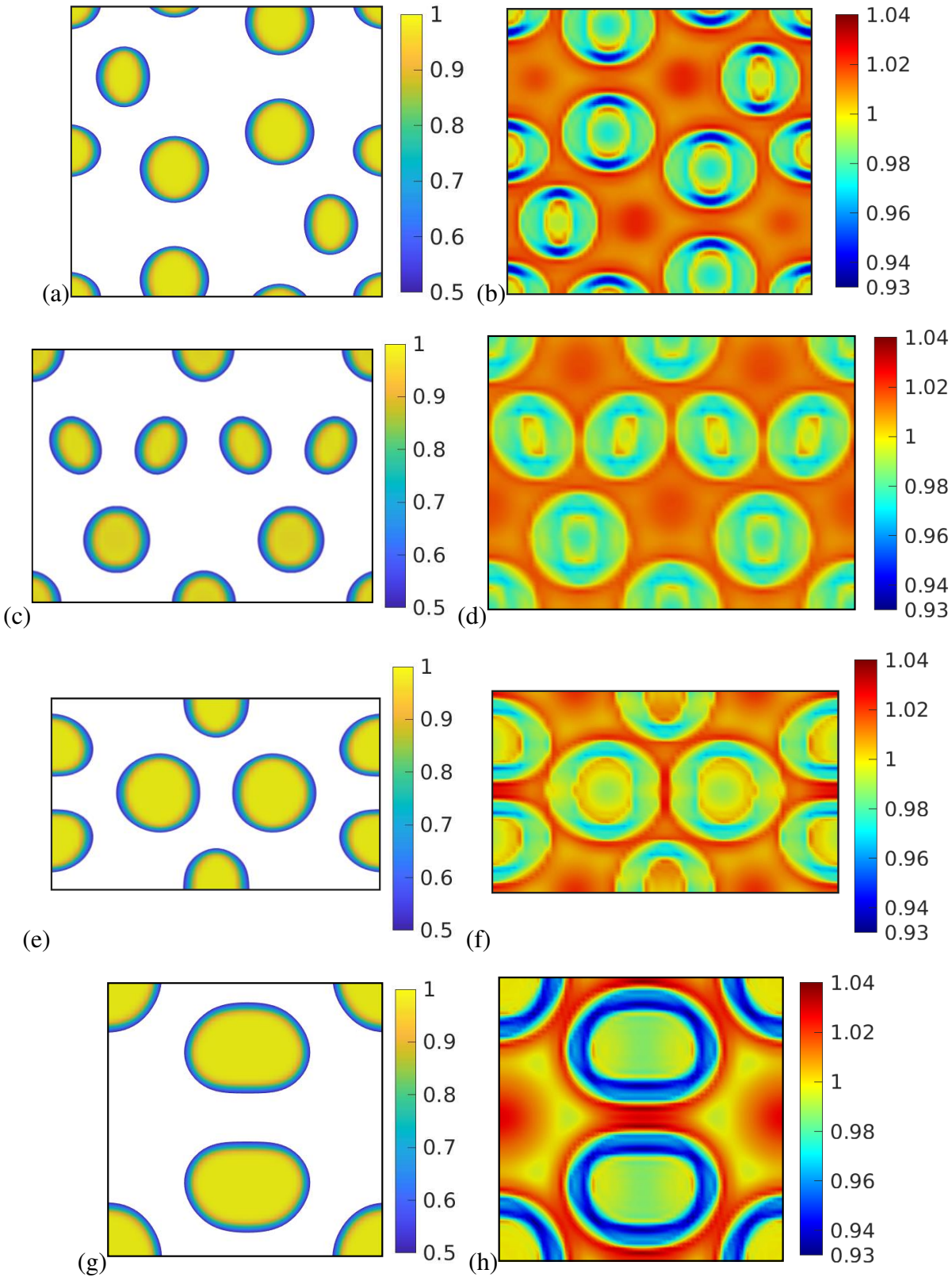

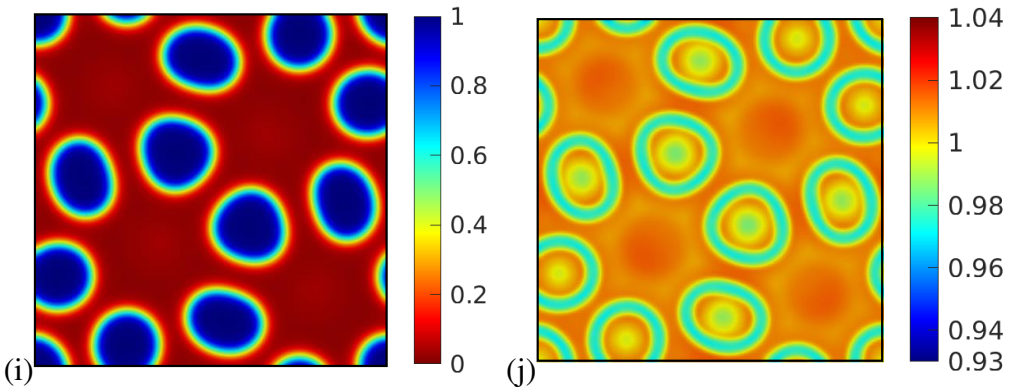

Figure 3.12. The normalized volume fraction profiles of A segments $\tilde{\phi}_{\mathrm{A}}(\mathbf{r}) \equiv \phi_{\mathrm{A}}(\mathbf{r})/\phi(\mathbf{r})$ (left column) and the total volume fraction profiles $\phi(\mathbf{r}) \equiv \phi_{\mathrm{A}}(\mathbf{r}) + \phi_{\mathrm{B}}(\mathbf{r})$ (right column) of (a,b) the C14 phase at f=0.2 and ε=4 along the (110) plane, (c,d) the C15 phase at f=0.2 and ε=4 along the (110) plane, (e,f) the Z phase at f=0.3 and ε=6.25 along the (110) plane, (g,h) the A15 phase at f=0.3 and ε=9 along the (100) plane, and (i,j) the σ phase at f=0.3 and ε=2.25 along the (001) plane. χN=40 for parts (a)~(h) and χN=23 for (i) and (j), N=10, N/κ=50π, and $b_{\mathrm{B}}/r_c = \sqrt{3}/2$. Parts (a), (c), (e), (g) and (i) can be qualitatively compared, respectively, with those for the "standard" model shown in Figs. S5(B) and S7(B) in Ref. 1, the right column of Figs. S18(F) and 3(D) in Ref. 2, and Fig. 6 in Ref. 3. See the main text for more details.

A15, C14, C15 and Z) phases considered here. The stability of σ is due to its delicate balance between the energetic and entropic contributions to the dimensionless (mean-field) Helmholtz free energy per chain βf_c. Within our parameter range, βf_c of the FK phases increase in the order of σ/A15, Z, C14 and C15 with their differences being on the order of 10^{-3} or smaller, and σ and A15 always have smaller internal energy per chain due to the A-B repulsion than Z, C14 and C15.

We have also calculated SCF phase diagrams for the "standard" model in the χN-ε plane at f=0.2 and 0.3, and compared them with those of the DPDC model. At f=0.2 the SCF phase diagram for the DPDC model at N=10 is qualitatively the same as that for the "standard" model, but they are qualitatively different at f=0.3 (where A15 is not stable for the DPDC model); the latter and any quantitative differences in the SCF phase diagrams are solely due to the

differences between these two models. On the other hand, A15 becomes stable for the DPDC model at f=0.3 and N=20, consistent with the fact that the DPDC model reduces to the "standard" model in the limit of $N\to\infty$, $b_P\to 0$ (at finite $\sqrt{N/6}b_B$, ε and b_B/r_c with r_c denoting the range of the DPD potential) and the generalized Helfand compressibility[74] $\kappa\to 0$.

Note that SCF theory inherently neglects the effects of system fluctuations/correlations, which are important to the low-molecular-weight A-B melts forming FK phases in experiments, and direct comparison between SCF and molecular (*i.e.*, molecular dynamics or Monte Carlo) simulation or field-theoretic simulation[75] results based on the same model system, thus without any parameter-fitting, is the only way to unambiguously quantify such effects. Since the "standard" model cannot be used in these simulations, this work provides the necessary mean-field reference for unambiguously quantifying the fluctuation/correlation effects with the DPDC model that can be readily used in both molecular and field-theoretic simulations.

REFERENCES

[1] F. C. Frank and J. S. Kasper, Acta Cryst. 11 (3), 184-190 (1958).

[2] F. C. Frank and J. S. Kasper, Acta Cryst. 12 (7), 483-499 (1959).

[3] V. Percec, C. H. Ahn, G. Ungar, D. J. P. Yeardley, M. Moller, and S. S. Sheiko, Nature 391 (6663), 161-164 (1998).

[4] G. Ungar, Y. S. Liu, X. B. Zeng, V. Percec, and W. D. Cho, Science 299 (5610), 1208-1211 (2003).

[5] B. K. Cho, A. Jain, S. M. Gruner, and U. Wiesner, Science 305 (5690), 1598-1601 (2004).

[6] X. B. Zeng, G. Ungar, Y. S. Liu, V. Percec, S. E. Dulcey, and J. K. Hobbs, Nature 428 (6979), 157-160 (2004).

[7] M. J. Huang, C. H. Hsu, J. Wang, S. Mei, X. H. Dong, Y. W. Li, M. X. Li, H. Liu, W. Zhang, T. Z. Aida, W. B. Zhang, K. Yue, and S. Z. D. Cheng, Science 348 (6233), 424-428 (2015).

[8] Z. B. Su, R. M. Zhang, X. Y. Yan, Q. Y. Guo, J. H. Huang, W. P. Shan, Y. C. Liu, T. Liu, M. J. Huang, and S. Z. D. Cheng, Prog. Polym. Sci. 103, 101230 (2020).

[9] A. Takano, W. Kawashima, A. Noro, Y. Isono, N. Tanaka, T. Dotera, and Y. Matsushita, J. Polym. Sci. B 43 (18), 2427-2432 (2005).

[10] K. Hayashida, W. Kawashima, A. Takano, Y. Shinohara, Y. Amemiya, Y. Nozue, and Y. Matsushita, Macromolecules 39 (14), 4869-4872 (2006).

[11] K. Hayashida, T. Dotera, A. Takano, and Y. Matsushita, Phys. Rev. Lett. 98 (19), 195502 (2007).

[12] S. Lee, M. J. Bluemle, and F. S. Bates, Science 330 (6002), 349-353 (2010).

[13] J. W. Zhang and F. S. Bates, J. Am. Chem. Soc. 134 (18), 7636-7639 (2012).

[14] M. W. Bates, J. Lequieu, S. M. Barbon, R. M. Lewis, K. T. Delaney, A. Anastasaki, C. J. Hawker, G. H. Fredrickson, and C. M. Bates, P. Natl. Acad. Sci. 116 (27), 13194-13199 (2019).

[15] A. J. Mueller, A. P. Lindsay, A. Jayaraman, T. P. Lodge, M. K. Mahanthappa, and F. S. Bates, ACS Macro Lett. 9 (4), 576-582 (2020).

[16] K. Kim, M. W. Schulze, A. Arora, R. M. Lewis, M. A. Hillmyer, K. D. Dorfman, and F. S. Bates, Science 356 (6337), 520-523 (2017).

[17] M. H. Uddin, C. Rodriguez, A. López-Quintela, D. Leisner, C. Solans, J. Esquena, and H. Kunieda, Macromolecules 36 (4), 1261-1271 (2003).

[18] K. Hayashida, A. Takano, S. Arai, Y. Shinohara, Y. Amemiya, and Y. Matsushita, Macromolecules 39 (26), 9402-9408 (2006).

[19] H. Takagi, R. Hashimoto, N. Igarashi, S. Kishimoto, and K. Yamamoto, J. Phys.: Condens. Mat. 29 (20), 204002 (2017).

[20] J. He and Q. Wang, Macromolecules, 57 (3), 1399-1401 (2024).

[21] H. Takagi and K. Yamamoto, Macromolecules 52 (5), 2007-2014 (2019).

[22] M. W. Schulze, R. M. Lewis, J. H. Lettow, R. J. Hickey, T. M. Gillard, M. A. Hillmyer, and F. S. Bates, Phys. Rev. Lett. 118 (20), 207801 (2017).

[23] H. Takagi, R. Hashimoto, N. Igarashi, S. Kishimoto, and K. Yamamoto, J. Fiber Sci. Technol. 74 (1), 10-16 (2018).

[24] A. P. Lindsay, R. M. Lewis, B. Lee, A. J. Peterson, T. P. Lodge, and F. S. Bates, ACS Macro Lett. 9 (2), 197-203 (2020).

[25] K. Yamamoto and H. Takagi, Mater. Trans. 62 (3), 325-328 (2021).

[26] A. P. Lindsay, G. K. Cheong, A. J. Peterson, S. Weigand, K. D. Dorfman, T. P. Lodge, and F. S. Bates, Macromolecules 54 (15), 7088-7101 (2021).

[27] Y. Miyamori, J. Suzuki, A. Takano, and Y. Matsushita, ACS Macro Lett. 9 (1), 32-37 (2020).

[28] G. M. Grason, B. A. DiDonna, and R. D. Kamien, Phys. Rev. Lett. 91 (5), 058304 (2003).

[29] S. T. Milner, Macromolecules 27 (8), 2333-2335 (1994).

[30] S. Lee, T. M. Gillard, and F. S. Bates, AIChE J. 59 (9), 3502-3513 (2013).

[31] S. Lee, C. Leighton, and F. S. Bates, P. Natl. Acad. Sci. 111 (50), 17723-17731 (2014).

[32] T. M. Gillard, S. Lee, and F. S. Bates, P. Natl. Acad. Sci. 113 (19), 5167-5172 (2016).

[33] C. Zhang, M. W. Bates, Z. S. Geng, A. E. Levi, D. Vigil, S. M. Barbon, T. Loman, K. T. Delaney, G. H. Fredrickson, C. M. Bates, A. K. Whittaker, C. J. Hawker, J. Am. Chem. Soc. 142 (21), 9843-9849 (2020).

[34] S. Jeon, T. Jun, S. Jo, H. Ahn, S. Lee, B. Lee, and D. Y. Ryu, Macromol. Rapid Commun. 40 (19), 1900259 (2019).

[35] S. Jeon, T. Jun, H. I. Jeon, H. Ahn, S. Lee, B. Lee, and D. Y. Ryu, Macromolecules 54 (20), 9351-9360 (2021).

[36] A. J. Mueller, A. P. Lindsay, A. Jayaraman, T. P. Lodge, M. K. Mahanthappa, and F. S. Bates, Macromolecules 54 (6), 2647-2660 (2021).

[37] A. P. Lindsay, A. Jayaraman, A. J. Peterson, M. W. Mueller, S. Weigand, K. Almdal, M. K. Mahanthappa, T. P. Lodge, and F. S. Bates, ACS Nano 15 (6), 9453-9468 (2021).

[38] S. M. Barbon, J.-A. Song, D. Chen, C. Zhang, J. Lequieu, K. T. Delaney, A. Anastasaki, M. Rolland, G. H. Fredrickson, M. W. Bates, C. J. Hawker, and C. M. Bates, ACS Macro Lett. 9 (12), 1745-1752 (2020).

[39] K. Kim, A. Arora, R. M. Lewis, M. J. Liu, W. H. Li, A. C. Shi, K. D. Dorfman, and F. S. Bates, P. Natl. Acad. Sci. 115 (5), 847-854 (2018).

[40] N. Xie, W. H. Li, F. Qiu, and A. C. Shi, ACS Macro Lett. 3 (9), 906-910 (2014).

[41] P. D. Olmsted and S. T. Milner, Phys. Rev. Lett. 72 (6), 936-939 (1994).

[42] P. D. Olmsted and S. T. Milner, Phys. Rev. Lett. 74 (5), 829-829 (1995).

[43] P. D. Olmsted and S. T. Milner, Macromolecules 31 (12), 4011-4022 (1998).

[44] A. Reddy, M. B. Buckley, A. Arora, F. S. Bates, K. D. Dorfman, and G. M. Grason, P. Natl. Acad. Sci. 115 (41), 10233-10238 (2018).

[45] L. Leibler, Macromolecules 13 (6), 1602-1617 (1980).

[46] M. W. Matsen and M. Schick, Phys. Rev. Lett. 72 (16), 2660-2663 (1994).

[47] G. H. Fredrickson, The equilibrium theory of inhomogeneous polymers. Oxford University Press: New York, (2006).

[48] G. Tzeremes, K. K. Rasmussen, T. Lookman, and A. Saxena, Phys. Rev. E 65 (4), 041806 (2002).

[49] H. D. Ceniceros and G. H. Fredrickson, Multiscale Model. Simul. 2 (3), 452-474 (2004).

[50] E. W. Cochran, C. J. Garcia-Cervera, and G. H. Fredrickson, Macromolecules 39 (7), 2449-2451 (2006).

[51] E. W. Cochran, C. J. Garcia-Cervera, and G. H. Fredrickson, Macromolecules 39 (12), 4264-4264 (2006).

[52] A. Ranjan, J. Qin, and D. C. Morse, Macromolecules 41 (3), 942-954 (2008).

[53] M. W. Matsen, Eur. Phys. J. E 30 (4), 361-369 (2009).

[54] A. Arora, D. C. Morse, F. S. Bates, and K. D. Dorfman, J. Chem. Phys. 146 (24), 244902 (2017).

[55] Y. Qiang and W. Li, Macromolecules 53 (22), 9943-9952 (2020).

[56] G. H. Fredrickson, E. Helfand, F. S. Bates, and L. Leibler, Springer Ser. Chem. Phys. 51, 13-19 (1989).

[57] G. H. Fredrickson, V. Ganesan, and F. Drolet, Macromolecules 35 (1), 16-39 (2002).

[58] K. T. Delaney and G. H. Fredrickson, J. Phys. Chem. B 120 (31), 7615-34 (2016).

[59] R. D. Groot and T. J. Madden, J. Chem. Phys. 108 (20), 8713-8724 (1998).

[60] E. Helfand and Y. Tagami, J. Polym. Sci. B: Polym. Lett. 9 (10), 741-746 (1971).

[61] K. Zhang and C. W. Manke, Comput. Phys. Commun. 129 (1-3), 275-281 (2000).

[62] L. J. Chen, Z. Y. Lu, H. J. Qian, Z. S. Li, and C. C. Sun, J. Chem. Phys. 122 (10), 104907 (2005).

[63] A. A. Gavrilov, Y. V. Kudryavtsev, and A. V. Chertovich, J. Chem. Phys. 139 (22), 224901 (2013).

[64] J. Glaser, P. Medapuram, T. M. Beardsley, M. W. Matsen, and D. C. Morse, Phys. Rev. Lett. 113 (6), 068302 (2014).

[65] P. Medapuram, J. Glaser, and D. C. Morse, Macromolecules 48 (3), 819-839 (2015).

[66] P. Sandhu, J. Zong, D. Yang, and Q. Wang, J. Chem. Phys. 138 (19), 194904 (2013).

[67] J. Zong and Q. Wang, J. Chem. Phys. 139 (12), 124907 (2013).

[68] J. Zong and Q. Wang, J. Chem. Phys. 143 (18), 184903 (2015).

[69] https://github.com/dmorse/pscfpp.

[70] A. Arora, J. Qin, D. C. Morse, K. T. Delaney, G. H. Fredrickson, F. S. Bates, and K. D. Dorfman, Macromolecules 49 (13), 4675-4690 (2016).

[71] G. K. Cheong, A. Chawla, D. C. Morse, and K. D. Dorfman, Eur. Phys. J. E 43 (2), 15 (2020).

[72] C. A. Tyler and D. C. Morse, Macromolecules 36 (21), 8184-8188 (2003).

[73] M. D. Sikiric, O. Delgado-Friedrichs, and M. Deza, Acta Cryst. A66, 602-615 (2010).

[74] E. Helfand and Y. Tagami, J. Polym. Sci. B: Polym. Lett. 9 (10), 741-746 (1971).

[75] G. H. Fredrickson, V. Ganesan, and F. Drolet, Macromolecules 35 (1), 16-39 (2002).

[76] J. He and Q. Wang, Macromolecules 55 (19), 8931-8939 (2022).

[77] R. P. Collanton and K. D. Dorfman, Phys. Rev. Matter. 6 (1) 15602 (2022)

4 ON THE RELATIVE STABILITY OF FRANK-KASPER PHASES FORMED BY NEAT DIBLOCK COPOLYMER MELTS AND BINARY BLENDS

4.1 Introduction

Understanding on the self-assembly of the simplest block copolymer system, linear and flexible diblock copolymer (DBC) melts, has been renewed since the experimental discovery of the Frank-Kasper (FK) σ phase in 2010[1]. Initially found in metallic alloys, FK phases refer to a class of complex structures where coordination polyhedra[2] have only triangular faces; the general principles regarding the combination of four types of such polyhedra into full structures with coordination numbers of 12, 14, 15 and 16, were deduced in the seminal work of Frank and Kasper[2, 3]. While 29 FK phases are known to date[4], only σ and A15 have been found to be stable in neat DBC melts[1, 5]; their stability over the conventional spherical phases such as the body- and face-centered cubic spherical phases (S_b and S_f, respectively) was first predicted by the polymer self-consistent field (SCF) calculations to be due to the conformational asymmetry between the two blocks[6] and later confirmed by experiments[7]. By blending two DBCs (denoted by A_1-B_1 and A_2-B_2) having different chain lengths and/or compositions (thus as limiting cases DBC 2 can also be homopolymer A_2 or B_2), C14 and C15 have also been found to be stable; the stability of these four FK phases in DBC blends, which can be conformationally symmetric, was again first predicted by the SCF calculations[8, 9] and later confirmed by experiments[10, 11]. This not only greatly expands the DBC systems that can form FK phases, but also provides new examples demonstrating the success of SCF theory in the study of block copolymer self-assembly.

Most SCF calculations of FK phases formed by neat DBC melts use the "standard" model (*i.e.*, incompressible systems of continuous Gaussian chains with the Dirac δ-function non-bonded interactions), which has the least number of parameters. Here we use f to denote the A-

Table 4.1. SCF phase diagrams of neat DBC melts reported in the literature. See the main text for more details.

Ref	N	f	ε	χN	**Fig** [a]
6 [b]	∞	0~1	2.25, 4	0~40	2
12		0~0.3	4	40	1C
			2.25, 4, 6.25	20, 30, 40	S2 [c]
13		0.23~0.33	4	25	S15
5		0~0.6	1~16	40	1L
		0~0.58	9	0~40	3C
14		0~0.4	1~9	60	2
15		0.2	1~4	0~40	3a
		0.3	1~9		3b
14 [d]	50	0~0.4	1~9	60	2
17 [e]	50, 100	0~0.58	9	40	5
16 [f]	10	0.2	1~4	0~40	2a
		0.3	1~9	0~23	2b
15 [f]	20	0.3	7~9	23~27	4c

[a] The figure number here refers to that in the original paper. [b] σ was the only FK phase considered in Ref. 6. [c] σ, C14 and C15 were the only FK phases shown in the figure. [d] Two models for incompressible melts of discrete Gaussian chains and freely jointed chains, respectively, with the Dirac δ-function non-bonded potential were used in Ref. 14. [e] A model for compressible melts of discrete Gaussian chains with the Gaussian non-bonded potential was used in Ref. 17. [f] The dissipative particle dynamics chain (DPDC) model for compressible melts of discrete Gaussian chains with the DPD non-bonded potential was used in Refs. 15 and 16.

block volume fraction in the copolymer, $\varepsilon \equiv a_A^2 / a_B^2$ the conformational asymmetry between the two blocks (we assume that all segments have the same volume) with a_P being the statistical segment length of the P (=A,B) block, and χN the segregation between the two blocks with χ being the (generalized) Flory-Huggins interaction parameter and N the copolymer chain length; for the "standard" model, $N \to \infty$. Table 4.1 summarizes the SCF phase diagrams of neat DBC melts[5, 6, 12-17] reported so far. These SCF calculations showed that regardless of the various models used, only σ and A15 are stable FK phases while C14, C15, H, Z and pσ are unstable. Very recently, Chen and Dorfman showed via SCF calculations of the "standard model" of neat

DBC melts that both μ and the newly discovered Φ^4 are unstable at f=0.25, ε=2.25 and χN=20.[18]

Most SCF calculations of FK phases formed by binary DBC blends (including those with A_2 or B_2) also use the "standard" model. Here we use f_i, N_i and ϕ_i to denote the A-block volume fraction, chain length and overall volume fraction of DBC i (=1,2), respectively, with $\phi_1=1-\phi_2$, and take $N=N_1$ and $r \equiv N_2/N_1$. Table 4.2 summarizes the SCF phase diagrams of binary DBC blends[8, 9, 11, 19-23] reported so far; note that all these studies used the "standard" model, except that Refs. 22 and 23 used incompressible blends of freely jointed chains of N=80 and 40, respectively, with the Gaussian non-bonded potential. These SCF calculations showed that in the blends C14 and C15 become stable in addition to σ and A15. Magruder and Dorfman further showed via SCF calculations of the "standard model" of A_1-B_1/A_2 that C36 is unstable as its Helmholtz free-energy density is always in-between those of C14 and C15 due to the similarity of their structures.[24] Similar results were found by Li and co-workers in their SCF calculations of the "standard" model of A_1-B_1/A_2-B_2, who studied "binary" spherical phases formed at large r>2.[20] Other FK phases have not yet been considered in SCF calculations of DBC systems.

Most explanations on the stability of FK phases in DBC systems are based on their structures. Given that minority (A) domains of different sizes and shapes are contained in one unit cell of an FK phase, unlike the conventional spherical phases where all the A-domains are the same, Bates and co-workers proposed that the Wigner-Seitz (WS) polyhedra of σ are on average closer to spherical, as quantified by the mean isoperimetric quotient of the WS polyhedra being closer to 1, than that of S_b and can therefore better accommodate the tendency to minimize distortions away from a spherical particle shape.[25] For neat DBC melts, Grason and co-workers applied a diblock foam model (DFM)[26-28] in the strong-segregation limit and the polyhedral-interface limit (where a chain in a WS polyhedron extends along the radial direction from its

Table 4.2. SCF phase diagrams of binary DBC blends reported in the literature. See the main text for more details.

Ref	f_1	f_2 [a]	ε	χN	r	ϕ_2	**Ens**[b]	**Fig**[c]
8 [d]	0.15	0.45/r	1	40	0.6~2	0~0.75	G	2b
	0.22	0.5		20	1.56	0~0.4	C, G	S3
9	0.15	$1-(1-f_1)/r$	1	40	1.05~2	0~0.6	G	2B
			4		1.02, 1.06, 1.1, 1.2	0.1~0.4	C	S1
11	0.12	0.38	1.7	20~30 [e]	1.4	0~1	G	10B
				30~40 [e]			C	S12
19	0.2	0.3, 0.5, 0.7	1	0~40	1.5	0~1	G	1
		0.5			0.5, 1			2a, 2b
20	0.23	$1-(1-f_1)/r$	1	20	1.6~4.05	0~0.54	G	1
	0.15			40	2.4, 2.7	0~0.5		11
21	0.18	1	1	25	0.12, 0.14, 0.18	0~1	C, G	S3B
			1.7	20	0.12, 0.14, 0.18			S2B
				25	0.12, 0.14, 0.18			2
				30	0.18			S1A
22	0.15		1	0~40	0.15	0~0.17	G	4a
	0.2				0.1125, 0.2			3b, 3a
	0.25				0.25			4c
	0.2		1.5625		0.1125, 0.2			3d, 3c
23	0.25	0	1.44	0~36	0.125, 0.75	0~0.7	G	6

[a] $f_2=1-(1-f_1)/r$ for the case where the B-blocks in both DBCs 1 and 2 have the same length, $f_2=1$ for homopolymer A_2, and $f_2=0$ for B_2. [b] C and G here denote the canonical and the grand-canonical ensemble, respectively. [c] The figure number here refers to that in the original paper. [d] C14 and C15 were not considered in Ref. 8. [e] χN in Ref. 11 refers to $\chi(\phi_1 N_1+\phi_2 N_2)$.

center to its surface with the A-B interface having the same shape as the polyhedron) to eleven FK phases (*i.e.*, σ, A15, C14, C15, H, Z, P, M, pσ, μ and δ), and found that while C15 has the smallest mean dimensionless area and S_b has the smallest mean dimensionless stretching of WS polyhedra, σ has the optimal balance between these two (thus the lowest free-energy density).[13]

The structure and thermodynamics of self-assembled phases of block copolymers are intimately connected, and it is the free-energy density that ultimately determines which phase is

stable at a given state point in the parameter space. Under the mean-field approximation, polymer SCF theory can provide detailed insights into the stability of various phases, as the dimensionless Helmholtz free-energy per chain of N segments βf_c and its various components are readily calculated from the converged conjugate fields and volume-fraction fields $\{\phi_P(\mathbf{r})\}$; here $\beta \equiv 1/k_B T$ with k_B denoting the Boltzmann constant and T the thermodynamic temperature of the system. In addition to the above DFM results, Grason and co-workers performed SCF calculations of seven FK phases (σ, A15, C14, C15, H, Z and pσ) formed by neat DBC melts and geometric analysis of the shape of the A-B interfaces (where A and B segments have the same volume fraction, *i.e.*, $\phi_A(\mathbf{r})=\phi_B(\mathbf{r})=1/2$) and their enclosed volume.[13] Collanton and Dorfman also performed similar geometric analysis of their SCF results of S_b, S_f, σ and A15 formed by neat DBC melts, and found that the imprinting of the WS polyhedra onto the A-B interfaces is significantly larger for A15 and σ than S_f and S_b and that the imprinting gap at the S_b/σ transition decreases with increasing ε. They further found that increasing imprinting is concurrent with sharpening of A-B interfaces (thus reduction in the dimensionless internal energy per chain βu_c), which drives the S_b to σ transition.[29]

For binary blends of A_1-B_1/A_2-B_2, Shi and co-workers found in their SCF calculations that large values of f_2 and r are both needed to stabilize the FK phases.[19] They proposed that the inter-domain segregation of DBCs 1 and 2 favors the formation of A-domains of different sizes, that their intra-domain segregation along the radial direction results in a core-shell structure of each A-domain formed by the longer A_2 and shorter A_1 blocks (which enables large A-domains), and that their intra-domain segregation along the A-B interfaces releases the frustration of forming non-spherical A-domains, thus enhancing the stability of the FK phases.[8, 19] For binary blends of A_1-B_1/A_2, Dorfman and co-workers found in their SCF calculations the sequence of

$S_b \rightarrow \sigma \rightarrow C14 \rightarrow C15 \rightarrow C$ (hexagonally packed cylinders) with the addition of A_2 at $r=f_1$ (*i.e.*, in the dry-brush regime), which can be explained by the increased volume difference between the spheres in these phases, and the shrinking/extinction of the FK phases with decreasing r.[21] Similar results were also obtained by Xie and Shi in their SCF calculations, who proposed that the sizes of A-domains are regulated by the differential localization of A_2 and that the resultant A-domains of different sizes is a key factor to stabilize the FK phases (especially C14 and C15).[22] Finally, for binary blends of A_1-B_1/B_2, Xie and Shi found in their SCF calculations that B_2 is more concentrated near the vertices and edges of the WS polyhedra, which releases the packing frustrations induced by both the non-sphericity and non-uniformity of A-domains and lowers the conformational asymmetry required to form σ (the only stable FK phase found so far), and that longer B_2 shrinks the stability window of σ.[23]

With the stability mechanism of FK phases over conventional spherical phases formed by neat DBC melts and binary DBC blends generally established, we are interested in why some FK phases are stable while others are not in such systems. As aforementioned, to date only σ and A15 are stable in neat DBC melts and only C14 and C15 become stable in binary DBC blends in addition to σ and A15. Recently, two of us found that σ and A15 have lower βu_c than some other FK phases (*i.e.*, C14, C15 and Z) formed by neat DBC melts using SCF calculations of the dissipative particle dynamics chain (DPDC) model.[15, 16] Here we report similar results for both neat DBC melts and binary blends of A_1-B_1/A_2-B_2 obtained from our SCF calculations of the "standard" model with H and pσ also included, which for the latter system are complementary to the structural analysis of Shi and co-workers[8, 19]. This trend is also found in other groups' SCF data for both neat DBC melts and binary blends of A_1-B_1/A_2 as described in detail below.

4.2 Model and Method

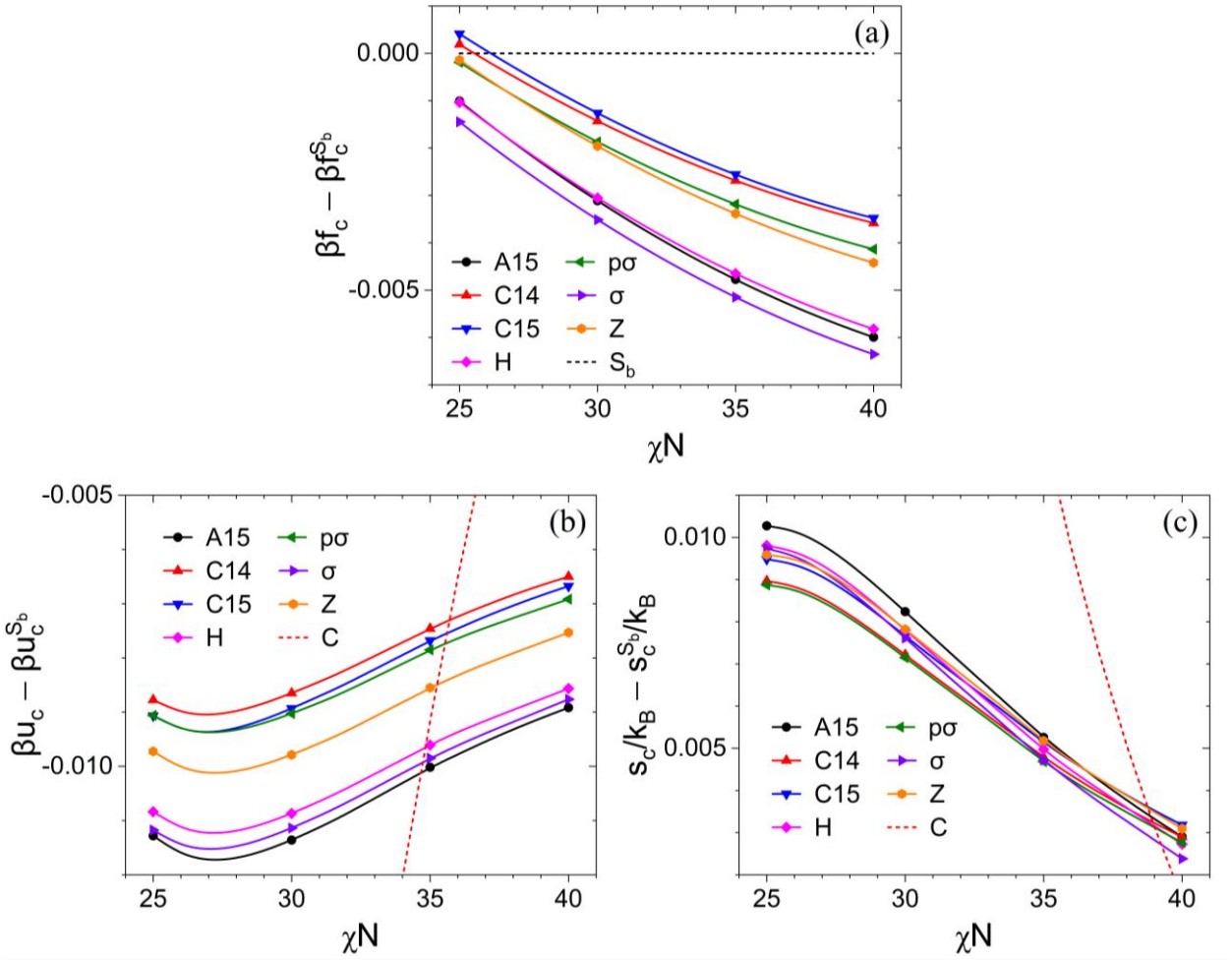

Figure 4.1. The dimensionless (a) Helmholtz free energy per chain βf_c, (b) internal energy per chain βu_c and (c) entropy per chain s_c/k_B of various ordered phases, relative to that of S_b, formed by neat DBC melts as functions of the segregation between the two blocks χN at the A-block volume fraction f=0.25 and conformational asymmetry ε=4. Since for χN=25~40 $\beta f_c^{C} - \beta f_c^{S_b} = 1.21\times10^{-2} \sim 3.3\times10^{-3}$ and $\beta f_c^{S_f} - \beta f_c^{S_b} = 2.5\times10^{-3} \sim 6.7\times10^{-3}$, results of non-FK phases (*i.e.*, C, S_b and S_f) are only partially or not shown for clarity. See the main text for more details.

As in Refs. 15, 16, we perform our SCF calculations using PSCF+, an improved and extended C++/CUDA version of PSCF; the latter is a software package for SCF calculations of the "standard" model and was used in Refs. 12, 13. We refer the readers to Refs. 5, 6, 12, 13 and 8, 20 for the SCF equations of neat DBC melts and binary DBC blends, respectively, and Ref. 15 for the major numerical improvement of PSCF+ over PSCF, namely the Richardson extrapolated

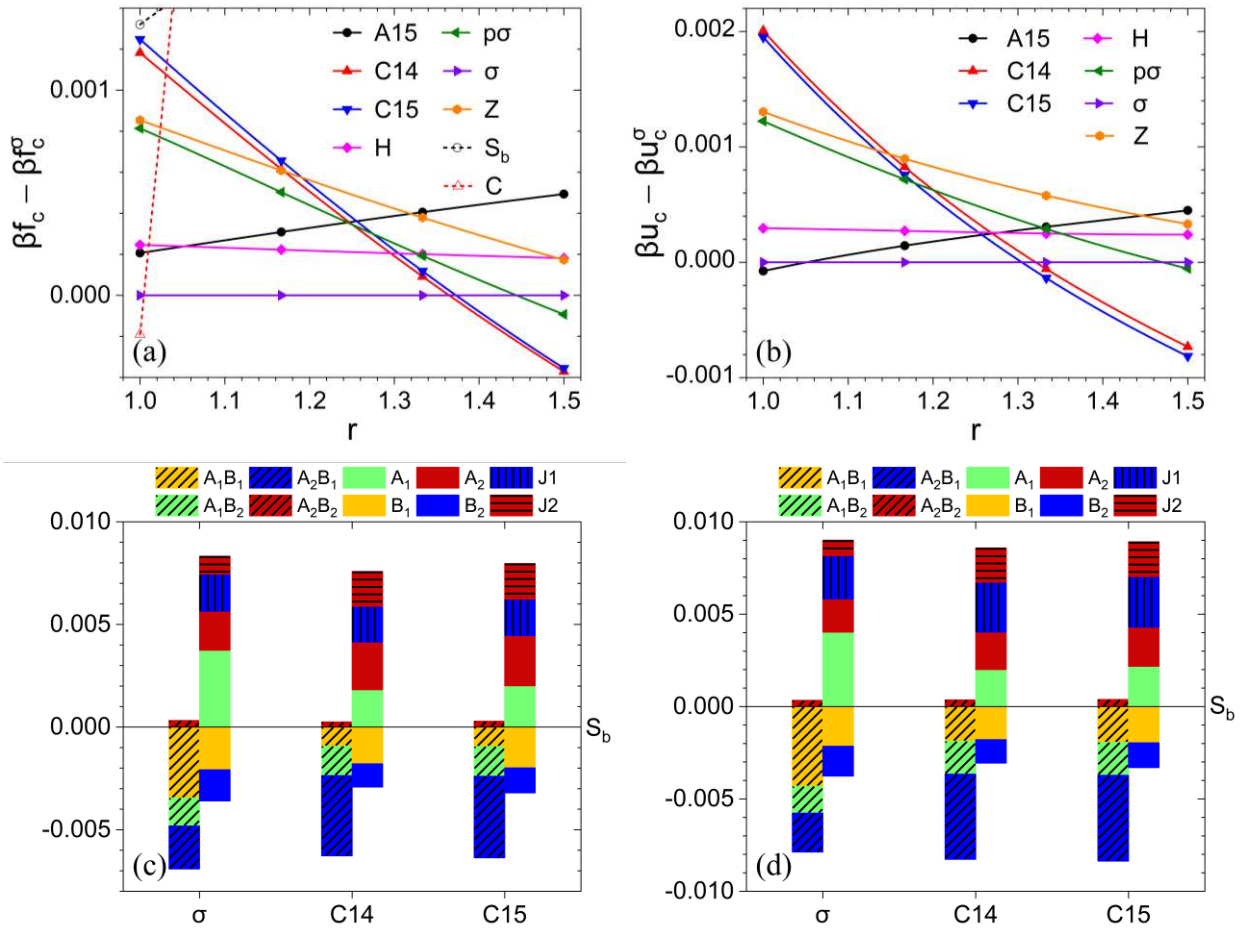

Figure 4.2. The dimensionless (a) Helmholtz free energy per chain βf_c and (b) internal energy per chain βu_c of various ordered phases, relative to that of σ, formed by binary blends of conformationally symmetric DBCs 1 and 2 as functions of the copolymer length ratio $r \equiv N_2/N_1$ at the A-block volume fractions f_1=0.2 and f_2=0.5, the volume fraction of DBC 2 in the system ϕ_2=1/6, and the segregation between the two blocks χN_1=25. Since for r=1.0~1.5, $\beta f_c^{\mathrm{C}} - \beta f_c^{\sigma} = -2\times10^{-4} \sim 1.56\times10^{-2}$, $\beta f_c^{\mathrm{S_b}} - \beta f_c^{\sigma} = 1.3\times10^{-3} \sim 2.5\times10^{-3}$ and $\beta f_c^{\mathrm{S_f}} - \beta f_c^{\sigma} = 2.1\times10^{-3} \sim 2.9\times10^{-3}$, results of non-FK phases (*i.e.*, C, S_b and S_f) are only partially or not shown for clarity. Parts (c) and (d) show the various contributions to βu_c and the dimensionless entropy per chain $s_c/k_B = \beta f_c - \beta u_c$ relative to that of S_b at r=1.2 and 1.4, respectively. See the main text for more details.

pseudo-spectral (REPS-*K*) methods.

4.3 Results and Discussion

We first determine the values of four numerical parameters (*i.e.*, the spatial discretization parameter m, the chain-contour discretization parameter n_s, K of the REPS method, and the

convergence criterion ε_0 for solving the SCF equations) needed to achieve an accuracy of our βf_c to be higher than 10^{-5} at χN=40. Following Ref. 15, for this we use neat DBC melts at f=0.25 and ε=4 for all the phases considered here (except ε=2.25 for σ, H and pσ), and find that m=64, n_s=128 (with K=2) and $\varepsilon_0=10^{-6}$; results for the ten ordered phases (*i.e.*, C, S_b, S_f, σ, A15, C14, C15, H, Z and pσ) considered in this work are shown in Chapter 3, along with the discretization of their unit cell.

Fig. 4.1 shows βf_c, βu_c and the dimensionless entropy per chain $s_c/k_B = \beta f_c - \beta u_c$ for various ordered phases, relative to that of S_b, formed by neat DBC melts at f=0.25, ε=4 and χN=25~40. We see that σ is the stable phase, and that σ and A15 have lower βu_c than other FK phases; the latter is consistent with the recent SCF results of the DPDC model shown in Refs. 15,

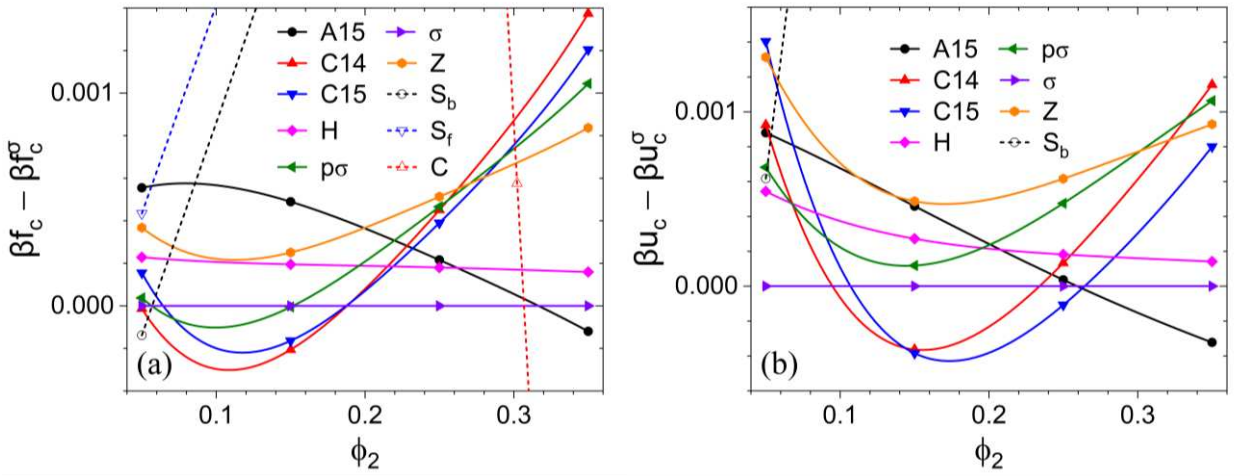

Figure 4.3. The dimensionless (a) Helmholtz free energy per chain βf_c and (b) internal energy per chain βu_c of various ordered phases, relative to that of σ, formed by binary blends of conformationally symmetric DBCs 1 and 2 as functions of the volume fraction of DBC 1 in the system ϕ_2 at the A-block volume fractions f_1=0.2 and f_2=0.5, the copolymer length ratio $r \equiv N_2/N_1 = 1.4$ and the segregation between the two blocks χN_1=25. Since for ϕ_2=0.05~0.35, $\beta f_c^{S_b} - \beta f_c^{\sigma} = -1\times10^{-4} \sim 6.2\times10^{-3}$, $\beta f_c^{S_f} - \beta f_c^{\sigma} = 4\times10^{-4} \sim 7.1\times10^{-3}$ and $\beta f_c^{C} - \beta f_c^{\sigma} = 1.28\times10^{-2} \sim -5.82\times10^{-3}$, results of non-FK phases (*i.e.*, C, S_b and S_f) are only partially or not shown for clarity. See the main text for more details.

16, as well as the SCF data of the "standard" model at various f, ε and χN for Ref. 12 deposited in a repository[30] and those for Ref. 13 shared with us[31].

For binary blends of A_1-B_1/A_2-B_2, our SCF calculations are performed in the canonical ensemble; previous comparative studies[8, 11] showed that grand-canonical-ensemble calculations give a two-phase coexistence region around the boundary between the two stable phases obtained in canonical-ensemble calculations. Here we consider conformationally symmetric DBCs (*i.e.*, ε=1) at f_1=0.2, f_2=0.5 and χN=25, and set ϕ_2=1/6 such that the overall volume fraction of A-blocks in the system is the same as f=0.25 in the above neat DBC melts (although this is not necessary as shown below, and Fig. 4.4 shows our phase diagram for the blends in the r-ϕ_2 plane); we also use a step size not larger than 1/128 for the chain-contour discretization. Fig. 4.2(a) shows that σ is the stable phase for r<1.365 while C14 becomes the stable phase for larger r; this is consistent with the SCF phase diagrams of the same model system obtained in the grand-canonical ensemble by Shi and co-workers[19], which indicate that σ and C co-exist at r=1 and that C14 is the stable phase at r=1.5. Fig. 4.2(b) shows that C14 and C15 have lower βu_c

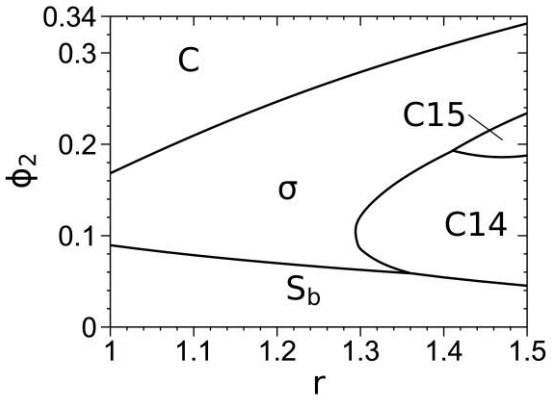

Figure 4.4. Our SCF phase diagram for conformationally symmetric A_1-B_1/A_2-B_2 in the r-ϕ_2 plane at f_1=0.2, f_2=0.5 and χN=25 calculated in the canonical ensemble. See the main text for more details.

than other FK phases for $r \gtrsim 1.32$; this is consistent with the above trend found for σ and A15 in neat DBC melts, suggesting the dominance of βu_c in determining the relative stability among various FK phases.

We can further decompose βu_c into contributions from the repulsion between A_i and B_j blocks ($\{i,j\}=\{1,2\}$), and s_c/k_B into contributions from the conformational entropy of A_i and B_i blocks and the translational entropy of the A-B junction J_i of DBC i.[32] Figs. 4.4(c) and 4.4(d) show these contributions for σ, C14 and C15 at r=1.2 and 1.4, respectively. Our SCF data indicate that as r increases from 1.2 to 1.4, the decrease in $\Delta f \equiv \beta f_c^{\mathrm{C14}} - \beta f_c^{\sigma}$, which is about 1.3×10^{-3}, is mainly (about 73%) due to that in $\Delta u \equiv \beta u_c^{\mathrm{C14}} - \beta u_c^{\sigma}$, which in turn is nearly all due to that in the interchain repulsion; that is, the decrease in the repulsion between A_2 and B_1 blocks accounts for about 74%, while that between A_1 and B_2 blocks accounts for about 26%, of the decrease in Δu; these numbers of course depend on the selected r-range.

For binary blends of A_1-B_1/A_2-B_2, Shi and co-workers showed that DBCs 1 and 2 segregate within each A-domain, which exhibits an anisotropic "core-shell" structure.[8, 19] Consistent with their results, Figs. 4.5(a) and 4.5(b) clearly show that the (shorter) A_1- and (longer) A_2-blocks form the shell and core, respectively, of each A-domain. On the other hand, we note that all faces of the Z12 WS polyhedra are pentagons, while Z14, Z15 and Z16 WS polyhedra have 2, 3 and 4 hexagonal faces, respectively, each having a six-fold rotation axis. Fig. 4.5(d) then clearly shows that the (shorter, compared to the B_1-block) B_2-block has higher volume fraction along the six-fold rotation axes of WS polyhedra. As r increases from 1.2 to 1.4, Fig. 4.6(a) shows that the A_1-block accumulates in the shell but depletes in the core of each A-domain, Fig. 4.6(b) shows that in each phase the WS polyhedra having more six-fold rotation

Table 4.3. Fraction of WS polyhedra f_z (z=12,14,15,16) and the average coordination number $\overline{z}$ of various FK phases; see the main text for details.

Phase	f_{12}	f_{14}	f_{15}	f_{16}	$\overline{z}$
A15	1/4	3/4	0	0	13.5
σ/H	1/3	8/15	2/15	0	13.467
Z	3/7	2/7	2/7	0	13.429
pσ	7/13	2/13	2/13	2/13	13.385
C14/C15	2/3	0	0	1/3	13.333

axes attract more A_2-block, Fig. 4.6(c) shows that the B_1-block accumulates around Z12 and Z14 WS polyhedra but depletes around Z16 WS polyhedra (in C14), and Fig. 4.6(d) shows that the B_2-block accumulates around the six-fold rotation axes connecting two Z16 WS polyhedra (in C14) but spreads into the B_1-block domains for other WS polyhedra pairs. These explain the above change in Δu.

The dominance of βu_c in determining the relative stability among various FK phases is also found for the above binary blends at r=1.4 as ϕ_2 varies. Fig. 4.5(a) shows that σ is the stable phase for ϕ_2>0.192 while C14 becomes the stable phase for smaller ϕ_2 (note that S_b is the stable phase for neat A_1-B_1 melt and C is the stable phase for ϕ_2>0.307 here), and Fig. 4.5(b) shows that C14 and C15 have lower βu_c than other FK phases for $0.26 \gtrsim \phi_2 \gtrsim 0.1$ (clearly the entropic effects, although less important, are not negligible here). This trend is further found in the SCF data for binary blends of A_1-B_1/A_2 at f_1=0.2, ε=1.5625 and χN=36 shown in figures 6 and 8 (where ϕ_2 varies at r=f_1 and r varies at ϕ_2=0.07, respectively) of Ref. 22 obtained by Xie and Shi using incompressible blends of freely jointed chains with the Gaussian non-bonded potential.

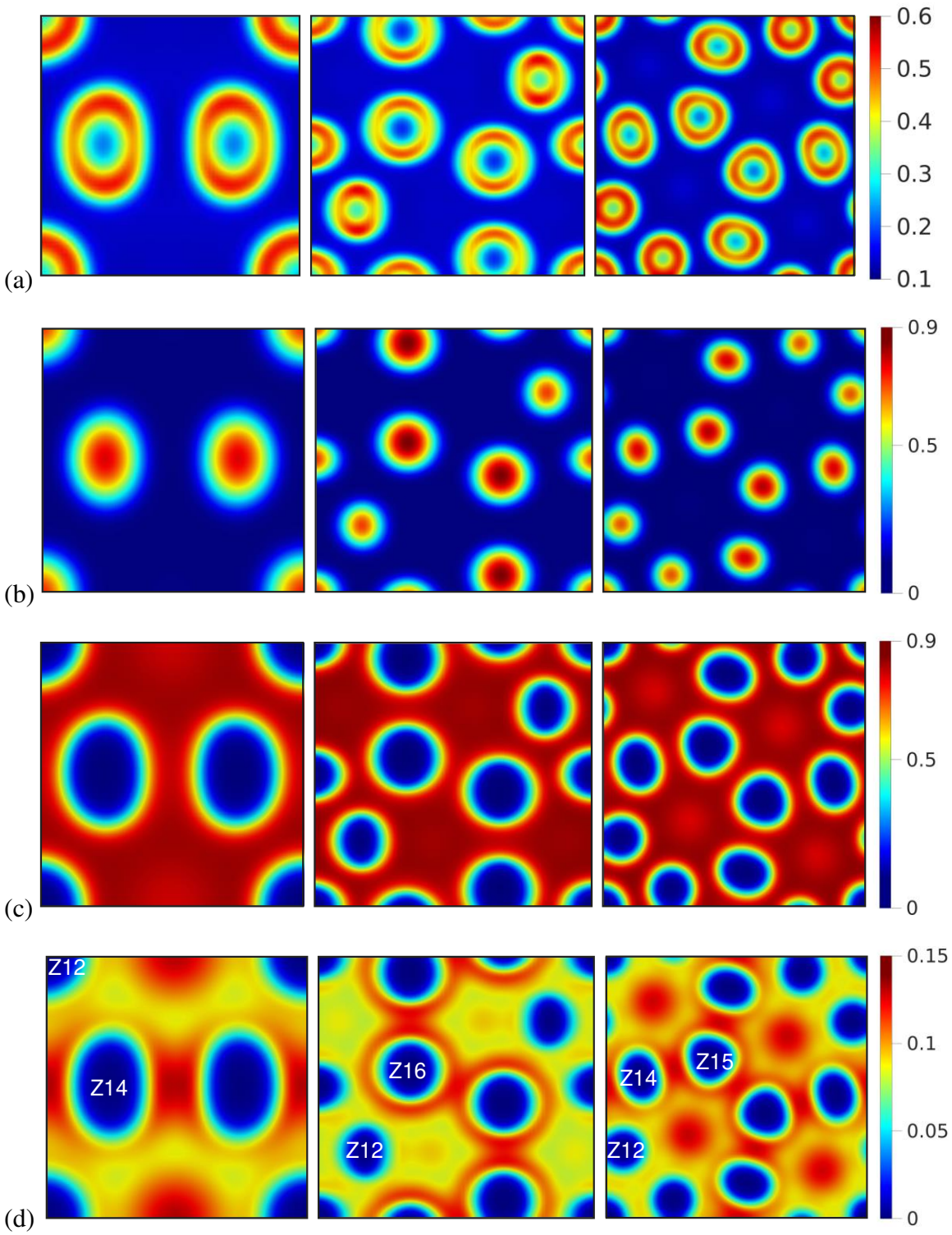

Figure 4.5. 2D volume-fraction profiles $\phi(\mathbf{r})$ of (a) A_1, (b) A_2, (c) B_1 and (d) B_2 in (from left to right) A15 [the (001) plane], C14 [the (110) plane] and σ [the (001) plane] at r=1.4, χN=25, ϕ_2=1/6, f_1=0.2 and f_2=0.5. See the main text for more details

For an FK phase, we can define its average coordination number (CN) $\bar{z} \equiv \sum_z z f_z$, where

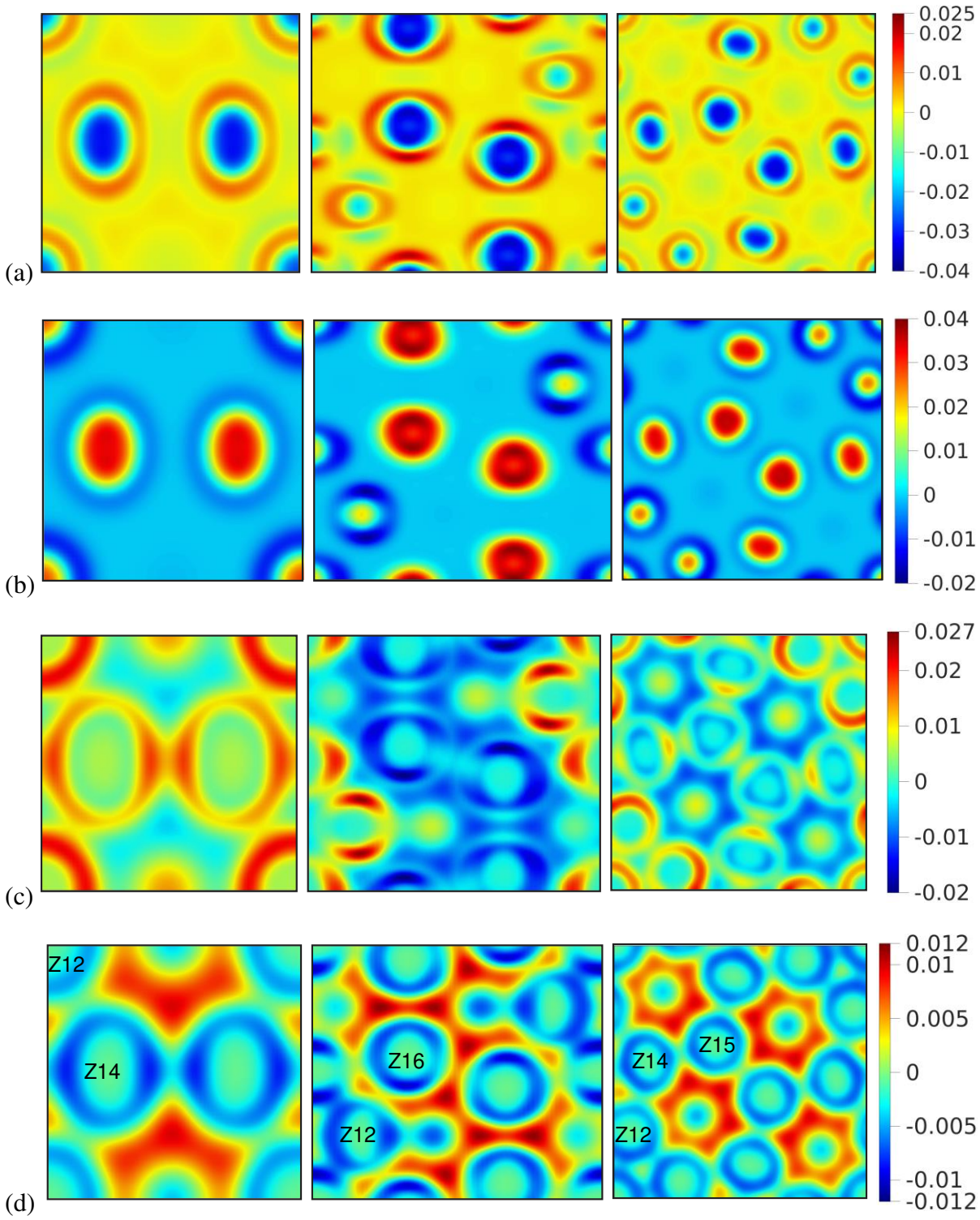

Figure 4.6. Similar to Fig. 4.5, but for $\phi(\mathbf{r}; r{=}1.4) - \phi(\mathbf{r}; r{=}1.2)$. See the main text for more details.

polyhedra in the FK phase given in Table III; note that since WS polyhedra with CN of z have $z-12$ six-fold rotation axes, $\overline{z}$ is equivalent to the average number of the latter. Inspecting the βf_c- (and βu_c-)curves of various FK phases shown in Figs. 4.1~4.3, we see that their variations are clearly correlated with $\overline{z}$; to be more specific, the βf_c- (and βu_c-)curves of the FK phases having the same $\overline{z}$ are almost "parallel" to each other, and the curve variations for different FK phases follow the same increasing/decreasing order of their $\overline{z}$. While $\overline{z}$ was calculated for various FK phases in Ref. 13, this is the first time such correlation is reported.

To summarize, we have found in SCF calculations performed by several groups that the relative stability among seven FK phases (A15, σ, H, Z, pσ, C14 and C15) formed by DBC systems is dominated by their internal-energy densities (*i.e.*, the repulsion between A and B blocks); this is the case for both neat DBC melts and binary DBC blends (including A_1-B_1/A_2-B_2 and A_1-B_1/A_2), regardless of the detailed models used (including the "standard" model, the DPDC model, and that of incompressible melts of freely jointed chains with the Gaussian non-bonded potential). We have also found that the variations of βf_c- (and βu_c-)curves of different FK phases in these calculations are clearly correlated with their $\overline{z}$. Finally, the change of stable phase between σ and C14/C15 in binary DBC blends is mainly due to that in the interchain repulsion. Clearly, SCF calculations of more FK phases formed by DBC systems are needed and, since $\overline{z}$ cannot be used to determine the relative stability of the FK phases, other structural indicators need to be analyzed to further reveal the relation between structures and thermodynamics of these fascinating self-assembled morphologies.

REFERENCES

[1] S. Lee, M. J. Bluemle, and F. S. Bates, Science, 330 (6002), 349-353 (2010).

[2] F. C. Frank and J. S. Kasper, Acta Cryst., 11 (3), 184-190 (1958).

[3] F. C. Frank and J. S. Kasper, Acta Cryst., 12 (7), 483-499 (1959).

[4] X. Y. Liu, X. Y. Yan, Y. Liu, H. Qu, Y. Wang, J. Wang, Q. Y. Guo, H. Lei, X. H. Li, F. Bian, X. Y. Cao, R. Zhang, Y. Wang, M. Huang, Z. Lin, E. W. Meijer, T. Aida, X. Kong, and S. Z. D. Cheng, Nat. Mater., 23 (4), 570-576 (2024).

[5] M. W. Bates, J. Lequieu, S. M. Barbon, R. M. Lewis, K. T. Delaney, A. Anastasaki, C. J. Hawker, G. H. Fredrickson, and C. M. Bates, P. Natl. Acad. Sci., 116 (27), 13194-13199 (2019).

[6] N. Xie, W. H. Li, F. Qiu, and A. C. Shi, ACS Macro Lett., 3 (9), 906-910 (2014).

[7] M. W. Schulze, R. M. Lewis, J. H. Lettow, R. J. Hickey, T. M. Gillard, M. A. Hillmyer, and F. S. Bates, Phys. Rev. Lett., 118 (20), 207801 (2017).

[8] M. J. Liu, Y. C. Qiang, W. H. Li, F. Qiu, and A. C. Shi, ACS Macro Lett., 5 (10), 1167-1171 (2016).

[9] K. Kim, A. Arora, R. M. Lewis, M. J. Liu, W. H. Li, A. C. Shi, K. D. Dorfman, and F. S. Bates, P. Natl. Acad. Sci., 115 (5), 847-854 (2018).

[10] A. P. Lindsay, R. M. Lewis, B. Lee, A. J. Peterson, T. P. Lodge, and F. S. Bates, ACS Macro Lett., 9 (2), 197-203 (2020).

[11] A. P. Lindsay, G. K. Cheong, A. J. Peterson, S. Weigand, K. D. Dorfman, T. P. Lodge, and F. S. Bates, Macromolecules, 54 (15), 7088-7101 (2021).

[12] K. Kim, M. W. Schulze, A. Arora, R. M. Lewis, M. A. Hillmyer, K. D. Dorfman, and F. S. Bates, Science, 356 (6337), 520-523 (2017).

[13] A. Reddy, M. B. Buckley, A. Arora, F. S. Bates, K. D. Dorfman, and G. M. Grason, P. Natl. Acad. Sci., 115 (41), 10233-10238 (2018).

[14] D. L. Vigil, T. Quah, D. Sun, K. T. Delaney, and G. H. Fredrickson, Macromolecules, 55 (11), 4237-4244 (2022).

[15] J. He and Q. Wang, Polymers, 16 (3), 372 (2024).

[16] J. He and Q. Wang, Macromolecules, 57 (3), 1399-1401 (2024).

[17] J. Lequieu, J. Chem. Phys., 158 (24), 244902 (2023).

[18] P. Chen and K. D. Dorfman, Nat. Mater., 23 (4), 455-456 (2024).

[19] J. Xie, Y. Li, and A. C. Shi, Macromol. Theory Simul., 30 (6), 2100053 (2021).

[20] F. Zhao, Q. Dong, Q. Li, M. Liu, and W. Li, Macromolecules, 55 (22), 10005-10013 (2022).

[21] G. K. Cheong, F. S. Bates, and K. D. Dorfman, P. Natl. Acad. Sci., 117 (29), 16764-16769 (2020).

[22] J. Xie and A.-C. Shi, Giant, 5, 100043 (2021).

[23] J. Xie and A.-C. Shi, Macromolecules, 56 (24), 10296-10312 (2023).

[24] B. R. Magruder and K. D. Dorfman, Soft Matter, 17 (39), 8950-8959 (2021).

[25] S. Lee, C. Leighton, and F. S. Bates, P. Natl. Acad. Sci., 111 (50), 17723-17731 (2014).

[26] P. D. Olmsted and S. T. Milner, Phys. Rev. Lett., 72 (6), 936-939 (1994).

[27] P. D. Olmsted and S. T. Milner, Phys. Rev. Lett., 74 (5), 829-829 (1995).

[28] P. D. Olmsted and S. T. Milner, Macromolecules, 31 (12), 4011-4022 (1998).

[29] R. P. Collanton and K. D. Dorfman, Phys. Rev. Mater., 6 (1), 015602 (2022).

[30] https://conservancy.umn.edu/handle/11299/188126.

[31] A. Reddy, K. D. Dorfman, and G. M. Grason, private communication (2020).

[32] C. Hawthorne, J. He, and Q. Wang, Phys. Rev. Mater., 8 (4), 045604 (2024).

5 STABLE AND UNSTABLE TILING PATTERNS FORMED BY ABC MIKTOARM STAR TRIBLOCK TERPOLYMERS OF SYMMETRIC INTERACTIONS

5.1 Introduction

The self- and directed assembly of block copolymers has attracted long-standing interest due to its both fundamental and practical importance.[1, 2] While the self-assembled morphologies formed by the simplest block copolymer system, linear and flexible diblock copolymer A-B melts with nearly equal statistical segment lengths, are simple and have been well understood[1], adding just one more flexible block C greatly expands the parameter space and leads to many distinct morphologies such that the phase behavior of flexible ABC triblock terpolymer melts remains poorly understood, despite the large amount of efforts devoted; this is the case for both linear and miktoarm (or star) chain architectures.[1, 3-7]

In this work, we are mainly interested in the various 2D tiling patterns formed by ABC miktoarm triblock terpolymer melts (referred to as stars hereafter), which are unique due to their underlying chain architecture and tendency to form morphologies rarely found in other block copolymer systems. The tiling patterns, whose structures consist of cylinders with even-sided polygonal cross-sections arranged so as to periodically tile the plane, can form when the three arms have comparable block lengths; such arrangements force the star junctions to align themselves along 1D lines (either straight or curved) rather than 2D surfaces.[8, 9] Each pattern is referred to by a set of integers enclosed in brackets that denote the polygons meeting at a vertex; for example, the well-known honeycomb tiling is referred to as [6.6.6] or [6^3] as it contains one type of vertex where three hexagons meet. The tiling patterns can be further classified based on whether they correspond to one of eleven so-called Archimedean tilings, all of which have the

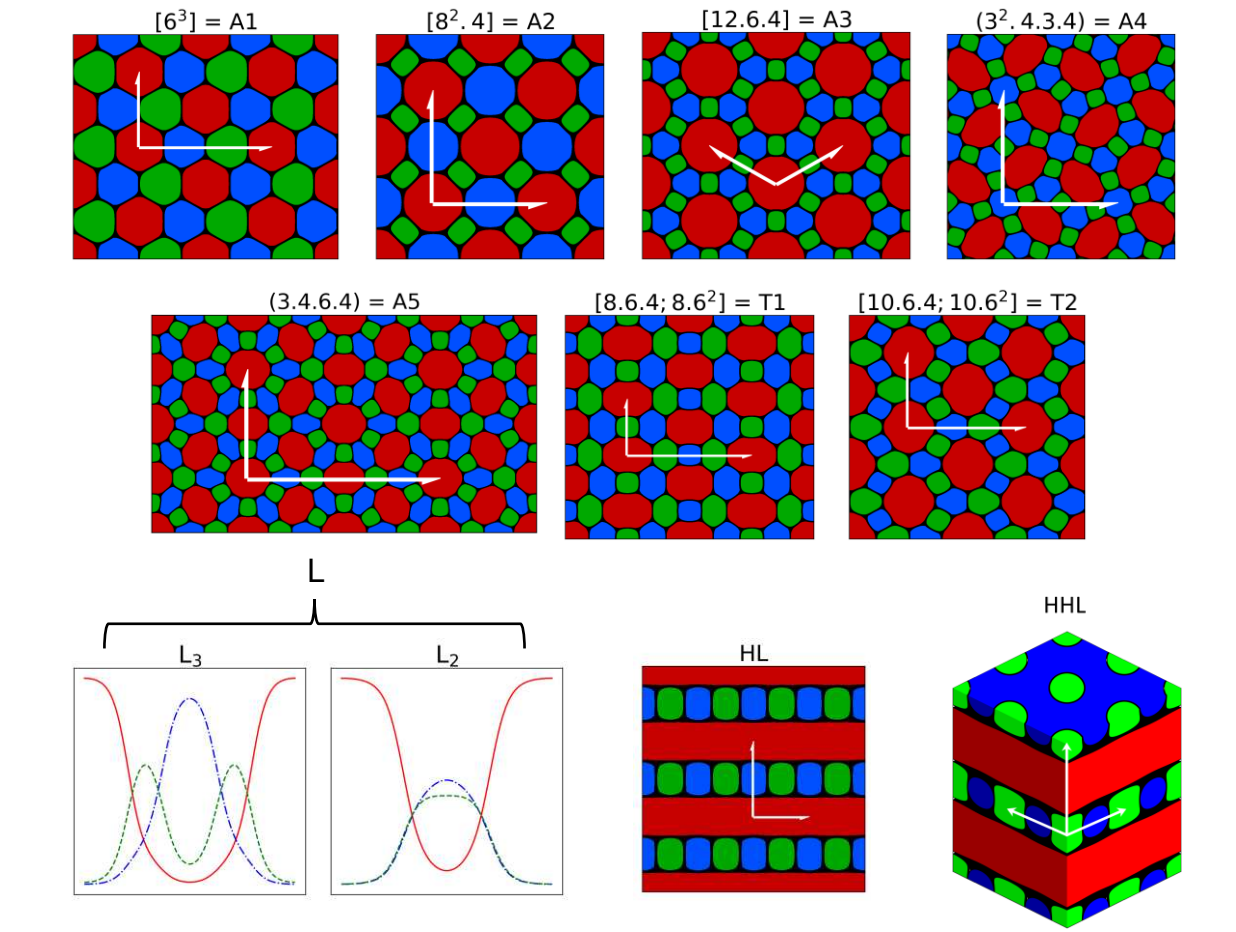

(a)

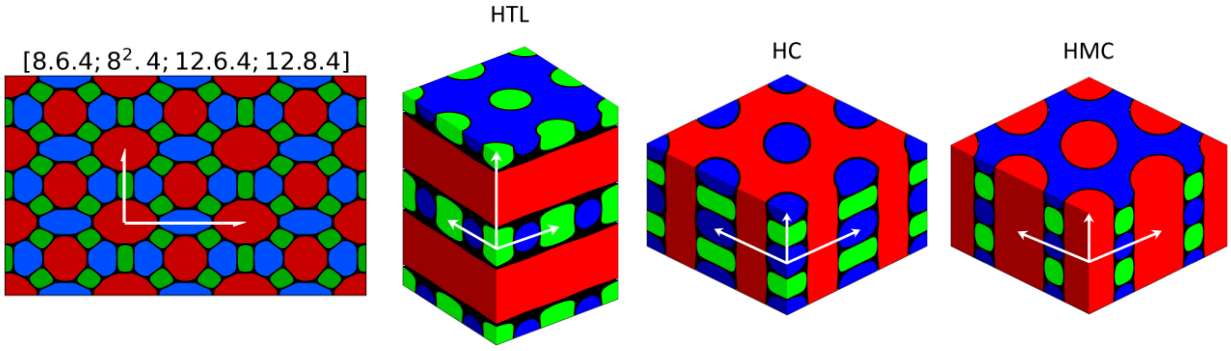

(b)

Figure 5.1. (Color) Schematics of some (a) stable and (b) unstable phases formed by symmetrically interacting ABC stars at χN=30, constructed from the volume-fraction fields $\{\phi_P(\mathbf{r})\}$ for P=A,B,C (L shows a direct plot of $\{\phi_P(\mathbf{r})\}$). Red, blue, and green correspond to regions where $\phi_P(\mathbf{r})$>0.5 for P=A,B,C, respectively, with other regions shown in black. The unit cells used in our SCF calculations are shown by white arrows indicating their basis vectors, and each phase is assigned a simple code name for convenience. See the main text for more details.

defining characteristic that they contain only one type of vertex. It is possible for tiling patterns to exist that have several types of vertex however (see Fig. 1), in which case each distinct set of polygons is separated by a semicolon. There are two exceptions to this naming scheme in this paper, [10.6.4;10.8.4] and [8.6.4;8.6^2;12.6.4], which contain several unique vertices while also having a corresponding Archimedean tiling that can be superimposed in a systematic manner. [10.6.4;10.8.4] can be seen to correspond to (3^2.4.3.4) by connecting the centers of the red (A-block) regions in Fig. 5.1, where we use parentheses rather than brackets to denote that the tiling is superimposed; similarly [8.6.4;8.6^2;12.6.4] can have (3.4.6.4) superimposed by connecting the centers of the blue (B-block) regions in Fig. 5.1.

While numerous tiling patterns (including those shown in Fig. 5.1(a)) have been found in experiments,[10, 11] our focus in this work is on the study of model, rather than real, melts of ABC stars. Accordingly, we give a brief overview of the previous theoretical and simulation studies of ABC stars having symmetric interactions (*i.e.*, equal repulsion) among segments on different arms, which are also the focus of our study. These studies assume that the three arms have the same statistical segment length and that all polymer segments occupy the same volume, thus providing a well-defined model system that avoids complications in experimental systems.

For the simplest case of ABC stars where the three arms have the same length, the [6^3] tiling pattern is expected from symmetry considerations and is indeed found by Dotera and Hatano[12] in their lattice Monte Carlo (LMC) simulations, by Bohbot-Raviv and Wang[13] in their numerical minimization of a free-energy functional obtained under the random-phase approximation for incompressible melts in a 2D unit cell, and by Liang and co-workers in their 2D[14] and 3D[15] calculations of a dynamic density-functional theory[16, 17].

Using the aforementioned LMC simulations at the polymer volume fraction $\phi \approx 0.75$ in rectangular cuboid boxes of various sizes, where the three arms of each star are connected to a common joint segment J with the nearest-neighbor interaction parameters $\varepsilon_{PP}=\varepsilon_{PJ}$ (for $\{P,P'\}=\{A,B,C\}$ and $P' \neq P$) and $\varepsilon_{PP}=\varepsilon_{JJ}=0$, Gemma *et al.* found various morphologies for stars having equal A- and B-arm length (*i.e.*, $N_A=N_B$) with increasing $\gamma \equiv N_C/N_A$, including five tiling patterns ([8^2.4], [6^3], [8.6.4;8.6^2], [10.6.4;10.6^2] and [12.6.4]), hierarchical lamellae (HL), hierarchical cylinders (HC), perforated lamellae (PL, *i.e.*, a variant of HL with A and B also penetrating into C-layers), A-B lamellae with oblate C-spheres at the A-B interfaces, and prolate spheres of A-B lamellae in C-matrix.[18] Table I lists the correspondence of various names used for the same morphology between our work and those in the literature; note that a "hierarchical" morphology is the same as the morphology (*e.g.*, lamellae, gyroid, and cylinders) formed by diblock copolymers but with one domain instead consisting of two microphase-separated domains whose interface is perpendicular to that in the morphology formed by diblock copolymers (if they are parallel, we have a "core-shell" morphology). They also studied [8^2.4], [6^3], [12.6.4] and HL using a strong-stretching theory.[18] In their subsequent simulations in a box of 128×128×10 (in units of the lattice spacing), Dotera and Gemma[19] found (3^2.4.3.4) for $A_9B_7C_{14}$ (where the subscripts denote the length of each block) and the dodecagonal quasicrystal (DDQC) tiling for $A_9B_7C_{16}$, and Dotera[20] found [8^2.4], DDQC, and [12.6.4] for $A_9B_7C_{12}$, $A_9B_7C_{15}$, and $A_9B_7C_{17}$ and $A_9B_7C_{18}$, respectively. Gemma *et al.* presented a final phase diagram that contains additional morphologies of single diamond and unknown network, as well as (3^2.4.3.4) found for $A_9B_7C_{14}$ in a simulation box of 48×48×25.[21] Very recently, using the same LMC simulations (except with $\varepsilon_{PJ}=0$) at $\phi \approx 0.9$ with simulated annealing, Li and co-workers found [8^2.4], [6^3], [8.6.4;8.6^2] and HL for stars having $N_A=N_B=6$ with increasing $N_C=2\sim15$.[22]

Table 5.1. Correspondence of various names used for the same self-assembled morphology formed by ABC stars.

Name used in this work	Other names used in the literature
two-layer lamellae (L_2)	P- and P′-segregated domains within L[23], L_3[35]
three-layer lamellae (L_3)	$L_{P,P'}$ with the minority block in the interfaces[23], LAM_3[27], L3[31], Lam[34, 44], L_3[35]
hierarchical lamellae (HL)	L+C[18, 22, 29, 44], C_P+$C_{P'}$ within L[23], LAM+BD[27], LPOC[34], $L_\perp$[35]
hierarchical-hexagonal lamellae (HHL)	HPL[34, 44]
hierarchical-tetragonal lamellae (HTL)	QPL[34], TPL[44]
hierarchical-checkerboard lamellae (HCL)	LAS[34]
hierarchical gyroid (HG)	$G_\perp$[35], HDG[44]
hierarchical cylinders (HC)	CPD[18], $SWM_{A,B}$ within C_{AB}^{hex}[23], HHC[31, 44], $C_\perp$ in the second row of their figure 4(a)[35]
hierarchical-matrix cylinders (HMC)	$C_\perp$ in the first row of their figure 4(a)[35]
core-shell gyroid (CSG)	gyroid with the minority block in the interfaces[23], Gyroid[34], DG[44]
core-shell cylinders (CSC)	CSH[27], HC[31, 44], HCyl[34]
core-shell spheres (CSS)	Bcc[34, 44], S_3[35]
perforated lamellae (PL)	perforated layer[18], C_A+C_B within PL_C[23]

Notably, in the range of γ=13/6~15/6, Gemma *et al.* found [10.6.4;10.6^2] and/or PL[18] while Li and co-workers found HL[22].

Using dissipative particle dynamics (DPD) simulations at the dimensionless polymer segment number density $\rho\sigma^3$=3 in a cubic box of size $(19\sigma)^3$, where σ denotes the range of the non-bonded DPD potential, Huang and co-workers presented two phase diagrams for stars having $N \equiv N_A+N_B+N_C=20$, where the three arms of each star are connected to a common joint segment J with the dimensionless DPD interaction parameters $a_{PP}=a_{PJ}=25$ and $a_{PP'}=a$. In the phase diagram at a=36 (for various star compositions), they found [8^2.4], [6^3], [10.6.4;10.6^2], (3^2.4.3.4), HL, two-layer lamellae (L_2), three-layer lamellae (L_3), core-shell gyroid (CSG), and tubes (cylinders) formed by mixed two minority blocks (HEX); while in the case of $N_A=N_B$ (for various N_C and a-values) they did not find (3^2.4.3.4), but found for the volume fraction of C

segments $f_C \equiv N_C/N \leq 0.5$ two additional morphologies of micelle-like structures with either the two major blocks or all the three blocks segregated, and for $f_C \geq 0.6$ several additional morphologies including PL, two variants of PL (one referred to as C_A+C_B within PL_{AB} and PL_C, and the other as A- and B-segregated domains within PL_{AB}, in their paper), segmented A- and B-wormlike micelles within either PL_{AB} or a 3D network, AB-formed micelles, and HC.[23] In the case of $N_A=N_B$, their γ-values at which [8^2.4], [6^3] and [10.6.4;10.6^2] are found are consistent with the LMC simulations[18], and that [8.6.4;8.6^2] is found in the LMC simulations (for f_C=0.429~0.467)[18, 22] but not in the DPD simulations[23] is apparently due to the small N-value used in the latter, where f_C can only be integer multiples of 0.1. Also, the star composition (f_A=0.3 and f_B=7/30) at which (3^2.4.3.4) is found in the LMC simulations[18] is close to that (f_A=0.3 and f_B=0.2) in the DPD simulations[23].

Given the differences in the above model systems and that the mismatch between the periodic boundary conditions imposed on the simulation boxes and the bulk periodicity of the self-assembled structures (which is not known in the simulations) can change the structures and their stability[24, 25], one can only expect qualitative agreement among the above simulation studies (which is indeed obtained). On the other hand, as we will discuss next, several groups have performed numerical calculations using the polymer self-consistent field (SCF) theory of the "standard" model (*i.e.*, incompressible melts of continuous Gaussian chains with the Dirac δ-function repulsions), where the bulk periodicity of an ordered phase can be readily found by minimizing the Helmholtz free-energy density with respect to the size and shape of the calculation cell. As we will see, the resulting SCF phase diagram depends on both the ordered phases included in the calculation and the accuracy of their dimensionless Helmholtz free energy per chain βf_c (which in turn depends on the spatial and/or chain-contour discretization) used to

construct the phase diagram, where $\beta \equiv 1/k_B T$ with k_B denoting the Boltzmann constant and T the thermodynamic temperature of the system.

Tang *et al.* performed 2D SCF calculations with a combinatorial screening strategy[26], where they solved the modified diffusion equations (MDEs) using a Crank-Nicholson scheme and the alternating direction implicit (CN-ADI) method with chain-contour discretization of Δs=0.01 and spatial discretization of $\Delta x = \Delta y = \left(\sqrt{6}/10\right) R_g$, where R_g denotes the root-mean-square radius of gyration of an ***ideal*** and ***linear*** chain having N segments.[27] They constructed a phase diagram for stars at $\chi_{PP'}N$=35, where $\chi_{PP'}$ denotes the Flory-Huggins parameter characterizing the repulsion between two segments of type P=A,B,C and P′≠P, as a function of f_A and f_B taken to be integer multiples of 0.1, which includes [6^3], [8^2.4], L_3, HL, HEX, core-shell cylinders (CSC), and the knitting pattern.[27] Qiu and co-workers also performed 2D SCF calculations, where they solved the MDEs using the generic reciprocal-space method[28] (which has no chain-contour discretization) with 151 basis functions (corresponding to spatial discretization of $\Delta x = D_x/18$ and $\Delta y = D_y/10$ with D_x and D_y denoting the bulk period of a self-assembled structure along the x- and y-direction, respectively, which are comparable to that used in Ref. 27).[29] They constructed a phase diagram for stars at $\chi_{PP'}N$=30, which includes [6^3], [8^2.4], [12.6.4], [8.6.4;8.6^2], [10.6.4;10.6^2], [8.6.4;8^2.4;12.6.4;12.8.4], L_3, and HL; while they used a much smaller increment of 0.001 in f_P, they focused only on the central portion (*i.e.*, f_P>0.2 for any P) of the phase diagram.[29] Apart from the different phases included in these calculations, the reciprocal-space method is expected to give more accurate results than the CN-ADI method.

Li and co-workers solved the MDEs using the 2nd-order pseudo-spectral method[30] with Δs=0.001 and a spatial discretization grid of 128^2 or 64^3 for a calculation cell containing one or

two unit cells of an ordered phase (such that the grid spacing is less than $0.1R_g$), and constructed a phase diagram for stars at $\chi_{PP'}N$=60, which includes [6^3], [8^2.4], [12.6.4], [8.6.4;8.6^2], [10.6.4;10.6^2], (3^2.4.3.4), L_3, HL, CSC, and HC; they also included (3.4.6.4) in their calculations but found it to be unstable.[31] The central portion of the phase diagram that Li and co-workers focused on is somewhat larger than in Ref. 29, and apart from the different phases included, their results are in good agreement in most cases. Note that the spatial discretization used in Ref. 31 is finer than in Ref. 29. In the case of f_B=f_C, [12.6.4] is stable for $0.513 \le f_A \le 0.566$ in Ref. 31 but unstable in Ref. 29; the stable regions of [6^3], [8^2.4] and [10.6.4;10.6^2] found in Ref. 31 are also larger than those in Ref. 29 (with the opposite occurring for [8.6.4;8.6^2]). These could be due to their different values of $\chi_{PP'}N$.

Zhang and co-workers solved the MDEs using a 4th-order pseudo-spectral method[32, 33] with $\Delta s \le 0.01$ and a spatial discretization grid of 32^3 for a unit cell, and constructed a phase diagram consisting of five lines connecting the central point at f_A=f_B=1/3 to those at f_C=0 and f_B=0, 0.17, 0.22, 0.33 and 0.5, respectively, for stars at $\chi_{PP'}N$=30, which includes [6^3], [8^2.4], [8.6.4;8.6^2], (3^2.4.3.4), L_3, HL, CSC, core-shell spheres (CSS), CSG, HEX, gyroid formed by mixed B and C, and hierarchical-tetragonal lamellae (HTL).[34] They actually included many more ordered structures in their calculations and found in particular [12.6.4], [10.6.4;10.6^2], (3.4.6.4), and [8.6.4;8^2.4;12.6.4;12.8.4] to be unstable along the five lines.[34] Their spatial discretization, however, may not be enough to give accurate results; in the case of two blocks having the same length, for example, Refs. 29 and 34 give quantitatively different phase boundaries even for the same phases included in both studies.

Finally, Qian and Xu solved the MDEs using the 2nd-order pseudo-spectral method[30] (with the chain-contour and spatial discretization not given but presumably the same as in Ref.

31), and constructed a phase diagram for stars at $\chi_{PP'}N$=60 in the case of f_B=f_C, which includes [6^3], [8^2.4], L_2, L_3, HL, HC, hierarchical-matrix cylinders (HMC), hierarchical gyroid (HG), and CSS.[35] The authors note that the stable region of HMC they found for 0.46<f_A<0.48 may actually be occupied by some tiling pattern not included in their calculations.[35]

The discrepancies between these previous SCF results raise the following question: What are the stable and unstable phases formed by this simple model system? Here we address this question by performing SCF calculations of the "standard" model for symmetrically interacting ABC stars at $\chi_{PP'}N \equiv \chi N$=30 (for P=A,B,C and P′≠P), focusing on the central portion (*i.e.*, $f_P \gtrsim 0.2$ for any P) of the phase diagram as this is the region occupied by the tiling patterns. By including all of the presently discovered tiling patterns from theories and experiments (overlapping many of the candidate pools of previous SCF studies) and accurately computing their free-energy density, we definitively establish which of these patterns are stable at the selected degree of segregation. Additionally, we investigate the energetic and entropic contributions to the free-energy density of the patterns in order to understand what drives their stability, focusing particularly on the differences between the lamellar-type phases (*i.e.*, L_2, L_3, HL, hierarchical-hexagonal lamellae (HHL), and HTL) and tiling patterns, as well as the thermodynamic and morphological properties of stable complex tiling patterns (*i.e.*, (3^2.4.3.4) and (3.4.6.4)).

5.2 Model and Method

5.2.1 Self-consistent field (SCF) equations for the "standard" model

As in Refs. 27, 29, 31, 34, 35, here we consider the "standard" model (*i.e.*, an incompressible melt of continuous Gaussian chains interacting via the Dirac δ-function potential) for n miktoarm star triblock terpolymer chains in volume V at thermodynamic temperature T. Each terpolymer chain (referred to as a star) consists of three linear blocks, denoted by P

(=A,B,C), connected at a common junction with each P block having N_P segments. For simplicity, we assume that all segments have the same volume $\rho_0^{-1} \equiv V/nN$ with $N \equiv \sum_P N_P$; the average volume fraction of P, equivalent to the block fraction, is therefore given by $f_P \equiv N_P/N$.

In the "standard" model, the configuration of the P-block in the k^{th} star is given by a continuous curve $\mathbf{R}_{k,P}(s)$ in space, where $s \in [0, f_P]$ is the block-contour variable with s=0 corresponding to the free end and f_P to the star junction. The dimensionless bonded energy of the P-block is then given by $\beta u_{k,P}^{b} = \int_0^{f_P} \mathrm{d}s \left(\mathrm{d}\mathbf{R}_{k,P}(s)/\mathrm{d}s \right)^2 \Big/ 4R_g^{\,2}$, where $\beta \equiv 1/k_B T$ with k_B denoting the Boltzmann constant, and $R_g \equiv \sqrt{N/6}a$ with a being the effective bond length assumed to be the same for all the blocks; note that $N \to \infty$ and $a \to 0$ while R_g is finite. On the other hand, the dimensionless non-bonded interaction energy (for stars with symmetric interactions) is given by $\beta U^{\text{nb}} = \left(\chi \rho_0 / 2 \right) \int \mathrm{d}\mathbf{r} \sum_P \sum_{P' \neq P} \hat{\phi}_P(\mathbf{r}) \hat{\phi}_{P'}(\mathbf{r})$, where χ denotes the Flory-Huggins parameter characterizing the repulsion between two segments of different types and $\hat{\phi}_P(\mathbf{r}) \equiv \left(N/\rho_0 \right) \sum_{k=1}^{n} \int_0^{f_P} \mathrm{d}s \, \delta\left(\mathbf{r} - \mathbf{R}_{k,P}(s) \right)$ denotes the normalized microscopic number density of P-segments at spatial position $\mathbf{r}$. The canonical partition function of this model system can therefore be written as

$$Z = \frac{1}{n!} \int \prod_{k=1}^{n} \prod_P \mathrm{D}\mathbf{R}_{k,P} \cdot \exp\left(-\sum_{k=1}^{n} \sum_P \beta u_{k,P}^{b} - \beta U^{\text{nb}} \right) \prod_{\mathbf{r}} \delta\left(\sum_P \hat{\phi}_P(\mathbf{r}) - 1 \right)$$
$$\cdot \prod_{k=1}^{n} \delta\left(\mathbf{R}_{k,A}(f_A) - \mathbf{R}_{k,B}(f_B) \right) \delta\left(\mathbf{R}_{k,B}(f_B) - \mathbf{R}_{k,C}(f_C) \right),$$

where the first Dirac δ-function enforces the incompressibility constraint at $\mathbf{r}$ while the others enforce the star chain architecture.

The SCF equations for the above model are given by

$$\omega_P(\mathbf{r}) = \chi N \sum_{P' \neq P} \phi_{P'}(\mathbf{r}) + \eta(\mathbf{r}), \tag{5.1}$$

$$\phi_{\mathrm{P}}(\mathbf{r}) = \frac{1}{Q}\int_0^{f_{\mathrm{P}}} \mathrm{d}s\, q_{\mathrm{P}}(\mathbf{r},s) q_{\mathrm{P}}^{\dagger}(\mathbf{r},s)\,, \tag{5.2}$$

$$\sum_{\mathrm{P}} \phi_{\mathrm{P}}(\mathbf{r}) = 1, \tag{5.3}$$

where $\phi_{\mathrm{P}}(\mathbf{r})$ is the normalized number density (*i.e.*, volume fraction) field of P-segments constrained to $\hat{\phi}_{\mathrm{P}}(\mathbf{r})$, $\omega_{\mathrm{P}}(\mathbf{r})$ is the conjugate field imposing this constraint, and $\eta(\mathbf{r})$ is the conjugate field imposing the incompressibility constraint at $\mathbf{r}$. $q_{\mathrm{P}}(\mathbf{r},s)$ and $q_{\mathrm{P}}^{\dagger}(\mathbf{r},s)$ are the forward and backward one-end-integrated propagators for the P-block, satisfying the modified diffusion equations (MDEs)

$$\frac{\partial q_{\mathrm{P}}}{\partial s} = \nabla^2 q_{\mathrm{P}} - \omega_{\mathrm{P}}(\mathbf{r}) q_{\mathrm{P}} \tag{5.4}$$

with the initial condition of $q_{\mathrm{P}}(\mathbf{r},s=0)=1$ and

$$-\frac{\partial q_{\mathrm{P}}^{\dagger}}{\partial s} = \nabla^2 q_{\mathrm{P}}^{\dagger} - \omega_{\mathrm{P}}(\mathbf{r}) q_{\mathrm{P}}^{\dagger} \tag{5.5}$$

with the initial condition of $q_{\mathrm{P}}^{\dagger}(\mathbf{r}, s = f_{\mathrm{P}}) = \prod_{\mathrm{P}'\neq\mathrm{P}} q_{\mathrm{P}'}(\mathbf{r}, f_{\mathrm{P}'})$, respectively.

$$Q = \frac{1}{V}\int \mathrm{d}\mathbf{r}\, q_{\mathrm{P}}(\mathbf{r},s) q_{\mathrm{P}}^{\dagger}(\mathbf{r},s) \tag{5.6}$$

is the normalized single-star partition function; note that Q is independent of P and s, and we have taken R_g as the unit of length in Eqs. (5.1)~(5.5). After these equations are solved, the dimensionless mean-field Helmholtz free energy per star can be calculated (within a constant) as

$$\beta f_c = \frac{\chi N}{2V}\int \mathrm{d}\mathbf{r} \sum_{\mathrm{P}} \sum_{\mathrm{P}'\neq\mathrm{P}} \phi_{\mathrm{P}}(\mathbf{r})\phi_{\mathrm{P}'}(\mathbf{r}) - \frac{1}{V}\int \mathrm{d}\mathbf{r} \sum_{\mathrm{P}} \omega_{\mathrm{P}}(\mathbf{r})\phi_{\mathrm{P}}(\mathbf{r}) - \ln Q\,, \tag{5.7}$$

which must be minimized with respect to (up to six) unit cell parameters $\boldsymbol{\theta}$ for each ordered phase to find its bulk periodicity; for the "standard" model, this gives[36]

$$\frac{\partial Q}{\partial \boldsymbol{\theta}} = \mathbf{0}\,. \tag{5.8}$$

5.2.2 Numerical methods and calculated quantities

For a given set of model parameters $\{f_{\mathrm{P}}\}$ and χN, discretization parameters $n_{\mathbf{r}}$ and n_s (explained in Sec. 3.1 below), and initial guess $\mathbf{x}^{(0)} \equiv \{\boldsymbol{\theta}^{(0)}, \{\omega_{\mathrm{P}}^{(0)}(\mathbf{r})\}\}$ for an ordered phase, we solve the above SCF equations using the recently released C++/Cuda version[37] of PSCF[38], an open-source code for SCF calculations of the "standard" model for block copolymer self-assembly that takes advantage of the massive parallelization provided by Graphics Processing Units (GPUs)[39]. PSCF uses a 4th-order pseudo-spectral method[40] to solve Eqs. (5.4) and (5.5), the composite Simpson's (1/3) rule to evaluate the contour integral in Eq.5.2, the composite trapezoidal rule to evaluate the integral over $\mathbf{r}$ in Eq. (5.6), and the Anderson mixing[41] combined with a variable-cell scheme[42] to simultaneously solve Eqs. (5.1), (5.3) and (5.8), which can be re-written as $\mathbf{f}(\mathbf{x})=\mathbf{0}$ with the convergence criterion of $|\mathbf{f}|_{\max}<\varepsilon$ (our choice of ε is also given in Sec. 3.1 below). As our improvement of PSCF, we have implemented the option to control the order of the Richardson extrapolation K that is used in solving the MDEs and evaluating the chain-contour integral in Eq.5.2.

After solving the above SCF equations, we further calculate the dimensionless mean-field internal energy per star $\beta u_c = \sum_{\mathrm{P}} \sum_{\mathrm{P}' \neq \mathrm{P}} \beta u_{c,\mathrm{PP}'} / 2$ with $\beta u_{c,\mathrm{PP}'} = \chi N \int \mathrm{d}\mathbf{r}\, \phi_{\mathrm{P}}(\mathbf{r}) \phi_{\mathrm{P}'}(\mathbf{r}) / V$ being the contribution due to the P-P′ repulsion, and the dimensionless entropy per star $s_c / k_B = \sum_{\mathrm{P}} s_{c,\mathrm{P}} / k_B + s_{c,\mathrm{J}} / k_B$ with $s_{c,\mathrm{P}} / k_B \equiv \int \mathrm{d}\mathbf{r} \left(\omega_{\mathrm{P}}(\mathbf{r}) \phi_{\mathrm{P}}(\mathbf{r}) + \rho_{\mathrm{J}}(\mathbf{r}) \ln q_{\mathrm{P}}(\mathbf{r}, f_{\mathrm{P}}) \right) / V$ due to the conformational entropy of the P-block and $s_{c,\mathrm{J}} / k_B \equiv -\int \mathrm{d}\mathbf{r}\, \rho_{\mathrm{J}}(\mathbf{r}) \ln \rho_{\mathrm{J}}(\mathbf{r}) / V$ due to the translational entropy of the junction, where $\rho_{\mathrm{J}}(\mathbf{r}) \equiv \prod_{\mathrm{P}} q_{\mathrm{P}}(\mathbf{r}, f_{\mathrm{P}}) / Q$ is the normalized number

density of junctions satisfying $\int d\mathbf{r}\rho_J(\mathbf{r}) = V$;[43] clearly, $\beta f_c = \beta u_c - s_c/k_B$.

5.3 Results and Discussion

The phases known to play a significant role in symmetrically interacting ABC stars are well-established,[29, 31, 34] and here we primarily seek to determine which tiling patterns are stable using the polymer self-consistent field (SCF) calculations of the "standard" model. Consequently, we consider as candidate phases all regular tiling patterns known from past studies, both theoretical and experimental, as well as several lamellar-type phases (in order to compute their phase boundaries with the tiling patterns). This includes all the phases shown in Fig. 1, in addition to the 2D knitting pattern[27] and the 3D hierarchical-checkerboard lamellae (HCL, referred to as LAS in Ref. 34) that is similar to the hierarchical-tetragonal lamellae (HTL) but with both minority blocks arranged in a checkerboard pattern; we were able to obtain converged results of the knitting pattern and HCL only at a few points in the $\{f_P\}$ parameter space. Though this list is not exhaustive, it includes many phases known from previous work to form near the central region of the phase diagram and importantly overlaps with the candidate pools of previous studies, thus resolving the discrepancies that may have arisen from using different candidates in previous SCF calculations.

In the remainder of this section, we first describe the impact of numerical parameters and justify that our choices give sufficient numerical accuracy in Sec. 5.3.1. This is followed in Sec. 5.3.2 by a presentation of the phase diagram at the segregation strength χN=30, as well as the dimensionless Helmholtz free energy per star βf_c and its components along the f_B=f_C isopleth. Sec. 3.3 finishes with an investigation of the thermodynamic properties of stable complex tiling patterns (3^2.4.3.4) and (3.4.6.4), uncovering the effects that stabilize them and comparing these amongst various morphologies; the star junction density $\rho_J(\mathbf{r})$ of (3^2.4.3.4) is also presented.

5.3.1 Numerical accuracy

For a given set of system parameters $\{f_P\}$ and χN, there are four numerical parameters that control the accuracy of our SCF calculations of an ordered phase: the maximum absolute value of the residual errors of the converged SCF equations (*i.e.*, the convergence criterion) ε, the total number of spatial discretization points $n_{\mathbf{r}}$, the total number of chain-contour discretization intervals $n_s = \sum_P n_P$, and the order of the Richardson extrapolation K that is used to solve the modified diffusion equations. Outside of the error analysis in this section, we set $\varepsilon=10^{-5}$ and allow PSCF[37] to adjust the unit-cell parameters in order to minimize βf_c for all of our results presented. For the error analysis, the unit-cell parameters are held constant (very close to those minimizing βf_c) so as to examine solely the effect of the numerical parameters on accuracy of βf_c of an ordered phase. In practice, we find the differences in βf_c between different phases to always be greater than our choice of $\varepsilon=10^{-5}$, allowing the stable phase (of those considered) at each point in the system parameter space to be resolved unambiguously, provided that $n_{\mathbf{r}}$ and n_s are large enough to also give an accuracy of $\beta f_c=\beta f_c(n_{\mathbf{r}},n_s,K)$ higher than 10^{-5}. Note that the parameter K affects both the accuracy of βf_c and the accessible points in the $\{f_P\}$ parameter space and should thus be chosen carefully. As discussed in The block-contour discretization n_P is constrained to integer multiples of 2^K; since the block fraction $f_P=n_P/n_s$, this also constrains the values that $\{f_P\}$ can take for given n_s. With this in mind, $K=1$ (*i.e.*, the 4th-order pseudo-spectral method[40] implemented in PSCF) is used to obtain all subsequent results while higher-order (*i.e.*, $K>1$) methods are used only to obtain highly accurate values of βf_c, denoted by $\beta f_c^* \equiv \beta f_c(n_{\mathbf{r}}^{\max}, n_s^{\max}, K^{\max})$, for use in the error analysis. The error in $\beta f_c=\beta f_c(n_{\mathbf{r}},n_s,1)$ of an ordered phase is then measured by $\Delta(n_{\mathbf{r}}, n_s) \equiv \left| \beta f_c(n_{\mathbf{r}}, n_s, 1) - \beta f_c^* \right|$. This error must be analyzed

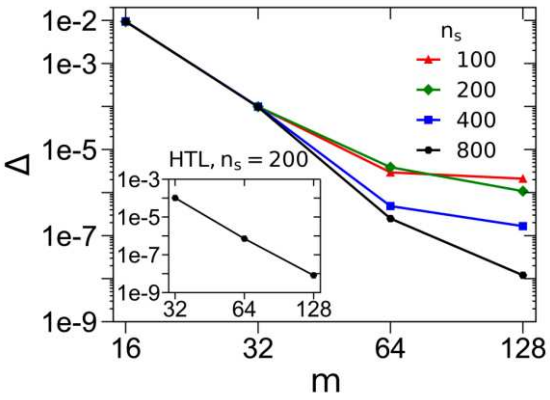

Figure 5.2. Logarithmic plot of the error $\Delta \equiv \left|\beta f_c(m, n_s, K=1) - \beta f_c^*\right|$ in the SCF Helmholtz free energy per star βf_c as a function of the spatial discretization parameter m and the chain-contour discretization parameter n_s for (3^2.4.3.4) and HTL (inset). Results for (3^2.4.3.4) are shown at the ABC star composition (f_A=0.45, f_B=0.30) and for HTL at (f_A=0.50, f_B=0.30), both at χN=30. A square mesh of $n_\mathbf{r}=m^2$ and cubic mesh of $n_\mathbf{r}=m^3$ is used for (3^2.4.3.4) and HTL, respectively, with $\beta f_c^* = \beta f_c(m=256, n_s=1600, K=4)$ for (3^2.4.3.4) and $\beta f_c^* = \beta f_c(m=128, n_s=800, K=3)$ for HTL; the convergence criterion of $\varepsilon=10^{-9}$ for solving the SCF equations is used in both cases. In units of R_g, the unit-cell parameters are 8.41 for (3^2.4.3.4) and (3.48,3.98) for HTL. See the main text for more details.

for each ordered phase, particularly with respect to its variation with $n_\mathbf{r}$ and n_s as the values necessary to achieve a desired accuracy depends on the complexity of the phase, the size of its unit cell, and the segregation strength χN (which is set to 30 in this work).

For example, Fig. 2 and its inset show $\Delta(n_\mathbf{r}, n_s)$ for (3^2.4.3.4) and HTL, respectively, serving as representative results for 2D and 3D phases. Rather than $n_\mathbf{r}$, the horizontal axis m denotes the number of spatial discretization intervals along each direction of the unit cell – note that a square unit cell is used for (3^2.4.3.4) and a tetragonal unit cell for HTL. We see in Fig. 2 that for small m Δ-curves for various n_s overlap as the errors are dominated by the spatial discretization, while for large m Δ-curves begin to level off as the errors are now dominated by the chain-contour discretization. From these results, it is clear that n_s=200 is sufficient to yield $\Delta<10^{-5}$ for both (3^2.4.3.4) and HTL by taking m=128 for the former and m=64 for the latter. In fact, this n_s-value

is sufficient to give $\Delta<10^{-5}$ for all phases considered in this work and has the additional benefit that (with K=1) all accessible f_P-values are integer multiples of 0.01, providing a high-resolution discretization of the parameter space. For this reason, n_s=200 is used in our subsequent SCF calculations. The effect of $n_{\mathbf{r}}$ on Δ for all other phases is also studied in a similar manner, and we find that $n_{\mathbf{r}}$=128×256, 128^2, 128^2, 128×256, 128×288, 160×240, 128, 160×192, and 64^3 for [6^3], [8^2.4], [12.6.4], (3.4.6.4), [8.6.4;8.6^2], [10.6.4;10.6^2], lamellae (L), HL, and all 3D phases, respectively, ensure $\Delta<10^{-5}$ in all cases; these are used to construct the phase diagram in Sec. 3.2.

5.3.2 Phase diagram and free-energy data

To construct the phase diagram at χN=30, βf_c is computed for all competing phases at each accessible point in the central region of the $\{f_P\}$ parameter space, and the phase having the smallest βf_c is taken as the stable one at that point. The results are shown in Fig. 5.3, where the different stable phases are shown in different colors. The symmetry-reduced phase triangle (where calculations are carried out) is given in Fig. 5.3(a), where $f_A>f_B>f_C$ at all points except for the $f_B=f_C$ isopleth that forms the hypotenuse and the $f_A=f_B$ isopleth that bounds the triangle to the right. Note that the central region of the parameter space where tiling patterns are stable is enclosed by L in our SCF calculations.

Fig. 5.3 shows that there are a total of seven stable tiling patterns at χN=30, including [12.6.4], (3^2.4.3.4), (3.4.6.4), [8.6.4;8.6^2], and [10.6.4;10.6^2] in addition to the well-established [6^3] and [8^2.4]. The tiling patterns transition to lamellae (L) as one progresses radially outward in the phase diagram. We note that L occurs in two variations: L_3, where there exist three microphase-separated layers each mainly consisting of one species, and L_2, where the two minority (B and C) blocks mix to form a layer between those of the majority (A) block. Though no distinction is made between these two morphologies in Fig. 5.3, we have found that L_2 forms

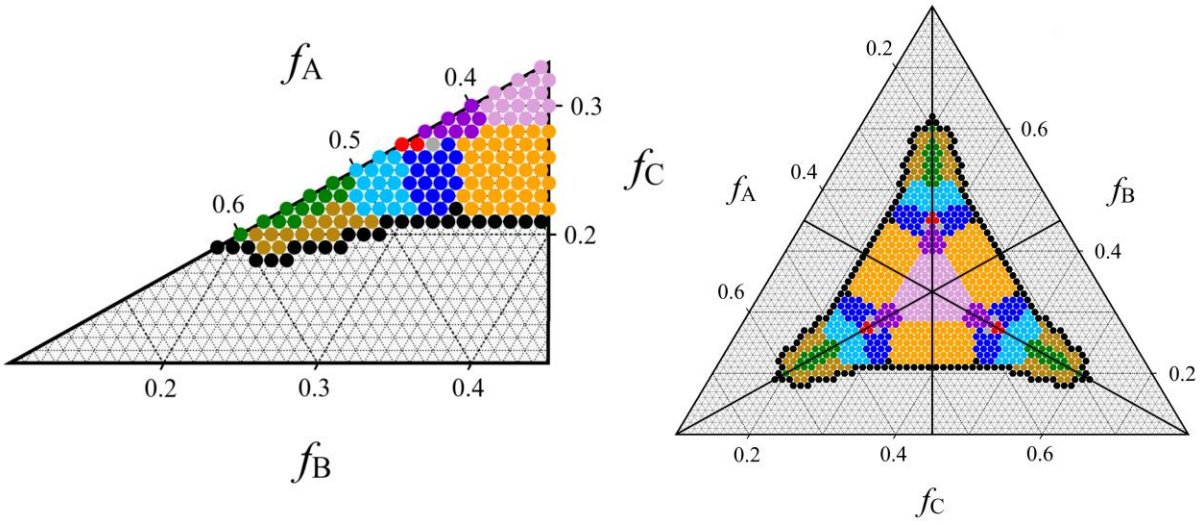

(a) (b)

Figure 5.3. (Color) Central region of our SCF phase diagram of ABC stars with symmetric interactions at χN=30. Each dot shows the stable phase at that point, color-coded according to [6^3] – pink, [8^2.4] – orange, [12.6.4] – cyan, (3^2.4.3.4) – blue, (3.4.6.4) – grey, [8.6.4;8.6^2] – purple, [10.6.4;10.6^2] – red, L – black, HL – green, and HHL – brown. Symmetric interactions reduce the necessary area to 1/6 of the parameter space as shown in Part (a), which is used to reconstruct the full phase diagram in (b). K=1 and n_s=200 are used in our SCF calculations. See the main text for more details.

when both f_B and f_C are small and comparable to each other, while L_3 forms when they are significantly different; for example, in Fig. 3(a) L_2 occurs near the f_B=f_C isopleth while L_3 occurs near the f_A=f_B isopleth. As the minority blocks become smaller and their size disparity decreases, trial (*i.e.*, initial) fields for L_3 converge instead to L_2 in our SCF calculations, the stability of which is probably due to either the relatively weak segregation of χN=30 considered here or the limited pool of candidate phases (which does not include, for example, the perforated lamellae found in molecular simulations[1823]). SCF calculations at a stronger segregation of χN=60 by Li *et al.*[31] suggest that the stability of L shrinks dramatically as χN increases, most likely from the destabilization of L_2 relative to other morphologies.

The most novel of these results are the regions of stability of (3.4.6.4) and hierarchical-

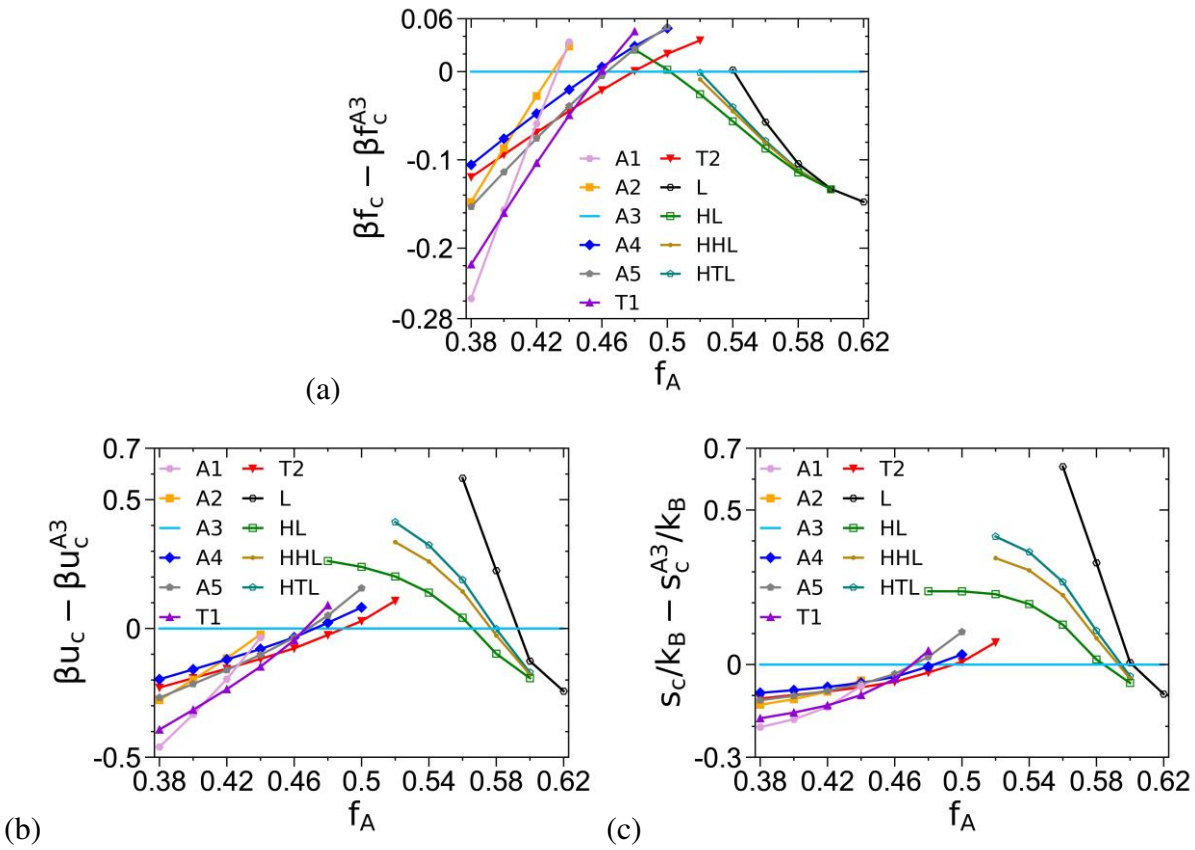

Figure 5.4. The dimensionless (a) Helmholtz free energy per star βf_c, (b) internal energy per star βu_c, and (c) entropy per star s_c/k_B along the f_B=f_C isopleth at χN=30 for various tiling patterns (including A1=[6^3], A2=[8^2.4], A3=[12.6.4], A4=(3^2.4.3.4), A5=(3.4.6.4), T1=[8.6.4;8.6^2], and T2=[10.6.4;10.6^2]) and lamellar-type phases. All values are taken relative to A3. See the main text for more details.

hexagonal lamellae (HHL). This is the first time these phases have been found stable in ABC stars with symmetric interactions, although both have been considered in previous SCF studies[31, 34] of these systems and HHL has been found stable for stars with asymmetric interactions.[44] With the parameter-space discretization used here, (3.4.6.4) is stable at a single point (f_A=0.44, f_B=0.29) with its βf_c on the order of 10^{-3} smaller than the competing tiling patterns (*i.e.*, (3^2.4.3.4), [10.6.4;10.6^2], and [8.6.4;8.6^2]). To the best of our knowledge, HHL has been considered in only one SCF study of symmetrically interacting ABC stars[34] where HTL was reported as stable

instead. In contrast to that study, we find that HHL is always more stable than HTL in the region considered here, with βf_c of HHL on the order of 10^{-3} smaller than HTL in most cases. According to our SCF calculations, HHL is the only stable 3D phase that appears in this region as hierarchical cylinders (HC), hierarchical-matrix cylinders (HMC), and HCL have either prohibitively large βf_c or simply could not be converged on at any of the points considered. Notably, HMC is not stable in the region of $0.46<f_C<0.48$ as found in Ref. 35, since [10.6.4;10.6^2] holds a small region of stability here. It is possible, however, that HC, HMC, or HCL could appear outside of the region of parameter space considered here. HC, for example, is most likely stable along the $f_B=f_C$ isopleth for larger values of f_A as we observe a downward trend in its βf_c along this line (data not shown); it is less likely that HMC or HCL is stable at any point for a symmetrically interacting system owing to the observed trend in their βf_c as well as the difficulty in obtaining converged results for these phases.

As discussed in the Introduction, there exist several previous SCF studies of this system at χN=30 that contain conflicting results, even for the same candidate phases considered. In particular, Ref. 34 found [12.6.4], [10.6.4;10.6^2], [8.6.4;8^2.4;12.6.4;12.8.4], (3.4.6.4), and HHL to be unstable along the five lines connecting the center of the $\{f_P\}$ parameter space to an edge of the phase triangle, while Ref. 29 found the former three tiling patterns to be stable at χN=30 and Ref. 31 found the former two (but not [8.6.4;8^2.4;12.6.4;12.8.4]) to be stable at χN=60. Meanwhile, both Refs. 31 and 34 found (3^2.4.3.4) to be stable although its region of stability is presented as much larger at χN=30 in Ref. 34 than at χN=60 in Ref. 31, while this phase was not considered in Ref. 29. In addition to these differences in phase stability, Refs. 29 and 34 (both at χN=30) also gave quantitatively different phase boundaries for the same phases – taking the $f_A=f_B$ isopleth as an example, Ref. 29 found the [8^2.4]/[6^3] and [6^3]/[8.6.4;8.6^2] transitions to

occur at f_C=0.28 and f_C=0.39, respectively, while Ref. 34 found these same phase transitions at f_C=0.265 and f_C=0.41, respectively. Clearly, such discrepancies raise questions concerning the accuracy and reproducibility of these previous SCF results, which we have addressed with the error analysis in Fig. 2 and thorough SCF calculations in Fig. 3. Our results definitively show that [12.6.4], [10.6.4;10.6^2], and (3.4.6.4) are stable tiling patterns at χN=30 and confirm the stability of (3^2.4.3.4), although its region is smaller than that given in Ref. 34 owing to the stability of [12.6.4]. Additionally, we have found [8.6.4;8^2.4;12.6.4;12.8.4] to be an unstable tiling pattern at all accessible points in the central region of parameter space considered here.

It is interesting to note that our SCF phase diagram qualitatively agrees well with that computed at χN=60[31] with the exception of (3.4.6.4) and HHL, which were found to be unstable and not considered, respectively; it is possible that (3.4.6.4) was missed in Ref. 31 as it occupies a small region of parameter space, or it may simply become unstable at the stronger segregation. Otherwise, it appears that the phase diagrams at χN=30 and χN=60 are similar, with the stronger segregation primarily causing phase boundaries to shift outwards along the isopleths. For example, along the f_B=f_C isopleth we find hierarchical lamellae (HL) to be stable for $f_A \in$[0.52,0.60]; for larger f_A the minority blocks become small enough to allow mixing and thus form L_2. At χN=60, however, HL is stable for $f_A \in$[0.566,0.768] while L_3 is reduced to a region centered on the f_A=f_B isopleth.[31] Despite this, the phase boundaries of [6^3], [8^2.4], [8.6.4;8.6^2], and [10.6.4;10.6^2] remain relatively unchanged, shifting only minorly at χN=60 while [12.6.4] replaces HL for $f_A \in$[0.513,0.566]. In particular, along the f_B=f_C isopleth we find the transition points (*i.e.*, f_A values) between [8^2.4]/[6^3], [6^3]/[8.6.4;8.6^2], [8.6.4;8.6^2]/[10.6.4;10.6^2], and [10.6.4;10.6^2]/[12.6.4] to lie in-between [0.28,0.29], [0.39,0.40], [0.44,0.45], and [0.46,0.47], respectively, with the corresponding transitions at χN=60 given by f_A=0.267, 0.410, 0.457, and

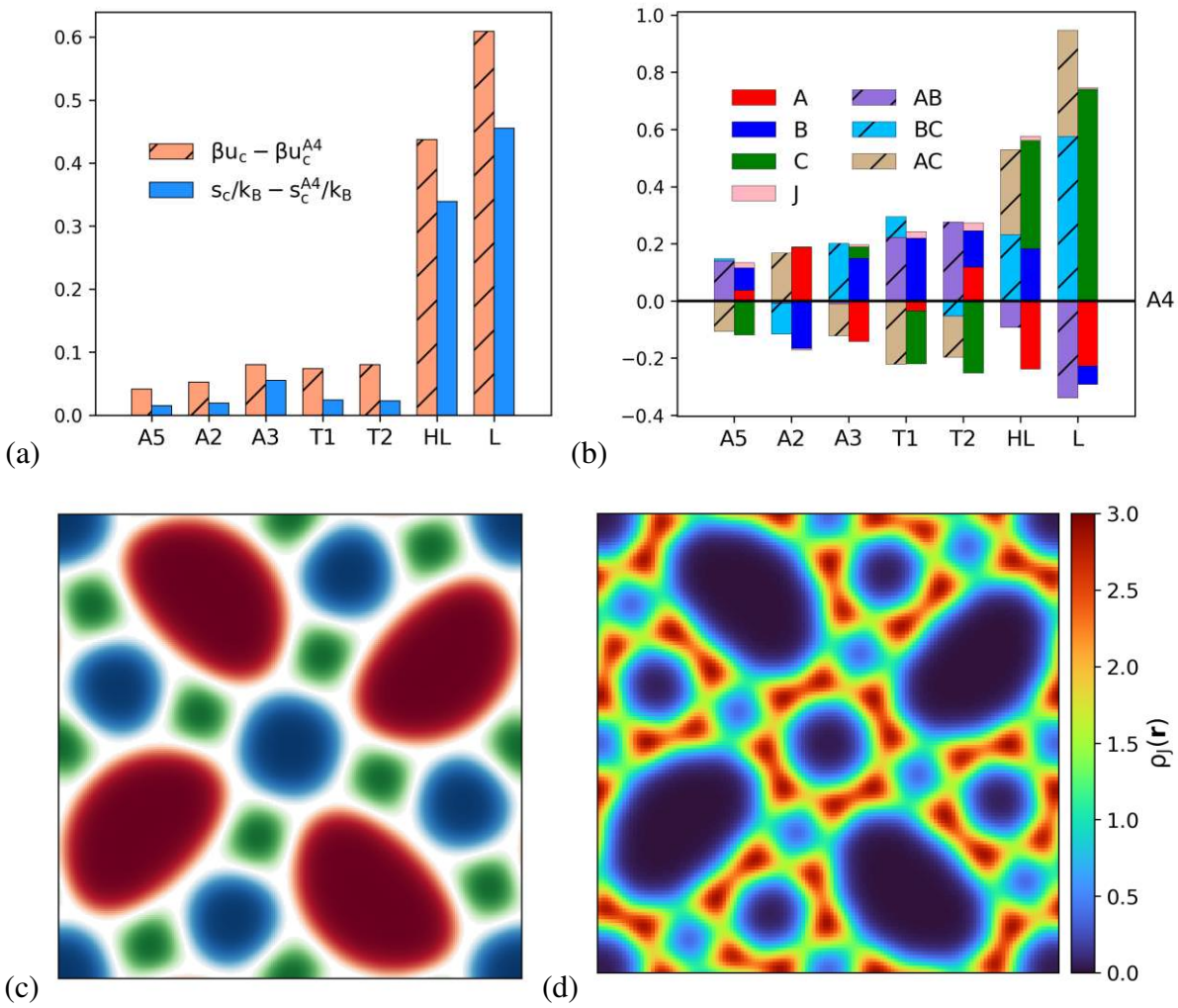

Figure 5.5. (Color) (a) The dimensionless internal energy per star βu_c and the dimensionless entropy per star s_c/k_B and (b) various contributions to βu_c (shown as the striped bars) and to s_c/k_B (shown as the solid bars) of A2=[8^2.4], A3=[12.6.4], A5=(3.4.6.4), T1=[8.6.4;8.6^2], T2=[10.6.4;10.6^2], HL, and L relative to A4=(3^2.4.3.4) at χN=30 and (f_A=0.45, f_B=0.30). Part (c) shows a unit cell of A4, where $\{\phi_P(\mathbf{r})\}$ smoothly transition from white at $\phi_P(\mathbf{r})$=0.50 to red, blue, and green at $\phi_P(\mathbf{r})$=1.0 for A, B, and C, respectively, thus allowing the interfaces to be resolved as the white regions; the corresponding star-junction density $\rho_J(\mathbf{r})$ is shown in (d). See the main text for more details.

0.513, respectively.[31] This leads to the conclusion that the central region of parameter space is relatively invariant to χN, with the regions of the interior tiling patterns (*i.e.*, [6^3], [8.6.4;8.6^2],

and [10.6.4;10.6^2]) changing changing little while [8^2.4], [12.6.4], and (3^2.4.3.4) occupy slightly larger regions at χN=60 and the region of HL increases significantly.

To support our results in Fig. 5.3 and better compare with other work, the differences in βf_c among various tiling patterns and lamellar-type phases (*i.e.*, L, HL, HHL, and HTL) along the f_B=f_C isopleth are shown in Fig. 4(a) as well as those in the dimensionless internal energy per star βu_c and the dimensionless entropy per star s_c/k_B in Figs. 4(b) and 4(c), respectively. Along this line the star composition is specified by a single block fraction, f_A, and all the differences in βf_c are taken relative to [12.6.4] rather than the disordered phase so as to highlight their magnitude, which is generally on the order of 10^{-2} for competing phases, except near phase boundaries where it can be on the order of 10^{-3} and rarely 10^{-4} (*e.g.*, at f_A=0.6). There is a general transition from tiling patterns (for $f_A \leq 0.5$) to lamellar-type phases ($f_A > 0.5$) along the isopleth, and we note that [12.6.4] is found to be slightly more stable than [10.6.4;10.6^2] and HL at two points given by f_A=0.48 and f_A=0.50, respectively.

From Figs. 5.4(b) and 5.4(c), we see that βu_c and s_c/k_B of the tiling patterns increase concomitantly with increasing f_A while those of the lamellar-type phases decrease in such a way that they become more stable than the tilings; in other words, the titling patterns are stabilized (for $f_A \lesssim 0.5$) by βu_c while the lamellar-type phases are stabilized (for $f_A \gtrsim 0.5$) by s_c/k_B. By visually inspecting the morphologies along the isopleth, we find that this effect can be ascribed to the mixing of the minority blocks that occurs in the tiling patterns for larger f_A. This phenomenon is entropically favorable but also incurs energetic penalty, generally large enough to outweigh the entropic gain and result in βf_c larger than the lamellar-type phases for $f_A \gtrsim 0.5$ (which can still maintain three distinct microphase-separated domains at the same f_A). Larger χN would make

such mixing more unfavorable and thus favor the tiling patterns as they consistently attain smaller βu_c than the lamellar-type phases. Consequently, if stability at stronger segregations is dominated by energetic effects rather than entropic effects, this could explain the larger region occupied by [12.6.4] along the isopleth at χN=60 in Ref. 31. We can see from Fig. 5.4(b) that [12.6.4] has the smallest βu_c for $f_A \in$[0.50,0.56], which nearly overlaps with $f_A \in$[0.513,0.566] where [12.6.4] is found to be stable at χN=60[31].

Similar results (data not shown) are found for the case of $f_B > f_C$ (but still within the central portion of the phase diagram), where [8^2.4], (3^2.4.3.4), (3.4.6.4) and [12.6.4] become stable for $f_A \lesssim 0.5$ while HHL becomes stable for $f_A \gtrsim 0.5$.

5.3.3 Thermodynamic and morphological properties of complex tiling patterns

Among the tiling patterns formed by ABC stars, (3^2.4.3.4) and (3.4.6.4) have no direct Archimedean tiling but rather a superimposed one; the unit cells of these stable phases are larger and more complex than any other tiling patterns in this system, resulting in an intriguing morphological structure that raises questions concerning the mechanisms behind their stability. Though (3.4.6.4) occupies only a small region of the phase diagram, (3^2.4.3.4) is quite prominent in this system and is particularly interesting for a number of reasons. It is an example of a cylindrical Frank-Kasper σ phase, having a structure equivalent to the cross-section of the spherical σ phase found stable in conformationally asymmetric diblock copolymer melts[45]. It is also closely related (*i.e.*, an approximant) to the dodecagonal quasicrystal (DDQC) morphology observed experimentally in ABC stars by Matsushita *et. al.*[46], which consists of an aperiodic tiling of squares and triangles that cannot be described by a single vertex as (3^2.4.3.4) can. The observance of such quasicrystalline structures in soft materials as well as hard materials suggests that universal principles govern their behavior, and in ABC stars DDQC forms at compositions

close to that of (3^2.4.3.4).[19, 46] Finally, theoretical calculations[21] have also shown that (3^2.4.3.4) could exhibit photonic band gaps if composed of materials of the appropriate dielectric contrast.

In order to understand the stability mechanisms of these unique phases, the thermodynamic and structural properties described in Sec. 5.2 are calculated for (3^2.4.3.4), (3.4.6.4), and some competing phases at χN=30 and a point where (3^2.4.3.4) is stable, (f_A=0.45, f_B=0.30), with the results shown in Figs. 5(a) and 5(b). The stability of the tiling patterns is governed by relatively subtle differences in their βu_c and s_c/k_B, generally on the order of 10^{-2}. Clearly, (3^2.4.3.4) is energetically favorable at this point, having the smallest βu_c at the cost of also having the smallest s_c/k_B compared to the competing phases. This trend is observed for nearly every point where (3^2.4.3.4) is stable, with the exception of (f_A=0.43, f_B=0.30) and (f_A=0.43, f_B=0.31) where [8.6.4;8.6^2] and [8^2.4], respectively, have the smallest βu_c; (3^2.4.3.4) is stabilized at these two points by balancing βu_c and s_c/k_B as it also does not have the largest s_c/k_B (data not shown). This is in contrast to the results of Ref. 44 (which considered asymmetrically interacting stars), where (3^2.4.3.4) was found to exhibit larger s_c/k_B than competing morphologies at a point where it is stable – this could be due to the different interaction parameters. Additionally, although Ref. 31 decomposed βf_c of (3^2.4.3.4) into energetic and entropic contributions as a function of f_A at f_C=0.2 and χN=60, they did not note a mechanism behind its stability. The stability mechanism of (3^2.4.3.4) formed by symmetrically interacting stars is therefore elucidated for the first time by our results shown in Figs. 5.5(a) and 5.5(b).

(3.4.6.4) has similar properties to (3^2.4.3.4) in Fig. 5(a) as the point (f_A=0.45, f_B=0.30) considered there is adjacent to the single point where (3.4.6.4) is stable, *i.e.*, (f_A=0.44, f_B=0.29). However, it turns out that neither (3.4.6.4) nor (3^2.4.3.4) has the smallest βu_c at (f_A=0.44, f_B=0.29); [8.6.4;8.6^2] actually minimizes βu_c at this point but has prohibitively small s_c/k_B, and

since (3.4.6.4) has more favorable s_c/k_B it achieves its stability here by balancing energetic and entropic effects.

Although (3.4.6.4) and (3^2.4.3.4) have similar βu_c and s_c/k_B at (f_A=0.45, f_B=0.30) (as shown in Fig. 5(a)), Fig. 5(b) shows that (3.4.6.4) has more favorable AC contribution to βu_c, $\beta u_{c,AC}$, and dimensionless B-block conformational entropy per star, $s_{c,B}/k_B$, while (3^2.4.3.4) has more favorable $\beta u_{c,AB}$ and $s_{c,C}/k_B$. Furthermore, (3^2.4.3.4) exhibits this behavior against most of the competitive tiling patterns (except [8^2.4] and [12.6.4]); note that [8^2.4], [12.6.4], and (3^2.4.3.4) have nearly identical $\beta u_{c,AB}$ (thus essentially the same A-B interfacial area) and $s_{c,C}/k_B$, and it is the more favorable $\beta u_{c,AC}+\beta u_{c,BC}$ that stabilizes (3^2.4.3.4) against [8^2.4] and [12.6.4]. These results suggest that (3^2.4.3.4) incorporate the thermodynamically favorable features of these two direct Archimedean patterns while simultaneously compensating for their unfavorable energetic properties at the block fractions where (3^2.4.3.4) is stable. As the stable region of (3^2.4.3.4) lies between those of [8^2.4] and [12.6.4] in the phase diagram, this morphology can be considered as a hybridization of the latter two, not only in terms of the thermodynamic properties but also the morphological structure. The square regions of the superimposed Archimedean pattern of (3^2.4.3.4) are identical to a unit cell of [8^2.4] but with larger, distended majority regions while the triangular regions of (3^2.4.3.4) are identical to a unit cell of [12.6.4] but again with distended majority regions. We can therefore conclude that these properties ($\beta u_{c,AB}$ and $s_{c,C}/k_B$) are some of the defining aspects of [8^2.4], [12.6.4], and (3^2.4.3.4), with the last co-opting such properties from the former two and augmenting with its own favorable aspects. Other complex tiling patterns could also be considered as hybridizations of the more fundamental patterns, which may allow the design of yet to be discovered morphologies.

Finally, the lamellar-type morphologies (*i.e.*, HL and L) at (f_A=0.45, f_B=0.30) have both

significantly larger βu_c and s_c/k_B (on the order of 10^{-1}) than the tiling patterns at this point in the parameter space, where it is clear that the energetic cost of forming a lamellar-type morphology is too large for the entropic gain to stabilize it. Both HL and L also exhibit more favorable $\beta u_{c,\mathrm{AB}}$ and $s_{c,\mathrm{C}}/k_B$ than (3^2.4.3.4), although this is countered by their more unfavorable $\beta u_{c,\mathrm{AC}}$ and $\beta u_{c,\mathrm{BC}}$. This is particularly apparent for L, which can be attributed to its overlap of the C block with the domains of A and B that occurs due to the star architecture, where C microphase-separates as much as possible but must retain a significant amount of contact with B and, to a lesser extent, A. The small $\beta u_{c,\mathrm{AB}}$ observed for L results from the screening (or substitution) of interactions between A and B by this layer of C, while simultaneously resulting in its large contact area with A and B. This may be one of the factors that contributes to the destabilization of L at stronger segregations.[31]

Another interesting feature of Fig. 5.5(b) concerns the dimensionless translational entropy per star of the star junctions $s_{c,\mathrm{J}}/k_B$, shown for each morphology relative to (3^2.4.3.4). It can be seen that [8^2.4], [12.6.4], and (3^2.4.3.4) have nearly identical $s_{c,\mathrm{J}}/k_B$, resulting in their entropic properties being governed solely by the conformational entropy of each block. In contrast, (3.4.6.4), [8.6.4;8.6^2], and [10.6.4;10.6^2] exhibit slightly more favorable $s_{c,\mathrm{J}}/k_B$ with [10.6.4;10.6^2] having the largest $s_{c,\mathrm{J}}/k_B$ among the phases considered here, although their differences in $s_{c,\mathrm{J}}/k_B$ are generally small. This quantity depends solely on the junction density $\rho_{\mathrm{J}}(\mathbf{r})$ of each morphology, given in Fig. 5.5(d) for (3^2.4.3.4) along with a unit cell of the morphology in Fig. 5.5(c) visualized in such a way that the interfaces between the microphase-separated domains are clearly discerned. Noting that $\rho_{\mathrm{J}}(\mathbf{r})$ is proportional to the probability that a star junction lies in a differential area element, we see from Fig. 5.5(d) that the junctions are smeared along the interfaces rather than tightly aligned along 1D lines, a result attributed to the relatively

weak segregation at χN=30. Despite this smearing, the junction density still exhibits clear maxima centered on the points where the majority domains of each species meet. It is interesting to note that certain domain interfaces appear to be more favorable for the junctions, thus resulting in greater junction densities; this can be seen in Fig. 5.5(d) via the red regions, where junctions are distributed more prominently along the AB interfaces than the AC or BC interfaces. As χN increases, we expect the area over which the junctions are distributed to shrink significantly and eventually approach a 1D alignment in the limit of strong segregation.

5.4 Conclusions

In this work, we have performed numerical polymer self-consistent field (SCF) calculations of the "standard" model (*i.e.*, incompressible melts of continuous Gaussian chains with the Dirac δ-function interactions) for symmetrically interacting ABC miktoarm triblock terpolymer melts (referred to as stars) using the recently released C++/Cuda version[37] of an open-source software, PSCF[38, 39]. The numerical accuracy of our calculations is rigorously tested, and the central region of the phase diagram (in terms of the volume fraction of the P-block in the star, f_P with P=A,B,C) constructed at the segregation strength χN=30 with a total of 16 candidate phases considered, including one 1D phase, ten 2D phases, and five 3D phases (*i.e.*, those shown in Fig. 1 in addition to the 2D knitting pattern[27] and the 3D hierarchical-checkerboard lamellae (HCL, referred to as LAS in Ref. 34)). Eight of these 2D phases are tiling patterns known to form in this system from previous studies[29, 31, 34], and of these eight tiling patterns we have found seven to be definitively stable at χN=30: [6^3], [8^2.4], [12.6.4], (3^2.4.3.4), (3.4.6.4), [8.6.4;8.6^2], and [10.6.4;10.6^2]. Notably, (3.4.6.4) is reported as stable for the first time while the phase of hierarchical-hexagonal lamellae (HHL) is found stable for the first time for symmetrically interacting ABC stars. Our numerical accuracy and careful selection of candidate phases allow

the resolution of several outstanding discrepancies from previous SCF studies of the same model system, demonstrating, for example, the stability of [12.6.4], (3^2.4.3.4), and [10.6.4;10.6^2] and metastability of hierarchical-tetragonal lamellae (HTL) and [8.6.4;8^2.4;12.6.4;12.8.4], which had conflicting results from previous studies[29, 31, 34, 35]. Finally, we have studied in detail the (mean-field) thermodynamic and morphological properties of two stable complex tiling patterns, (3^2.4.3.4) and (3.4.6.4), and revealed the mechanisms behind their stability. While (3^2.4.3.4) is energetically stabilized in most cases, at a few points the stability of (3^2.4.3.4) and (3.4.6.4) is due to their optimal balance between the energetic and entropic effects.

Having established the stable and unstable tiling patterns for symmetrically interacting ABC stars at χN=30 within the "standard" model using SCF calculations, some logical directions for future work are: (1) to systematically increase χN for symmetrically interacting ABC stars, (2) to systematically study the phase behavior of symmetrically interacting ABC stars outside the central region of the $\{f_P\}$ parameter space, and (3) to systematically explore the phase behavior of asymmetrically interacting ABC stars. Only two SCF studies[31, 35] have been devoted to symmetrically interacting ABC stars at χN=60, although it is possible that the center of the phase diagram (*i.e.*, the region occupied by the tiling patterns) is relatively insensitive to χN as suggested earlier. Most of the existing studies have focused on these tiling patterns as they are unique morphologies that are rarely observed in other polymer systems, and it has been noted[27] that the star architecture's topological constraint is less severe as the outer regions of the $\{f_P\}$ parameter space are approached, resulting in the appearance of familiar morphologies from diblock and linear triblock copolymers. Nevertheless, some theoretical[34, 35] and experimental[47] studies on ABC stars have demonstrated the existence of unique 3D morphologies outside of the central region of the $\{f_P\}$ parameter space, and it is worthwhile to systematically study the phase

behavior of these regions as they are still poorly understood. Finally, only one SCF study[44] has systematically explored the phase behavior of asymmetrically interacting ABC stars (at $\chi_{AB}N=\chi_{BC}N=30$ and $\chi_{AC}N=50$). It is our hope that this work will serve as a useful reference for these future investigations into the self-assembly of this fascinating class of materials.

REFERENCES

[1] F. S. Bates and G. H. Fredrickson, Phys. Today 52 (2), 32-38 (1999).

[2] C. Park, J. Yoon and E. L. Thomas, Polymer 44 (22), 6725-6760 (2003).

[3] F. S. Bates, M. A. Hillmyer, T. P. Lodge, C. M. Bates, K. T. Delaney and G. H. Fredrickson, Science 336 (6080), 434-440 (2012).

[4] N. Hadjichristidis, H. Iatrou, M. Pitsikalis, S. Pispas and A. Avgeropoulos, Prog. Polym. Sci. 30 (7), 725-782 (2005).

[5] Y. Matsushita, K. Hayashida and A. Takano, Macromol. Rapid Commun. 31 (18), 1579-1587 (2010).

[6] M. Liu, W. Li, F. Qiu and A.-C. Shi, Macromolecules 45 (23), 9522-9530 (2012).

[7] L. Li and W. Li, Sci. Sin. Chim. 53 (4), 651-663 (2023).

[8] S. Okamoto, H. Hasegawa, T. Hashimoto, T. Fujimoto, H. Zhang, T. Kazama, A. Takano and Y. Isono, Polymer 38 (21), 5275-5281 (1997).

[9] S. Sioula, N. Hadjichristidis and E. L. Thomas, Macromolecules 31 (23), 8429-8432 (1998).

[10] K. Hayashida, A. Takano, S. Arai, Y. Shinohara, Y. Amemiya and Y. Matsushita, Macromolecules 39 (26), 9402-9408 (2006).

[11] Y. Matsushita, K. Hayashida, T. Dotera and A. Takano, J. Phys. Condens. Matter 23 (28), 284111 (2011).

[12] T. Dotera and A. Hatano, J. Chem. Phys. 105 (18), 8413-8427 (1996).

[13] Y. Bohbot-Raviv and Z. G. Wang, Phys. Rev. Lett. 85 (16), 3428-3431 (2000).

[14] X. He, L. Huang, H. Liang and C. Pan, J. Chem. Phys. 116 (23), 10508-10513 (2002).

[15] X. He, L. Huang, H. Liang and C. Pan, J. Chem. Phys. 118 (21), 9861-9863 (2003).

[16] J. G. E. M. Fraaije, J. Chem. Phys. 99 (11), 9202-9212 (1993).

[17] J. G. E. M. Fraaije, B. A. C. van Vlimmeren, N. M. Maurits, M. Postma, O. A. Evers, C. Hoffmann, P. Altevogt and G. Goldbeck-Wood, J. Chem. Phys. 106 (10), 4260-4269 (1997).

[18] T. Gemma, A. Hatano and T. Dotera, Macromolecules 35 (8), 3225-3237 (2002).

[19] T. Dotera and T. Gemma, Phil. Mag. 86 (6-8), 1085-1091 (2006).

[20] T. Dotera, Phil. Mag. 88 (13-15), 2245-2251 (2008).

[21] K. Ueda, T. Dotera and T. Gemma, Phys. Rev. B 75 (19), 195122 (2007).

[22] Z. Liu, Z. Wang, Y. Yin, R. Jiang and B. Li, Soft Matter 17 (21), 5336-5348 (2021).

[23] C. I. Huang, H. K. Fang and C. H. Lin, Phys. Rev. E 77, 031804 (2008).

[24] Y. Feng, J. Wu, B. Li and Q. Wang, Soft Matter 18 (14), 2750-2756 (2022).

[25] Y. Feng, B. Li and Q. Wang, Soft Matter 18 (26), 4923-4929 (2022).

[26] F. Drolet and G. H. Fredrickson, Phys. Rev. Lett. 83 (21), 4317-4320 (1999).

[27] P. Tang, F. Qiu, H. Zhang and Y. Yang, J. Phys. Chem. B 108 (24), 8434-8438 (2004).

[28] Z. Guo, G. Zhang, F. Qiu, H. Zhang, Y. Yang and A. C. Shi, Phys. Rev. Lett. 101 (2), 028301 (2008).

[29] G. Zhang, F. Qiu, H. Zhang, Y. Yang and A.-C. Shi, Macromolecules 43 (6), 2981-2989 (2010).

[30] G. Tzeremes, K. K. Rasmussen, T. Lookman and A. Saxena, Phys. Rev. E 65 (4), 041806 (2002).

[31] W. Li, Y. Xu, G. Zhang, F. Qiu, Y. Yang and A. C. Shi, J. Chem. Phys. 133 (6), 064904 (2010).

[32] E. W. Cochran, C. J. Garcia-Cervera and G. H. Fredrickson, Macromolecules 39 (7), 2449-2451 (2006).

[33] E. W. Cochran, C. J. Garcia-Cervera and G. H. Fredrickson, Macromolecules 39 (12), 4264-4264 (2006).

[34] W. Xu, K. Jiang, P. Zhang and A. C. Shi, J. Phys. Chem. B 117 (17), 5296-5305 (2013).

[35] M. Qian and Y. Xu, Langmuir 38 (26), 7889-7897 (2022).

[36] C. A. Tyler and D. C. Morse, Macromolecules 36 (21), 8184-8188 (2003).

[37] https://github.com/dmorse/pscfpp.

[38] G. K. Cheong, A. Chawla, D. C. Morse and K. D. Dorfman, Eur. Phys. J. E 43 (2), 15 (2020).

[39] A. Ranjan, J. Qin and D. C. Morse, Macromolecules 41 (3), 942-954 (2008).

[40] M. W. Matsen, Eur. Phys. J. E 30 (4), 361-369 (2009).

[41] A. Arora, D. C. Morse, F. S. Bates and K. D. Dorfman, J. Chem. Phys. 146 (24), 244902 (2017).

[42] M. W. Matsen and F. S. Bates, J. Chem. Phys. 106 (6), 2436-2448 (1997).

[43] K. Jiang, J. Zhang and Q. Liang, J. Phys. Chem. B 119 (45), 14551-14562 (2015).

[44] S. Lee, M. J. Bluemle and F. S. Bates, Science 330 (6002), 349-353 (2010).

[45] K. Hayashida, T. Dotera, A. Takano and Y. Matsushita, Phys. Rev. Lett. 98 (19), 195502 (2007).

[46] J. Park, S. Jang and J. Kon Kim, J. Polym. Sci. Part B: Polym. Phys. 53 (1), 1-21 (2014).

[47] W. H. Press, in Numerical recipes in C: The art of scientific computing (1992).

6 CONCLUDING REMARKS

A high-performance software package, PSCF+, has been developed, which allows various combinations of chain-connectivity models (including CGC, discrete Gaussian chains, and freely jointed chains), non-bonded isotropic pair (including the Dirac δ-function, soft-sphere (SS), dissipative particle dynamics (DPD), and Gaussian) potentials and system compressibility (incompressible *vs.* compressible). Acceleration algorithms including Richardson-extrapolated pseudo-spectral methods, crystallographic fast Fourier transform, "slice" algorithm, and so on are implemented, which can speed up the SCF calculations and reduce the GPU memory usage significantly. PSCF+ is freely available on Github now.

We have found in SCF calculations performed by several groups that the relative stability among seven FK phases (A15, σ, H, Z, pσ, C14 and C15) formed by DBC systems is dominated by their internal-energy densities (*i.e.*, the repulsion between A and B blocks); this is the case for both neat DBC melts and binary DBC blends (including A_1-B_1/A_2-B_2 and A_1-B_1/A_2), regardless of the detailed models used. We have also found that the variations of βf_c- (and βu_c-) curves of different FK phases in these calculations are clearly correlated with their $\overline{z}$. Finally, C14, C15 and Z have larger internal energy per chain due to the A-B repulsion than s and A15, thus not stable in A-B melts, and the change of stable phase between σ and C14/C15 in binary DBC blends is mainly due to that in the interchain repulsion. However, deeper understanding in the formation mechanism requires SCF calculations of more FK phases.

In addition, we have performed SCF calculations of the "standard" model for symmetrically interacting ABC miktoarm triblock terpolymer melts (referred to as stars) using

PSCF+, and the central region of the phase diagram is constructed in detail with the (3.4.6.4) pattern and the 3D phase of hierarchical-hexagonal lamellae found to be stable for the first time.